EVOLUTION OF CASCADIA LANDSCAPES: DRAINAGE REORGANIZATION

INFERRED FROM TOPOGRAPHIC TRANSFORMATIONS AND

DENDROCHRONOLOGICAL DATING OF

LANDSLIDE-DAMMED LAKES

by

WILLIAM TRUIN STRUBLE

A DISSERTATION

Presented to the Department of Earth Sciences
and the Graduate School of the University of Oregon
in partial fulfillment of the requirements
for the degree of
Doctor of Philosophy

December 2020

DISSERTATION APPROVAL PAGE

Student: William Truin Struble

Title: Evolution of Cascadia Landscapes: Drainage Reorganization Inferred from Topographic Transformations and Dendrochronological Dating of Landslide-Dammed Lakes

This dissertation has been accepted and approved in partial fulfillment of the requirements for the Doctor of Philosophy degree in the Department of Earth Sciences by:

| | |
|---|---|
| Joshua J. Roering | Chairperson |
| Rebecca J. Dorsey | Core Member |
| Leif Karlstrom | Core Member |
| Daniel G. Gavin | Institutional Representative |

and

| | |
|---|---|
| Kate Mondloch | Interim Vice Provost and Dean of the Graduate School |

Original approval signatures are on file with the University of Oregon Graduate School.

Degree awarded December 2020

DISSERTATION ABSTRACT

William Truin Struble

Doctor of Philosophy

Department of Earth Sciences

December 2020

Title: Evolution of Cascadia Landscapes: Drainage Reorganization Inferred from Topographic Transformations and Dendrochronological Dating of Landslide-Dammed Lakes

Landscapes evolve through the contributions of uplift and erosion over myriad spatiotemporal scales. Over long timescales ($>10^3$ yr), tectonics and climate set landscape and drainage basin form. Over societally relevant timescales essential for quantifying hazards, earthquake-triggered landslides directly link active tectonics and surface processes. In this dissertation, I clarify the timing of bedrock landsliding as well as the scale of landforms responsible for setting the geometry and position of drainage divides throughout the Cascadia forearc.

Despite the presence of >20,000 mapped bedrock landslides in the Oregon Coast Range (OCR), no single slope failure has been definitively linked with the last major Cascadia Subduction Zone (CSZ) earthquake, which occurred in January 1700 AD. I utilize dendrochronology of 'ghosts forests' at landslide-dammed lakes, which provides seasonal accuracy, to establishing the timing of dam emplacement. In Chapter II, I determine that the landslides that formed Klickitat and Wasson Lakes, Oregon, occurred in the winters of 1751/52 and 1819/20, respectively. I additionally demonstrate that, while $^{14}$C dating of landslides has corroborative power, landslide ages are ambiguous and sometimes thousands of years too old when using $^{14}$C alone. I build on this

dendrochronological technique in Chapter III to establish the timing of 20 landslides in the OCR. None of these landslides date to 1700 AD. Notably, however, at least 4 landslide dams temporally cluster to the winter of 1889/90 AD, coincident with regionally significant flooding likely triggered by a series of atmospheric rivers. I further establish that landslide dams are preferentially preserved at small to intermediate catchment areas and valley widths, where large wood accumulated upstream of landslide deposits armors the dams. Finally, in Chapter IV, I consider how long-wavelength landforms set drainage basin extent and stability. I utilize continuous wavelet transforms to observe that at wavelengths $>\sim30$ km, the Willamette Valley extends along the entire CSZ, a landform I term the Cascadia Forearc Lowland (CFL). Further, by smoothing topography to progressively longer wavelengths, I establish that synthetic drainage networks consolidate into margin-parallel rivers at wavelengths $>30$ km, coincident with the CFL and in agreement with field observations of stream capture.

This dissertation includes previously published and unpublished co-authored material.

CURRICULUM VITAE

NAME OF AUTHOR:  William T. Struble

GRADUATE AND UNDERGRADUATE SCHOOLS ATTENDED:

> University of Oregon, Eugene
> University of Nevada, Reno

DEGREES AWARDED:

> Doctor of Philosophy, Earth Sciences, 2020, University of Oregon
> Bachelor of Science, Geology, 2016, University of Nevada, Reno

AREAS OF SPECIAL INTEREST:

> Geomorphology, Landscape Evolution, Landslides, Tectonics

PROFESSIONAL EXPERIENCE:

> Graduate Employee, Department of Earth Sciences, University of Oregon, 2016-2020
> Undergraduate Research Assistant, Departments of Geological Sciences and Engineering, Physics, University of Nevada, Reno, 2012-2016.

GRANTS, AWARDS, AND HONORS:

> Research Excellence Award, Department of Earth Sciences, University of Oregon, 2020.
>
> Lewis and Clark Fund Grant for Topographic Map Interpretation, American Philosophical Society, 2020-2021.
>
> Lokey Doctoral Fellowship, University of Oregon, 2019-2020.
>
> EDMAP Grant, United States Geological Survey, 2019.
>
> National Center for Airborne Laser Mapping Seed Grant, 2018.
>
> National Science Foundation Graduate Research Fellowship Honorable Mention, 2017.

Outstanding Bachelor of Science Student in Geology, University of Nevada, Reno, 2016.

PUBLICATIONS:

**Struble, W.T.**, Roering, J.J., Black, B.A., Burns, W.J., Calhoun, N.C., & Wetherell, L.R. (in review), Atmospheric Rivers Trigger and Large Woody Debris Preserves Abundant Bedrock Landslide Dams in Western Oregon, Journal of Geophysical Research: Earth Surface.

**Struble, W.T.**, Roering, J.J., Dorsey, R.J., & Bendick, R. (in revision), Characteristic scales of drainage reorganization in Cascadia, Geophysical Research Letters.

**Struble, W.T.**, McCoy, S.W., Hobley, D.E., Tucker, G.E., & Gregory, L.C. (in revision), Mountain-Front Facet Gradient Encodes Long-Term Slip Rates Along the Wasatch Normal Fault, USA, Geophysical Research Letters.

Wetherell, L.R., Ely, L.L., Roering, J.J., Walsh, M.K., Burchfield, M., Nace, K., Wetherell, M., **Struble, W.T.**, Black, B.A. (in revision), Quantifying sedimentation patterns of small landslide-dammed lakes in the central Oregon Coast Range, Earth Surface Processes and Landforms.

LaHusen, S.R., Duvall, A.R., Booth, A.M., Grant, A., Mishkin, B.A., Montgomery, D.R., **Struble, W.T.**, Roering, J.J., & Wartman, J. (2020), Rainfall triggers more deep-seated landslides than Cascadia earthquakes in the Oregon Coast Range, USA, Science Advances 6, doi:10.1126/sciadv.aba6790.

Tucker, G.E., Hobley, D.E., McCoy, S.W., & **Struble, W.T.** (2020), Modeling the Shape and Evolution of Normal-Fault Facets, Journal of Geophysical Research: Earth Surface 125, doi:10.1029/2019JF005305.

**Struble, W.T.**, Roering, J.J., Black, B., Burns, W.J., Calhoun, N., & Wetherell, L. (2020), Dendrochronological dating of landslides in western Oregon: searching for signals of the Cascadia A.D. 1700 earthquake, Geological Society of America Bulletin, 130, doi:10.1130/B35269.1

Perkins, J.P., Roering, J.J., Burns, W.J., **Struble, W.T.**, Black, B., Schmidt, K., Duvall, A., & Calhoun, N. (2018), Hunting for landslides from Cascadia's great earthquakes, Eos, 99, doi:10.1029/2018EO103689.

ACKNOWLEDGMENTS

TABLE OF CONTENTS

LIST OF FIGURES

# LIST OF TABLES

**CHAPTER I**

**INTRODUCTION**

Landscapes are formed by the dynamic interplay of uplift and erosion. Over large spatiotemporal scales, uplift is driven by tectonic processes, with mantle and isostatic contributions, while climatic variability dictates erosion. Yet, while tectonics and climate clearly conduct the dynamic adjustment of landscapes, the scale of landforms and processes responsible for setting the extent of drainage basins and triggering drainage reorganization, respectively, has remained unclear. Superimposed on long-wavelength landforms and processes are discrete perturbations triggered by climatic or seismic events. Deep-seated bedrock landslides, for instance, serve as a primary erosional process in steep and mountainous landscapes. In many orogenic landscapes where earthquakes are common, bedrock landsliding is a common response to ground motion and serves as a discrete, observable link between tectonics and hillslope erosion. In Cascadia, however, despite the presence of >20,000 mapped deep-seated landslides in the Oregon Coast Range, no bedrock landslide has been definitively linked with the last major subduction zone earthquake. These knowledge gaps, spread over a large suite of scales, raise several questions about forearc landscape evolution: How common are bedrock landslides during Cascadia Subduction Zone earthquakes? What particular seismic or hydrologic processes drive deep-seated slope instability, and do landslide dams preserve a record of slope failure in characteristic landscape locations? What landform scales dictate the location and stability of drainage divides, and do characteristic landforms predict drainage disequilibrium? In this dissertation, I clarify the scale and timing of landscape perturbations in the Cascadia forearc. Specifically, I use multiple landslide

1

geochronological techniques (e.g. dendrochronology, $^{14}$C, topographic roughness) to clearly establish the timing of bedrock landsliding in the Oregon Coast Range and clarify whether seismic or hydrologic processes are the primary drivers of deep-seated slope instability. I additionally utilize topographic transformation techniques (e.g. continuous wavelet transforms, Gaussian filtering) to constrain the primary landforms responsible for setting the extent, and therefore the scale-dependence, of drainage basins in the forearc as well as predict future drainage reorganization.

In Chapter II, co-authored with Joshua Roering (University of Oregon), Bryan Black (University of Arizona), William Burns (Oregon Department of Geology and Mineral Industries), Nancy Calhoun (Oregon Department of Geology and Mineral Industries, and Logan Wetherell (Central Washington University), and published in *Geological Society of America Bulletin* in January 2020, I utilize dendrochronology of 'ghost forests' at landslide-dammed lakes in the Oregon Coast Range to establish with seasonal accuracy the timing of landslide failure at Wasson and Klickitat Lakes. Furthermore, I compare the seasonally accurate landslide ages to those calculated using traditional landsliding dating techniques, specifically $^{14}$C dating. I establish that not only does $^{14}$C dating produce ambiguous landslide ages at both sites, but, in some cases, results in ages that are ~9,000 years too old. Notably, the timing of landslide-dammed lake formation at Klickitat and Wasson Lake does not correspond to the last major Cascadia Subduction Zone earthquake, which occurred on January 26, 1700 AD.

In Chapter III, co-authored with Joshua Roering (University of Oregon), Bryan Black (University of Arizona), William Burns (Oregon Department of Geology and Mineral Industries), Nancy Calhoun (Oregon Department of Geology and Mineral

Industries, and Logan Wetherell (Central Washington University, University of Oregon), and in review at *Journal of Geophysical Research: Earth Surface*, I build on the landslide dating framework I establish in Chapter II to date 20 landslide-dammed lakes in the Oregon Coast Range. While most deep-seated bedrock landslides in the Oregon Coast Range have previously been assumed to be triggered by Cascadia Subduction Zone earthquakes, none of these 20 dated slides correspond to the 1700 AD earthquake. Rather, I observe temporal clustering of at least 4 dated landslide dams in the winter of 1889/90 AD, corresponding to a series of atmospheric rivers that triggered one of the largest regional flooding events in western Oregon and northern California. Furthermore, I note a conspicuous paucity of preserved landslide dams at drainage areas >8 km$^2$ and valley widths >80 m. This characteristic location in the landscape corresponds with the confluence of third order rivers, where valleys are sufficiently wide to transmit mature Douglas-fir and other conifer trees. I further suggest that the accumulation of large wood upstream from landslide dam deposits armors landslide dams from through-flowing debris flows and the erosive effects of coarse sediment transport.

Chapter IV was co-authored with Joshua Roering (University of Oregon), Rebecca Dorsey (University of Oregon), and Rebecca Bendick (University of Montana), and is in revision at the journal *Geophysical Research Letters*. While terrestrial landscapes exhibit drainage networks that deviate from those predicted by long wavelength topography (Black et al., 2017), the scale of landforms and associated processes responsible for setting the extent and morphology of river networks remains unclear. In Chapter IV, I consider dominant topographic features at different scales and establish the scale-dependency of drainage networks in the forearc of the Cascadia

Subduction Zone. I utilize continuous wavelet transforms to map landforms over a range of wavelengths. Notably, I observe that at wavelengths >30 km, the Willamette Valley extends along the entire subduction zone margin, a landform that I term the Cascadia Forearc Lowland. Furthermore, to establish how drainage patterns evolve as the influence of short wavelength landforms, and therefore small-scale processes, are removed, I Gaussian filter topography to progressively longer wavelengths and map synthetic drainage networks. I observe that at wavelengths >30 km, forearc drainages reorganize into margin-parallel drainage systems, akin to the modern Willamette River, that are coincident with the Cascadia Forearc Lowland. Coupled with field observations of stream capture in the forearc, I suggest that long-wavelength topography and synthetic drainage networks are an accurate predictor of future stream capture locations and drainage patterns.

This dissertation addresses processes that act over disparate wavelengths and timescales. As such, it presents unprecedented clarity in landslide geochronology in the Pacific Northwest, crucial for quantifying hazards during major earthquakes and storm events. It additionally propels interpretations of landscape evolution and forearc drainage history into a promising quantitative realm, which will influence landscape and tectonics analyses globally.

# CHAPTER II

# DENDROCHRONOLOGICAL DATING OF LANDSLIDES IN WESTERN OREGON: SEARCHING FOR SIGNALS OF THE CASCADIA A.D. 1700 EARTHQUAKE

## 1. Introduction

Despite improved resolution of the recurrence interval of large-magnitude subduction zone earthquakes in Cascadia (Goldfinger et al., 2012), prediction of ground motion and landscape response remains highly uncertain (Allstadt et al., 2013). The Cascadia subduction zone has produced numerous large (>M 9.0) earthquakes, with an average recurrence interval of 300–500 yr (Goldfinger et al., 2012). The timing of the most recent earthquake, which occurred on the evening of 26 January 1700, has been constrained in part by a combination of (1) offshore turbidite records (Goldfinger et al., 2012); (2) the dendrochronology of "ghost forests," which were drowned by coseismic subsidence and the resultant tsunami (Atwater and Yamaguchi, 1991; Yamaguchi et al., 1997); and (3) the arrival of the tsunami in Japan (Atwater et al., 2005). During future great subduction zone earthquakes (>M 8.0), the magnitude of shaking is locally uncertain (Allstadt et al., 2013), although shaking is expected to be high along the coast, with peak ground acceleration (PGA) values of 0.4 *g* (percent of gravity) and higher

5

(Frankel et al., 2018; Wirth et al., 2018). Shaking will attenuate inland toward the Willamette Valley and the Cascades, though PGA will remain high throughout the Oregon Coast Range, in excess of 0.2 $g$ (Figure 1; Madin and Burns, 2013; Olsen et al., 2015). High-intensity and long-duration shaking may affect landslide reactivation differently than expected for shallow, crustal earthquakes (Meunier et al., 2008, 2007). Shallow crustal faults in western Oregon (e.g., Blakely et al., 2000) may produce earthquakes capable of initiating landslides as well, though linking landslides with such earthquakes is beyond the scope of this analysis.

Historically, earthquakes can produce $10^4$ to $10^5$ landslides, including disrupted (rock falls, debris avalanches) and coherent (slumps) slides as well as lateral spreads (earth and debris lateral spreads and flows; Keefer, 2002, 1984; Wartman et al., 2013). In many landscapes, a significant proportion of total erosion occurs due to coseismic landslides (Dadson et al., 2004; Densmore and Hovius, 2000; Hovius et al., 2011; Li et al., 2014; Marc et al., 2016a), the distribution of which is commonly spatially variable and complicated. In many cases, the spatial density of earthquake-induced landsliding varies systematically with ground motion (Meunier et al., 2007); however, in cases where PGA or peak ground velocity (PGV) do not clearly scale with distance to the epicenter, landslide density may instead correlate with distance to fault rupture or the frequency content of seismic waves (Massey et al., 2018; Serey et al., 2019). More than 15,000 landslides were triggered in the 2008 Wenchuan earthquake (Li et al., 2014), and in the 2015 Gorkha, Nepal, earthquake, landslides increased in density over 100 km away from the epicenter, likely due in part to variation in substrate weathering and strength and the direction of rupture propagation (Roback et al., 2017). In addition, low rock strength

6
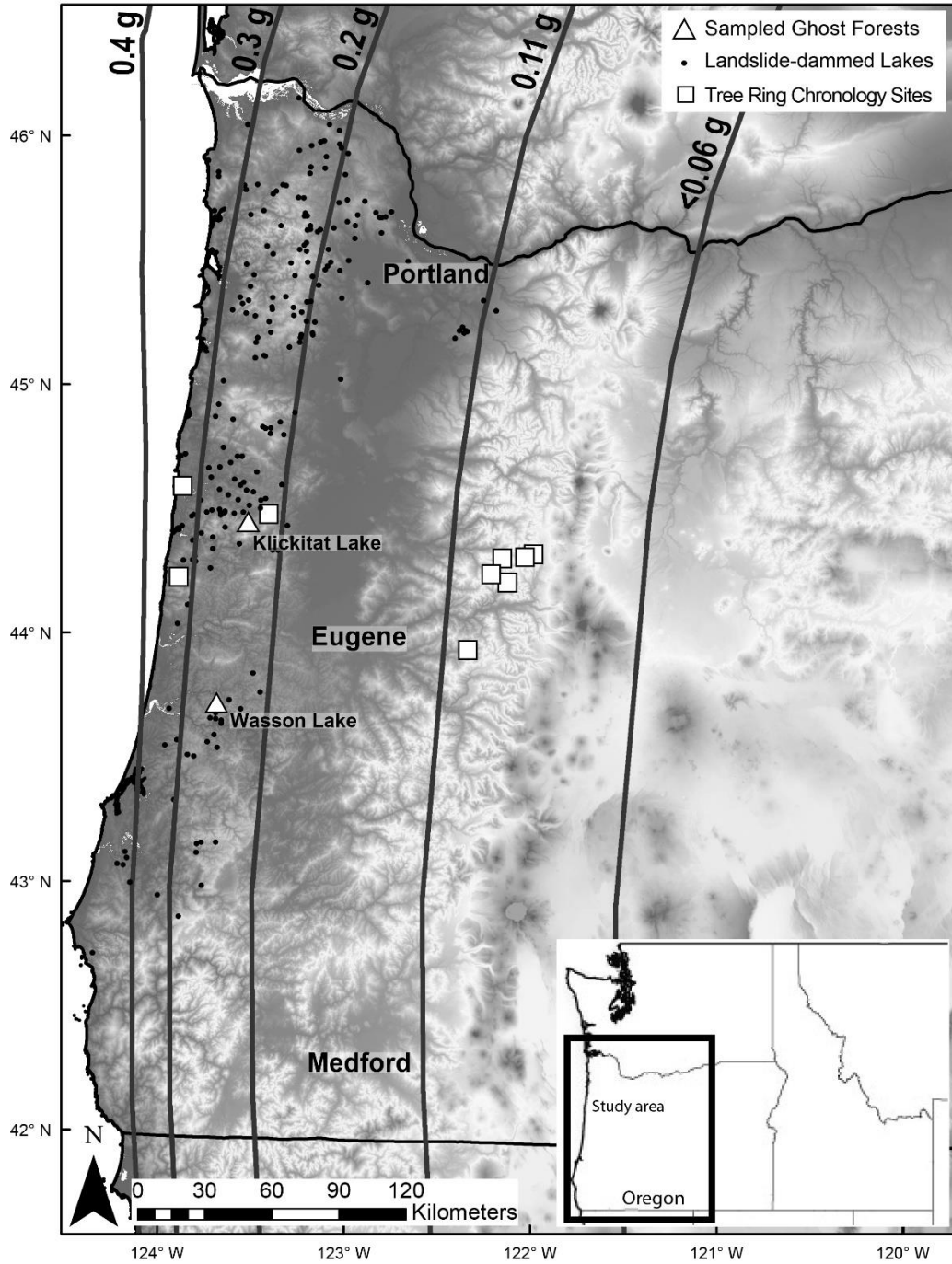
**Figure 1**. **Western Oregon and landslide-dammed lakes.** Triangles represent the two landslide-dammed lakes we dated in this study, Wasson Lake and Klickitat Lake. Squares are the sites of Douglas fir chronologies constructed in Black et al. (2015) that were used to cross-date the "ghost forest" trees. Labeled black contours represent the expected peak ground acceleration during a $M_w$ 9 Cascadia subduction zone earthquake (Madin and Burns, 2013).

often determines the pattern of coseismic slope instability (Newmark, 1965), as made

apparent in the 2011 Tohoku earthquake, where >80% of the >3400 landslides occurred

in Quaternary sediments and weak Neogene rock units (Wartman et al., 2013).

Probabilistic models are useful for predicting where coseismic landsliding is most

pervasive during earthquakes as well as the cumulative volume of all coseismic

landslides (Jibson et al., 2000; Keefer, 1984). Keefer (1984) noted a power-law scaling

relationship between seismic moment and total landslide volume. The volume of

landslides associated with subduction zone earthquakes, however, is often significantly

less than that predicted by the power-law scaling relationship (Marc et al., 2016b),

although the number of subduction zone earthquake inventories is very limited (Tanyaş et

al., 2017, 2018). By contrast, at least one subduction zone earthquake deviates markedly

from this trend. The 1960 Chilean earthquake caused $\sim$250 km$^2$ of the proximal terrain to

experience landsliding (Veblen and Ashton, 1978), which, when applied to the area-

volume relationship of Larsen et al. (2010), produces a resultant landslide volume much

larger than subduction zone earthquakes of a similar magnitude (Perkins et al., 2018).

Hence, the apparent paucity of landslides during some subduction zone earthquakes may

partially be accounted for by the limited number of landslide inventories for subduction

zone earthquakes as opposed to shallow crustal earthquakes (Marc et al., 2016b). If the

recent data sets are representative, the low rates of landslides during subduction zone

events may additionally be due to seismic attenuation, great depth of the hypocenter, and

the directivity of seismic waves away from shore (Gallen et al., 2016; Gorum et al., 2014;

Kargel et al., 2016; Meunier et al., 2008, 2007). Regardless, the observed variability in

slope failure during subduction zone earthquakes warrants investigation of past slope failures in Cascadia.

The coastal and forearc regions of Cascadia exhibit a long history of widespread slope instability (Roering et al., 2005; Schulz et al., 2012). In the Oregon Coast Range, the geologic and topographic signature of landsliding is pervasive; steep topography and weak lithologic units combine to promote slope instability over a range of time scales (Burns et al., 2012; Roering et al., 2005; Schmidt and Montgomery, 1995). Here, thousands of shallow, colluvial landslides and debris flows associated with intense rainfall have been historically observed (Montgomery et al., 2000; Robison et al., 1999; Stock and Dietrich, 2003). However, all of the >40,000 known deep-seated landslides (Burns and Watzig, 2014) appear to have formed prior to European settlement, which suggests that the conditions promoting pervasive deep-seated instability have not been realized in recent decades or longer. Elsewhere, deep-seated landslides are common during large-magnitude earthquakes, particularly in areas of high relief (e.g., Gallen et al., 2016; Kargel et al., 2016; Keefer, 1984; Marc et al., 2016a; Roback et al., 2017; Vala-gussa et al., 2019). However, no subaerial landslide in Cascadia has been definitively linked to a subduction zone earthquake, including the A.D. 26 January 1700 earthquake (Atwater et al., 2005; Goldfinger et al., 2012; Karlin et al., 2004; Leithold et al., 2018; Schulz et al., 2012; Schuster et al., 1992). Here, we used dendrochronological methods to date two landslides in the Oregon Coast Range with subannual precision, placing particular interest in links to the A.D. 1700 subduction zone earthquake. However, as this approach is more broadly applied, it holds the potential to identify synchrony among

landslide events and infer mechanisms of slope failure, whether from earthquake-induced ground motion or extreme hydrologic events.

## 1.1. Dating Prehistoric Landslides

Landslides have been dated using surface exposure dating and the dendrochronology of live trees on deposits (Ballantyne and Stone, 2004; Fantucci and McCord, 1995; Ivy-Ochs et al., 2009; Lang et al., 1999; Stefanini, 2004; and many others), although radiocarbon ($^{14}$C) dating is the most common method (Benda, 1990; Booth et al., 2017; Clague, 2015; Lang et al., 1999; Logan et al., 1998; Pringle et al., 1998; Reneau et al., 1986; Reneau and Dietrich, 1991; Reynolds et al., 2015; Suter et al., 2013; and many others). The use of $^{14}$C dating on detrital materials in sediments is particularly applicable in the Oregon Coast Range due to the abundance of datable organic material (e.g., Benda, 1990; Reneau et al., 1986; Reneau and Dietrich, 1991) and has been used elsewhere to build comprehensive landslide chronologies and calibrate other relative dating techniques. For example, surface roughness–age calculations of landslides have been calibrated by $^{14}$C dating (e.g., Booth et al., 2017; LaHusen et al., 2016; McKean and Roering, 2004), as have tephrochronologies that inform volcanic eruptive histories (Braitseva et al., 1993) and reconstructions of paleolandscapes (Cerovski-Darriau et al., 2014; Danišík et al., 2012).

While these techniques have provided useful data sets of landslide recurrence in various landscapes, their precision is not adequate to date recent landslides or tie them to specific triggering events. Surface exposure dating is limited when field relationships between sampled surfaces are not clear (Ballantyne and Stone, 2004; Ivy-Ochs et al., 2009), and landslides must be sufficiently large to expose fresh and shielded bedrock

(Lang et al., 1999). Radiocarbon dating has inherent uncertainty due to varying

production rates of $^{14}$C in the atmosphere, made evident in the "wiggles" of the

radiocarbon calibration curve. Some portions of this curve oscillate more than others,
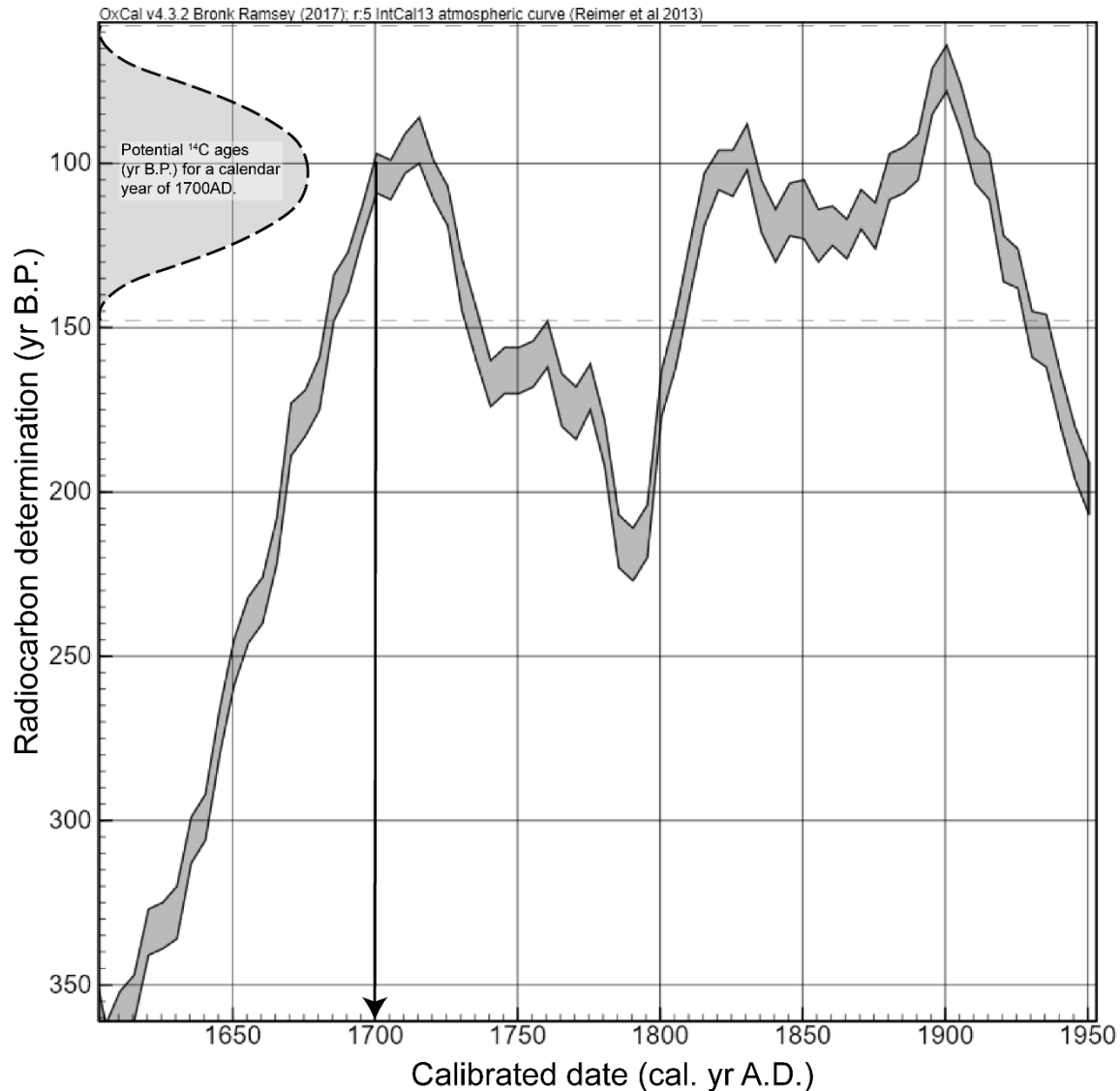


**Figure 2**. **Radiocarbon calibration curve between A.D. 1600 and present (1950).** The oscillation of the curve (solid line, filled) results in several potential calendric (calibrated) ages where the uncalibrated $^{14}$C age intercepts the curve. Note that a $^{14}$C age on wood that died in ca. A.D. 1700 could intersect the calibration curve at four locations. Dashed-line probability distribution function (PDF) provides range of potential $^{14}$C ages that may suggest A.D. 1700 as a possible calendar year age. Figure is modified from Bronk Ramsey (2017), with calibration curve data from Reimer et al. (2013).

which complicates dating of landslides that occurred during these episodes (Figure 2; Reimer et al., 2009). Further complicating precision, $^{14}$C dating commonly neglects the residence time of detrital material, which may remain on the landscape undisturbed for millennia prior to landslide emplacement (Clague, 2015; Gavin, 2003, 2001; Trumbore, 2000). The $^{14}$C method of dating additionally does not consider reactivation of deep-seated landslides; a $^{14}$C date for a reactivated landslide may provide the age of the initial failure, not the most recent event. Finally, $^{14}$C dating often relies on dating charcoal, which is subject to high uncertainty due to high postfire residence times (Gavin, 2003, 2001; Reneau et al., 1986; Reneau and Dietrich, 1991; Trumbore, 2000). Ultimately, $^{14}$C dating cannot provide the dating precision necessary to connect landslide failures to a specific event, or to identify clustering of landslides associated with a particular triggering event.

## 2. Study Area

### 2.1. Oregon Coast Range

The Oregon Coast Range is a steep and dissected mountain range subject to uplift along the Cascadia subduction zone. The Oregon Coast Range has cool, wet winters, during which the majority of the annual 1–2 m of precipitation falls, and dry, warm summers (PRISM Climate Group, 2016). The hillslopes are soil-mantled and support tree populations of Douglas fir (*Pseudotsuga menziesii*) and western hemlock (*Tsuga heterophylla*). The predominant lithology in the Oregon Coast Range is a ~3-km-thick interbedded turbidite sequence of Eocene sandstones and siltstones known as the Tyee Formation, which rests on accreted volcanic terranes (Heller and Dickinson, 1985; Wells et al., 1998). Previous work has generally placed the provenance of the sediments within

the Tyee Formation as either the Idaho Batholith or the Klamath Mountains (Dumitru et al., 2013; Heller et al., 1985; Heller and Dickinson, 1985). Since deposition in the Eocene and subsequent uplift in the Miocene, the Tyee Formation has experienced 40° to 70° of clockwise rotation at 1°/m.y., primarily due to oblique subduction and extension in the Basin and Range Province and northward migration of the Sierra Nevada block (Heller and Ryberg, 1983; McNeill et al., 2000; Wells et al., 1998; Wells and Heller, 1988; Wells and McCaffrey, 2013). This rotation has resulted in the deeper marine facies of the Tyee Formation, and hence a higher proportion of siltstone to sandstone, in the northern portion of the Oregon Coast Range, with a higher proportion of sandstone remaining in the south (Roering et al., 2005). This rotation also places the Oregon Coast Range in a compressive regime, resulting in minor deformation and folding, with dips along fold limbs typically less than 15°–20° (Baldwin, 1956).

On the steep ridge-valley terrain in the Oregon Coast Range, soils are produced from bedrock primarily through tree throw and are thinnest (∼0.5 m) on the ridges and adjacent hillslopes (Dietrich and Dunne, 1978). Soils thicken (∼1–2 m) in the unchanneled valleys, which are periodically evacuated by shallow landslides that often mobilize into debris flows (Benda and Dunne, 1997; Dietrich and Dunne, 1978; Stock and Dietrich, 2003). The Oregon Coast Range has often been described as an example of a steady-state landscape, where uplift is balanced by erosion (Montgomery, 2001; Reneau and Dietrich, 1991). Studies of cosmogenic erosion rates have shown that the Oregon Coast Range is eroding at ∼0.05–0.14 mm yr–1 (Balco et al., 2013; Heimsath et al., 2001; Penserini et al., 2017), while marine terraces along the coast suggest uplift rates of 0.05–0.3 mm yr$^{-1}$ (Kelsey et al., 1994, 1996; Kelsey and Bockheim, 1994), with strath

terraces suggesting similar rates of 0.1–0.2 mm yr$^{-1}$ (Personius, 1995). The extent to

which these uplift rates penetrate inland is generally poorly constrained, although

Penserini et al. (2017) found morphologic evidence that erosion and uplift rates,

assuming steady erosion, experience a modest increase in the eastward (inland) direction.

The extent to which spatial variability in uplift rates correlates with deep-seated

landslides in the Oregon Coast Range is poorly known.

Deep-seated landslides are most common on dip slopes of sandstone-siltstone

turbidite interbeds of the Tyee Formation (Roering et al., 2005). The density of deep-

seated sliding varies with latitude, reflecting the relative dominance of sandstone and

siltstone interbeds. Specifically, the southern portion of the Oregon Coast Range, where

sandstone is the more common component of the Tyee Formation, exhibits fewer large

landslides (Burns et al., 2012; Roering et al., 2005). Because the spatial distribution of

landslides correlates strongly with lithology and geologic structure rather than the inland

attenuation of ground motion from subduction zone earthquakes (Madin and Burns, 2013;

Olsen et al., 2015), the application of coseismic landslide model predictions is complex,

especially given the broad range of landslide triggering mechanisms (Allstadt et al.,

2013).

The paucity of historic deep-seated landslide activity and the potentially broad

range of landslide ages complicate efforts to link landslides with specific seismic or

hydrologic events. Specifically, despite the existence of >40,000 deep-seated landslides

in the Oregon Coast Range (Burns and Watzig, 2014), few to none have been observed to

fail catastrophically or form landslide dams, with the notable exception being the Drift

Creek landslide reactivation in 1975, which followed heavy and prolonged rain (Thrall et

al., 1980). The landslide responsible for the formation of Triangle Lake occurred ca. 50

ka (Marshall et al., 2017), and soil residence times suggest some of the largest deep-

seated landslides are on the order of 100 ka or older (Almond et al., 2007). Such an

extensive history of landsliding may reflect numerous individual triggering events (or

episodes of activity) for each landslide. More importantly, however, the tendency for

landslides to experience reactivation enables us to test whether earthquakes and storms

act as potential triggers using dendrochronology and other dating methods.

*2.2. Landslide-Dammed Lakes*

A causal relation between slope failure and triggering events such as subduction

zone earthquakes or large storms requires the acquisition of landslide ages with precision

greater than that provided by $^{14}$C dating of detrital materials, which typically has >10 yr

standard error and may neglect residence time and the origin of the wood within the tree.

Dendrochronology is the only known method with the potential to estimate landslide age

with annual (or potentially subannual) precision. There exist dozens of landslide-dammed

lakes in western Oregon with standing Douglas fir snags, or "ghost forests" (Figure 1).

Tree rings from these standing Douglas fir snags can be analyzed to date the year of death

of the trees, reminiscent of the paleoseismic work of Yamaguchi et al. (1997), who used

drowned trees on the coast of Cascadia to constrain the timing of the A.D. 26 January

1700 earthquake. These Oregon Coast Range ghost forests died when large landslides

clogged proximal valley bottoms, damming stream channels. Rapid valley inundation

followed landslide dam emplacement, resulting in the death of the submerged trees.

Landslide dam emplacement also initiated alluviation upstream of the dam, which is

additionally useful for estimating time since landslide emplacement. In the Oregon Coast

15

Range, light detection and ranging (LiDAR) analysis revealed a multitude of such

landslide-dammed lakes, with deposit morphology suggesting triggering within the last

several hundred years (Figures 3 and 4). These landslide-dammed lakes afford a unique

opportunity to determine whether the timing of the landslides corresponds with major

Cascadia earthquakes.

## 3. Methods

### 3.1. Site Selection and Mapping

Using high-resolution airborne LiDAR-derived bare earth digital elevation models

(DEMs; Oregon Department of Geology and Mineral Industries, 2012, 2015), we located

>200 sites with topographic evidence of landslide-dammed lakes throughout the Oregon

Coast Range. These sites were investigated further to clarify those that appear young

enough to have been potentially associated with the A.D. 1700 earthquake (Atwater et al.,

2005). We selected landslide-dammed lake sites that displayed characteristics that are

consistent with relatively recent (hundreds of years) landslide movement, in particular,

fresh morphologic features such as sharp headscarps and minimal channel incision of the

deposit (Booth et al., 2017, 2009; Burns and Madin, 2009; LaHusen et al., 2016). Sites

that experienced a single damming event without obvious subsequent reactivation were

prioritized. We examined each potential landslide dam for the presence of an existing

lake or marsh upstream of the deposit, and we used aerial imagery (USDA, 2000) to

locate standing snags. Lakes were prioritized according to land ownership and

accessibility to trees, the presence of delta progradation, and marginal sedimentation,

aiding in access.

We selected two landslide-dammed lakes in the Oregon Coast Range for dating, Klickitat Lake (44.480°N, 123.659°W) and Wasson Lake (43.748°N, 123.795°W). Both slides appear to have experienced a single damming event and occurred on hillslopes within the Tyee Formation, where bedding is primarily subhorizontal, although at Klickitat Lake, there is a higher proportion of siltstone to sandstone (Roering et al., 2005), and the slide occurred on a shallowly dipping slope (Schlicker et al., 1973). Though deep-seated, both landslides are elongate and have a relatively long runout and fluid-like appearance (Cruden and Varnes, 1996). They are primarily composed of blocky and weathered Tyee Formation clasts within a matrix of colluvial sand and silt. Once we selected Klickitat and Wasson Lakes for field reconnaissance, we completed detailed mapping of the landslide features, current and estimated high-lake extent, and alluvium retained upstream of the landslide dam. Initial field data and sample acquisition included: confirming the presence of the landslide dam, standing water, alluvium, and standing snags; verifying the survival of bark to confirm the existence of the outer growth increment and noting accessibility of standing snags for future sampling; and sampling standing snags' outer rings, detrital organics from within the landslide deposit for $^{14}$C analysis, and increment cores from old-growth living trees on the landslide surface.

### 3.2. Snag Sampling and Measurement

We collected samples from dead Douglas fir trees at Klickitat Lake and Wasson Lake (Table 1). Where Douglas fir snags were readily accessible from shore, we excavated the base of each tree to expose fresh bark, sampling just below waterline for higher preservation potential. Bark attached to the last growth increment is crucial for determining an accurate year (and potentially season) of death, as the interface between

the bark and outermost growth ring demarcates the termination of the growth record. A lack of bark does not preclude dating of the landslide, though the calculated age must be considered a maximum age. A licensed sawyer extracted slabs or wedges at each tree; each slab ideally included >100 rings with bark at the outer edge and was sufficiently wide (>20 cm) relative to tree diameter to account for any variability in ring width around the tree. Care was taken to avoid sampling portions of trees with abnormal growth patterns potentially from fire damage or limb growth. We reburied any excavated portions of the trees to reduce visual impact. Slabs were promptly dried to reduce mold growth and preserve the possibility of radiocarbon dating.

We used the dendrochronology technique of cross-dating to establish the calendar year of death from drowned snags, and thus the age of the landslide damming event. As trees grow, limiting factors such as drought result in synchronous, time-specific growth patterns among individuals of a given species and region (Bekker et al., 2018; Douglass, 1941; Yamaguchi et al., 1997). Black et al. (2015) generated three >400 yr Douglas fir chronologies for the Oregon Coast Range (Figure 1) and four >800 yr chronologies in the western Cascade Range that revealed strong regional correlation. We cross-dated the ring measurements from ghost forest trees at landslide-dammed lakes against both locations to determine the timing of death, which corresponds to the calendar year of the last growth increment. We were often able to estimate the season of death by the extent to which the final increment formed; termination of growth during formation of dark, late wood suggests death in the late summer to winter, while the partial development of light, early wood implies a death in late winter to spring (Studhalter, 1956).

**Table 1**. **Sample Locations, Western Oregon**

| Sample Type | [14]C sample name (Figures 9, 10) | Location | |
| --- | --- | --- | --- |
| | | Lat (N) | Long (W) |
| Wasson Lake | | | |
| Standing snag <u>and</u> [14]C | WL1, 2 | 43.7484 | 123.7946 |
| Standing snag | N.A. | 43.7485 | 123.7954 |
| Standing snag | N.A. | 43.7477 | 123.7948 |
| Detrital [14]C (5 samples) | WL3, WL4, WL5, WL6, WL7 | 43.7478 | 123.7969 |
| Live core | N.A. | 43.7465 | 123.7977 |
| Live core | N.A. | 43.7466 | 123.7978 |
| Live core | N.A. | 43.7476 | 123.7975 |
| Live core | N.A. | 43.7480 | 123.7970 |
| | | | |
| Klickitat Lake | | | |
| Standing snag | N.A. | 44.4798 | 123.6584 |
| Standing snag | N.A. | 44.4795 | 123.6582 |
| Standing snag | N.A. | 44.4792 | 123.6583 |
| Standing snag | N.A. | 44.4794 | 123.6582 |
| Standing snag | N.A. | 44.4799 | 123.6584 |
| Standing snag | N.A. | 44.4800 | 123.6584 |
| Standing snag bark [14]C | KL1 | 44.4808 | 123.6600 |
| Standing snag bark [14]C | KL2 | 44.4807 | 123.6595 |
| Buried log [14]C (2 samples) | KL3 | 44.4772 | 123.6536 |
| Detrital [14]C (3 samples) | KL4, KL5, KL6 | 44.4783 | 123.6560 |
| Live core, DBH = 156.2 cm | N.A. | 44.4770 | 123.6548 |
| Live core, DBH = 130.3 cm | N.A. | 44.4771 | 123.6546 |
| Live core, DBH = 168.1 cm | N.A. | 44.4769 | 123.6548 |
| Live core, DBH = 157.8 cm | N.A. | 44.4771 | 123.6547 |
| Live core, DBH = 158.4 cm | N.A. | 44.4770 | 123.6550 |
| Live core, DBH = 156.2 cm | N.A. | 44.4784 | 123.6550 |
| Live core, DBH = 76 cm | N.A. | 44.4786 | 123.6572 |
| Live core, DBH = 161 cm | N.A. | 44.4785 | 123.6554 |
| Live core, DBH = 148.1 cm | N.A. | 44.4784 | 123.6553 |
| Live core, DBH = 136 cm | N.A. | 44.4787 | 123.6560 |

After collecting and drying each slab, we sanded the slab surfaces progressively

finer, finishing at 400 grit and adding a final polish with 12 μm lapping film. Samples

within a given site were visually cross-dated using the list-year technique (Yamaguchi,

1991). Next, we used high-resolution scans (>2400 dpi) of slab surfaces to measure rings

with the dendrochronology software CooRecorder (Larsson, 2013). Each slab was measured twice along different transects to account for any growth irregularities around the circumference of the tree. Using the tree-ring software CDendro (Larsson, 2013), high-frequency, year-to-year variability was isolated within each measurement time series. These high-frequency patterns, which meet the statistical assumption of serial independence, were first compared among measurement time series within each site. Correlation coefficients were generated, as were "*T* tests," which compensate for differences in the number of overlapping years, calculated as

$$T\ value = c\sqrt{\frac{n-2}{1-c^2}},\qquad(1)$$

where $c$ is the correlation coefficient, and $n$ is the number of overlapping years (Larsson, 2013). Correlation and *T* tests were lagged forward and backward over as many years as possible while maintaining a minimum of 30 yr of overlap. Correct dating was established if the correlation coefficient was highly significant ($p < 0.01$) and it and the *T*-test value were conspicuously greater than that of any other lag.

Measurement time series could be dated relative to one another within each site, but that did not provide information regarding the calendar years over which the trees lived. To generate dates tied to calendar year, the high-frequency variability from each measurement time series (that had been dated relative to one another) was averaged within the site. This floating mean chronology was then compared to the high-frequency variability from living trees at Marys Peak in the Oregon Coast Range (Black et al., 2015) using lagged correlations and *T*-test values. A lake was considered dated if there was a conspicuously prominent, highly significant ($p < 0.01$) correlation coefficient and

*T*-test value between the dead ghost forest chronology and the chronology generated from live-collected trees (Figures 6, 7, and 8). An exact year of tree death could be established if the wood immediately under the bark was well preserved, and confidence in the date of the landslide event was increased if multiple trees at a site died in the same year.

*3.3. Live Tree Coring*

Some of the landslide deposits at landslide-dammed lakes in the Oregon Coast Range host live old-growth Douglas fir trees. These trees denote the minimum age of the landslide, as old-growth stands are unlikely to survive large, deep-seated landslide failures (Clague, 2015). Live old growth is particularly useful at some landslide-dammed lakes where drowned snags are poorly preserved and have no visible bark to demarcate the outer growth ring. No statistical correlation with existing tree-ring chronologies is required with this method, as the age of the trees simply provides the minimum age of the landslide. The ecesis interval, or time between landslide occurrence and tree establishment, separates the age of the trees and the timing of the landslide and can span from a couple years to a century, depending on the landscape (Clague, 2015; Pierson, 2007). We used increment borers to collect 18 cores from 10 live Douglas fir trees at Klickitat Lake and four cores from four western hemlock trees at Wasson Lake to compare to the dendrochronology-derived age of the standing snags (Table 1; Figures 9 and 10). While this method is limited by the availability of old-growth stands, which currently exist as a minor component of the harvest patchwork in the Oregon Coast Range, it remains a useful tool when used in concert with dendrochronology and radiocarbon dating.

## 4. $^{14}$C Dating: Tree Rings

We collected wood samples from slabs extracted from standing snags for $^{14}$C analysis in order to corroborate the age of the landslide derived from dendrochronological techniques (Pringle, 2014; Schuster et al., 1992). As a tree grows, each progressive growth ring consumes and stores the relative concentration of $^{14}$C present in the atmosphere. As such, tree rings record annual variations in atmospheric isotopic composition and can serve as a means to tune the radiocarbon calibration curve (Reimer et al., 2013). Because each ring precisely denotes a single year of growth in the tree, derived radiocarbon ages can be constrained by the calendar year of growth of each ring, a process known as "wiggle matching" (Reimer et al., 2009). This process is particularly useful for improved $^{14}$C dating of materials that are relatively young (<500 yr), as the radiocarbon calibration curve oscillates significantly throughout this time period (Figure 2).

We collected three wood samples for $^{14}$C analysis from a slab from Wasson Lake, and two samples from a buried log in the landslide deposit at Klickitat Lake (Table 1). Each of the slabs from Wasson Lake internally cross-correlate, so we are confident that the wood samples from only one tree are representative of the other slabs. For the Wasson Lake slab, we sampled wood from the outermost ring and rings 99 and 180 counted from the outside edge, rings sufficiently separated to effectively utilize Bayesian statistical methods. We used OxCal, a Bayesian statistical tool, to convert $^{14}$C years to calendar years and narrow the range of potential ages using wiggle matching (Bronk Ramsey, 1995). Wiggle matching utilizes the sequential order and spacing of the rings to best fit the $^{14}$C ages, including the error range on the radiocarbon calibration curve, to a

constrained calendar year probability distribution function (PDF) for each sample (Bronk

Ramsey, 1995, 2009). For example, if the PDFs of rings 99 and 180 overlap, OxCal

constrains the range of possible ages by recognizing that ring 99 is known to be exactly

81 yr older than ring 180, thus shrinking the range of possible calendar year ages. We

followed a similar approach for the buried log at Klickitat Lake. We collected the

outermost preserved ring and wood from a ring ∼52 rings inward. Given the decayed

state of the wood, it was unclear how many rings may be missing from the outer edge of

the tree, so the wiggle-matching derived age must be considered a maximum age of the

landslide deposit. The $^{14}$C ages from standing snags at Wasson Lake and the buried log at

Klickitat Lake are also useful for interpreting the ages of the multitude of landslides in

the Oregon Coast Range that lack dams and for which only deposits can be identified.

## 5. $^{14}$C Dating: Landslide Deposit Detritus

To test for radiocarbon inheritance and constrain how residence time of variable

detritus types biases calculated landslide ages, we preferentially selected small organic

debris including charcoal, wood, and twigs. Traditional methods for dating landslides

require collecting organic material from the landslide deposit, which is then dated using

$^{14}$C dating. We followed this approach at Klickitat and Wasson Lakes, and we collected

five pieces of detrital carbon from each deposit for dating. Where large pieces of wood or

stumps were found, we sampled the outermost rings in order to derive the youngest and

most accurate date possible. The various materials we sampled, including pieces of wood,

twigs, leaves, and charcoal, were intended to constrain and demonstrate the types of

materials that are considered preferable for dating landslides. Alternative materials such

23

as wood or charcoal bias the calculated age relative to the dendrochronologically derived date, which should be the most contemporaneous with landslide occurrence.

*5.1. Sedimentation Rate Age*

To estimate the number of years required to retain the volume of sediment behind landslide dams, we utilized LiDAR-derived, bare earth, 1 m DEMs and existing erosion rate data for the Oregon Coast Range (Butterfield et al., 2015). Many previous studies have investigated the magnitude of erosion in the Oregon Coast Range, finding erosion rate values from cosmogenic nuclides spanning a range from 0.05 mm yr$^{-1}$ to 0.2 mm yr$^{-1}$ (Bierman et al., 2001; Heimsath et al., 2001 Marshall et al., 2015; Penserini et al., 2017; Reneau and Dietrich, 1991); Brown and Krygier (1971) and Beschta (1978) measured sediment yield rates between 0.05 and 0.08 mm yr$^{-1}$. Hence, based on these previously published erosion rates, we selected a range of erosion rate values from 0.05 to 0.2 mm yr$^{-1}$ to use in our analysis to determine an approximate time scale of alluvial backfilling.

We used the equation

$$T = \frac{V}{A \cdot E},$$
(2)

at Wasson and Klickitat Lakes to calculate the time, *T*, required for deposition of the observed sediment volume, *V*, given the upstream drainage area, *A*, and erosion rate, *E*. In Equation 2, we assume the following: (1) The landslide dam is perfectly efficient at trapping sediment, (2) all sediment impounded upstream is a result of landslide emplacement, (3) and millennial erosion rates can be effectively applied over the time scale of sedimentation in these basins (<200 yr). Despite the apparent limitation of these assumptions (e.g., Minear and Kondolf, 2009; Marineau and Wright, 2017), the
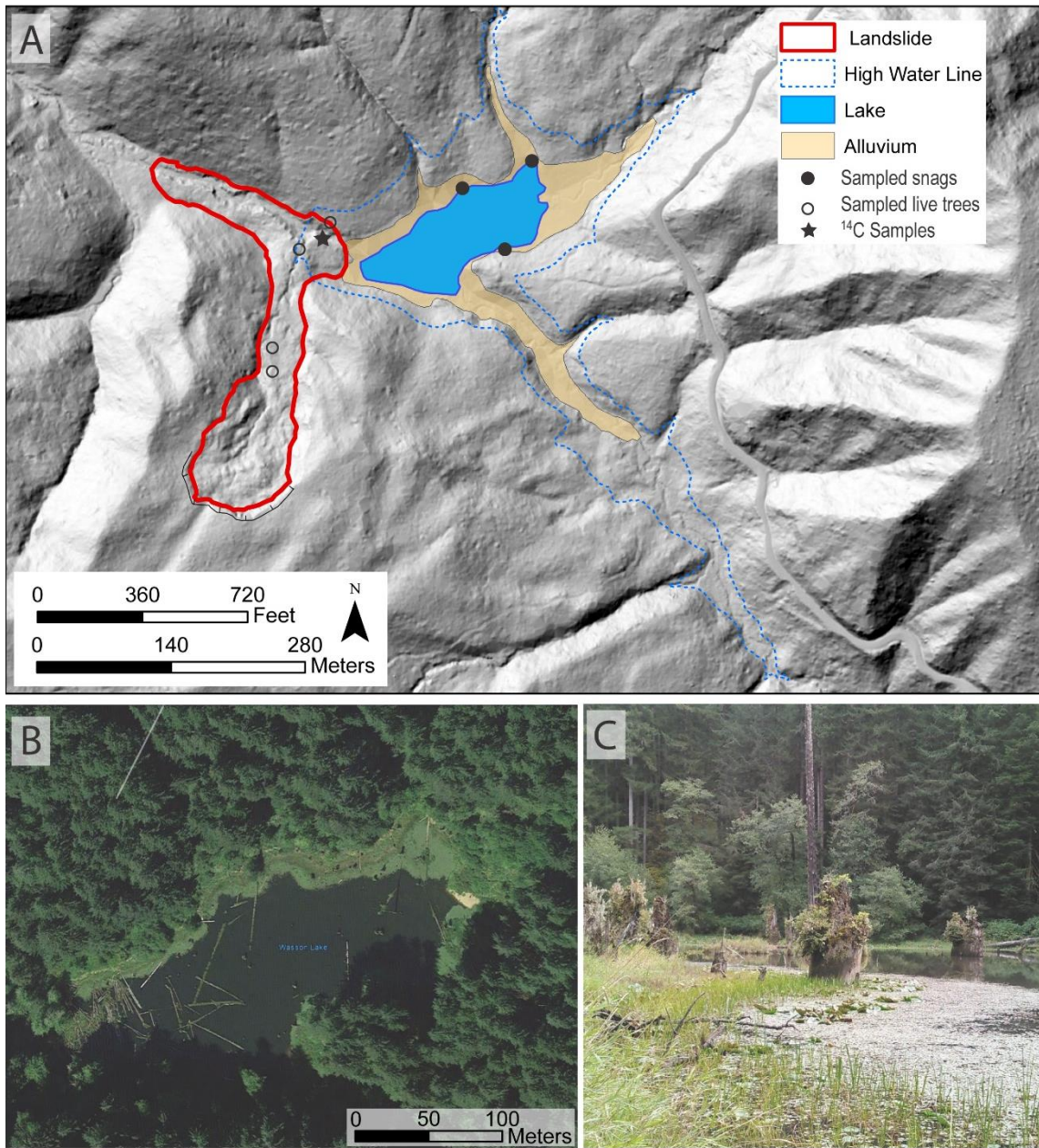
**Figure 3**. **Wasson Lake.** (A) Map of the Wasson Lake site (43.748°N, 123.795°W), including the current and estimated high water levels, with the landslide dam outlined in red. Sampled drowned snags are denoted by filled circles, and cored live trees are denoted by empty circles; ^{14}C samples are labeled by filled star. Note that all detrital ^{14}C samples fall at single location in landslide deposit. (B) Aerial imagery of Wasson Lake. (C) Standing Douglas fir snags in Wasson Lake. Snag nearest to camera is ~2.5 m tall.
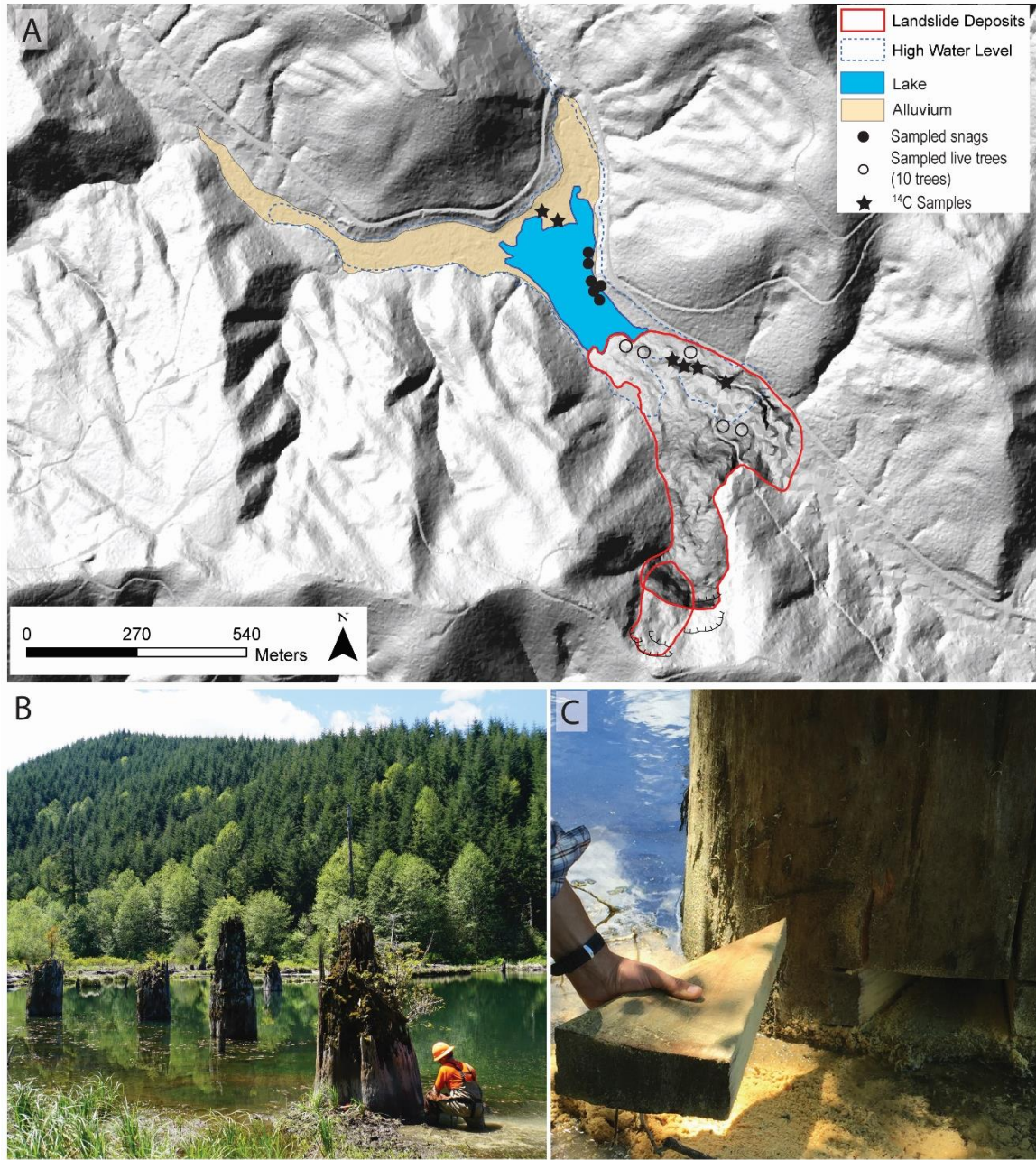
**Figure 4**. **Klickitat Lake.** (A) Map of the Klickitat Lake site (44.480°N, 123.659°W), including the current and estimated high water levels, with the landslide dam outlined in red. Sampled drowned snags are denoted by filled circles. Live-cored trees are denoted as empty circles. Note that multiple trees fit within individual circles (Table 1). Filled stars are ^{14}C sample sites. (B) Sampling Douglas fir snags in Klickitat Lake. (C) Example of slab extracted from standing snag.

approximate landslide ages that we derived using this method served as a powerful corroborative and reconnaissance tool. In addition, we assumed that the lakes continue to trap sediments to the present day. At Klickitat Lake, most of the incision at the outlet, where the channel is lined with riprap, is due to anthropogenic lowering of lake level during road construction in the mid-twentieth century. In addition, we observed modern marginal sedimentation at Klickitat Lake from aerial imagery and field observations. Furthermore, at Wasson Lake, the landslide pushed the channel to the north side of the valley, where it currently flows over bedrock on the prelandslide proximal hillslope. While some incision has occurred at the outlet, which is evident by an earlier highstand of the lake (Figure 3), the potential progressive or instantaneous nature of lake lowering is unclear. In any case, we used the modern lake level to calculate impounded sediment volume, so any drastic change in lake level will not affect the calculated age.

We calculated the drainage area above the landslide dam using 1 m DEMs in ArcMap. In order to calculate the sediment volume that has been deposited in the lakes since landslide emplacement, we estimated the pre–sediment infill topography. We drew surface elevation drainage and cross-section profiles above and below the alluvium extent, which we used to estimate the prelandslide drainage centerline elevation. We assumed all valleys to be v-shaped prior to sediment infilling. While we observe that the valley bottoms are not v-shaped, the catchment area at both Klickitat and Wasson Lake is small enough that any variability in valley width is minor and will not greatly affect our calculations (May et al., 2013). The outer edge of the alluvium elevation was extracted as points from the current surface DEM, which were then combined and interpreted as a prelandslide dam DEM. We subtracted this prelandslide dam DEM from the modern

27
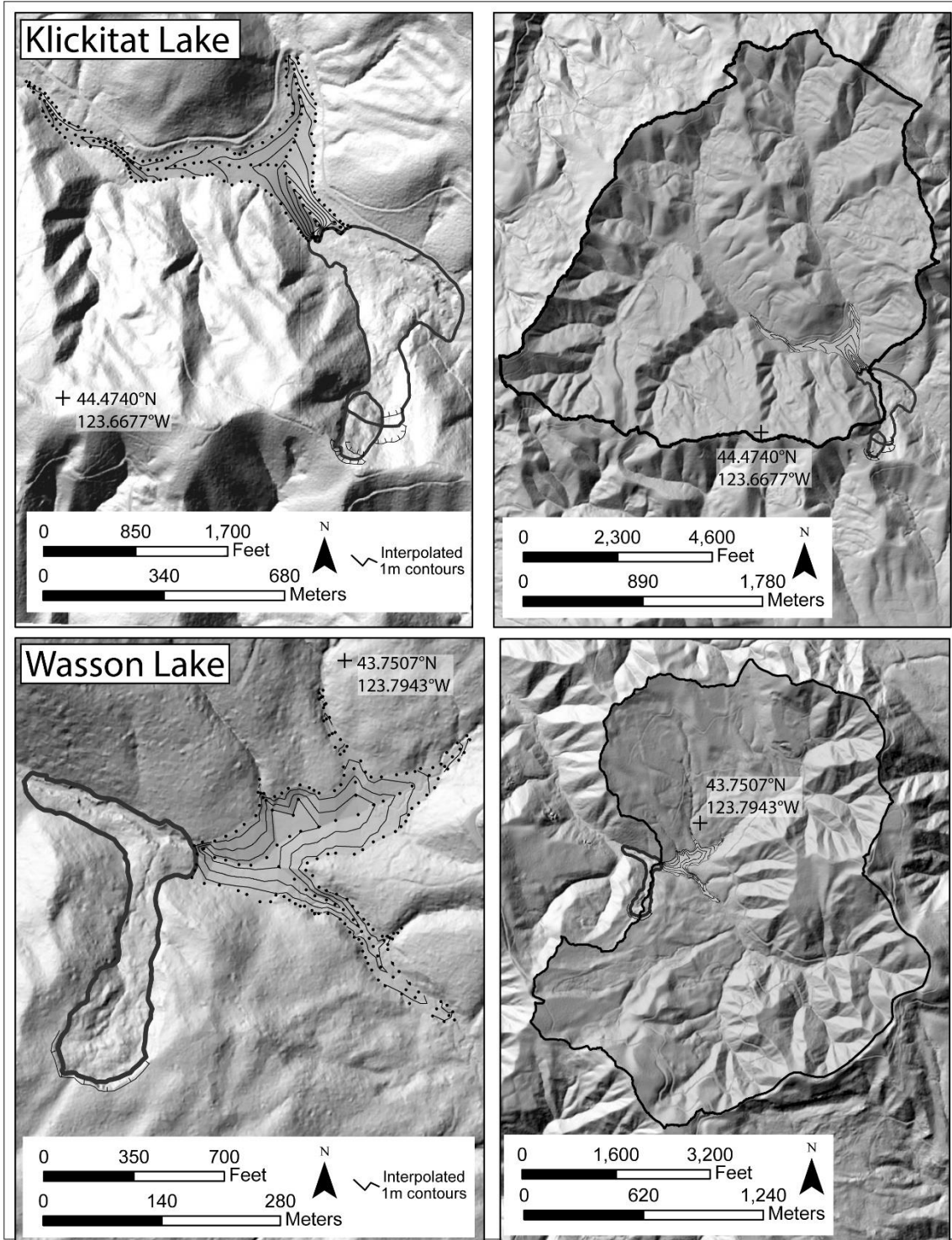
**Figure 5**. **Maps of the estimated pre–sediment infill digital elevation model** (DEM; with interpolated 1 m contours) and elevation points (black dots) used to calculate landslide age from valley alluviation at Klickitat and Wasson Lakes. Watershed extent above landslide dam is outlined in black.

DEM (Figure 5), which resulted in the total depth of lake water and sediment. We estimated an average lake depth from field observations, which, along with lake surface area, provided a total lake volume. We removed the lake volume from the total volume of the lake and sediment to yield the total sediment volume.

## 6. Results

### 6.1. Klickitat Lake

We measured the rings from seven slabs and cross-dated the slabs against each other to ensure that the trees at Klickitat Lake lived contemporaneously. The eight measured transects on the seven slabs have a series intercorrelation coefficient value of 0.639. After comparing the mean, undated Klickitat chronology against the Marys Peak chronology (Black et al., 2015), we determined the year of death to be in the winter of A.D. 1751–1752. The correlation coefficient for the floating chronology at Klickitat Lake and the Douglas fir chronology from Marys Peak was 0.51 with a *T* value of 8.1, values which are conspicuously high relative to other lagged dates (Figures 6 and 7). Using the cores that we collected from live trees on the surface of the landslide, we observed that the oldest trees began growing between A.D. 1760 and 1770, approximately a decade after the landslide occurred (Figure 9). We are confident that the trees measured here accurately reflect the age of the landslide, as the trees on the landslide surface cannot be older than the lake.

To analyze the impact of radiocarbon inheritance on organic material in landslides, we collected and analyzed organic detrital material found within the landslide deposit, including charcoal and woody debris ranging from twigs to pieces of entire trees.
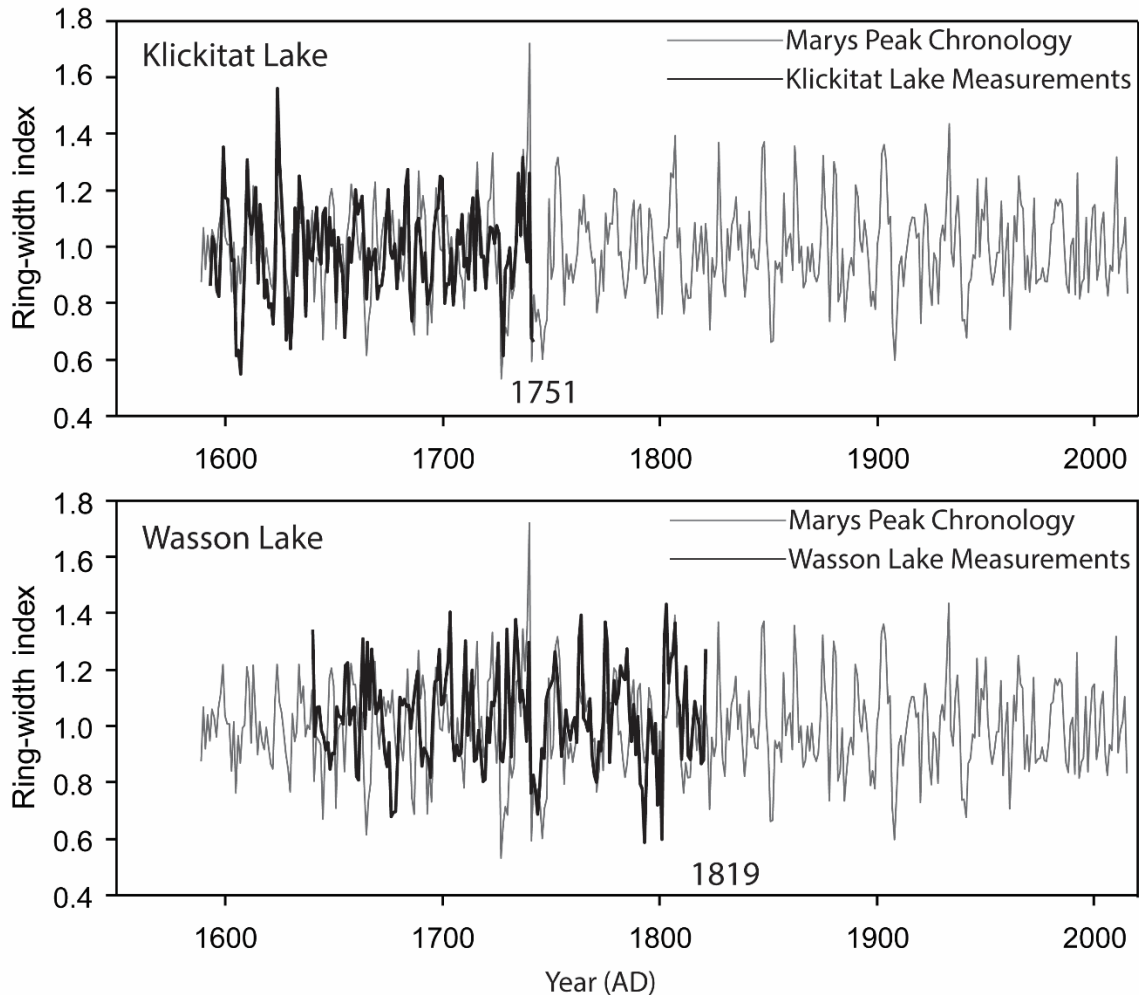
**Figure 6**. **Measurement time series.** Examples of the measurement time series for Klickitat and Wasson Lakes (black) lagged and fit against the Marys Peak chronology (gray). Lagged correlation coefficient and *T* values corresponding to these two dates are conspicuously high relative to other potential years (Figures 7 and 8), thus showing the year of death of the trees and accurate dating of the landslide.

We found that collected detrital material at Klickitat Lake provides a wide range of ages. Specifically, two detrital charcoal samples provided ages of ca. 4400–4200 B.C. and A.D. 800–1000, while woody material provided an age spanning from the early A.D. 1600s to near-present. We also collected two samples ∼52 rings apart in a log buried in the landslide deposit. These two wiggle-matched samples suggest a maximum landslide occurrence during the mid- to late A.D. 1600s (Figure 9). Thus, ^{14}C dating of organic

30

material from the landslide deposit suggests a landslide age with high uncertainty, spanning over 6000 yr.

Using the sediment accumulation analysis above the dam, we determined an age range spanning from 330 to 82 yr. The range of potential ages resulted from applying multiple sediment accumulation rates. Thus, the time required for the estimated volume of sediment to accumulate behind the landslide dam translates to landslide dam emplacement between A.D. 1688 and 1936, which brackets our calculated dendro-chronology age of A.D. 1751 (Figure 9).

*6.2. Wasson Lake*

We utilized multiple techniques to accurately constrain the age of the slide that created Wasson Lake. Following the same technique as Klickitat Lake, we measured and cross-dated tree rings from three slabs at Wasson Lake and found the year of death for the trees to be the winter of A.D. 1819–1820. The correlation coefficient for the floating chronology from three samples at Wasson Lake and the Douglas fir chronology from Marys Peak was 0.38, corresponding to a *T* value of 6.0, values that are highly statistically significant ($p < 0.01$) and conspicuously greater than all other correlations (Figure 8). Similar to Klickitat Lake, we are confident that rapid valley inundation following landslide emplacement killed the trees prior to further growth increments being added. We also observed from increment cores that live, old-growth western hemlock on the landslide surface began growing in the mid-1840s to early 1850s, a similar ecesis interval to that observed at Klickitat Lake.
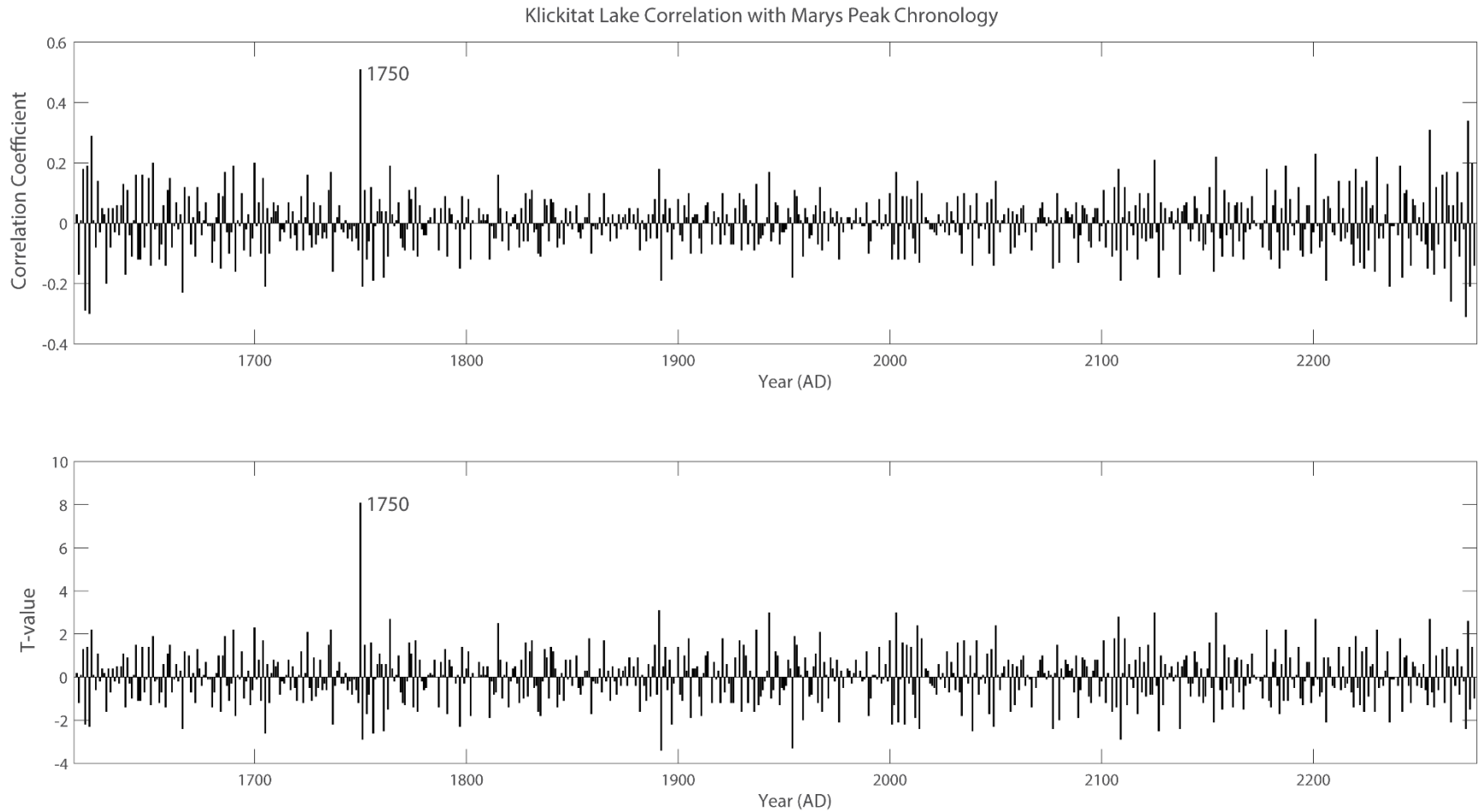
**Figure 7**. **Correlation plots for floating chronology generated at Klickitat Lake lagged against chronology from Marys Peak, Oregon** (Black et al., 2015). Both the correlation coefficient and *T* value (correlation coefficient normalized by the sample size) are significantly and conspicuously high for the year A.D. 1750, relative to other years. Note that the year A.D. 1750 corresponds to the last *measured* ring, while 1751 was the year of the last growth increment.
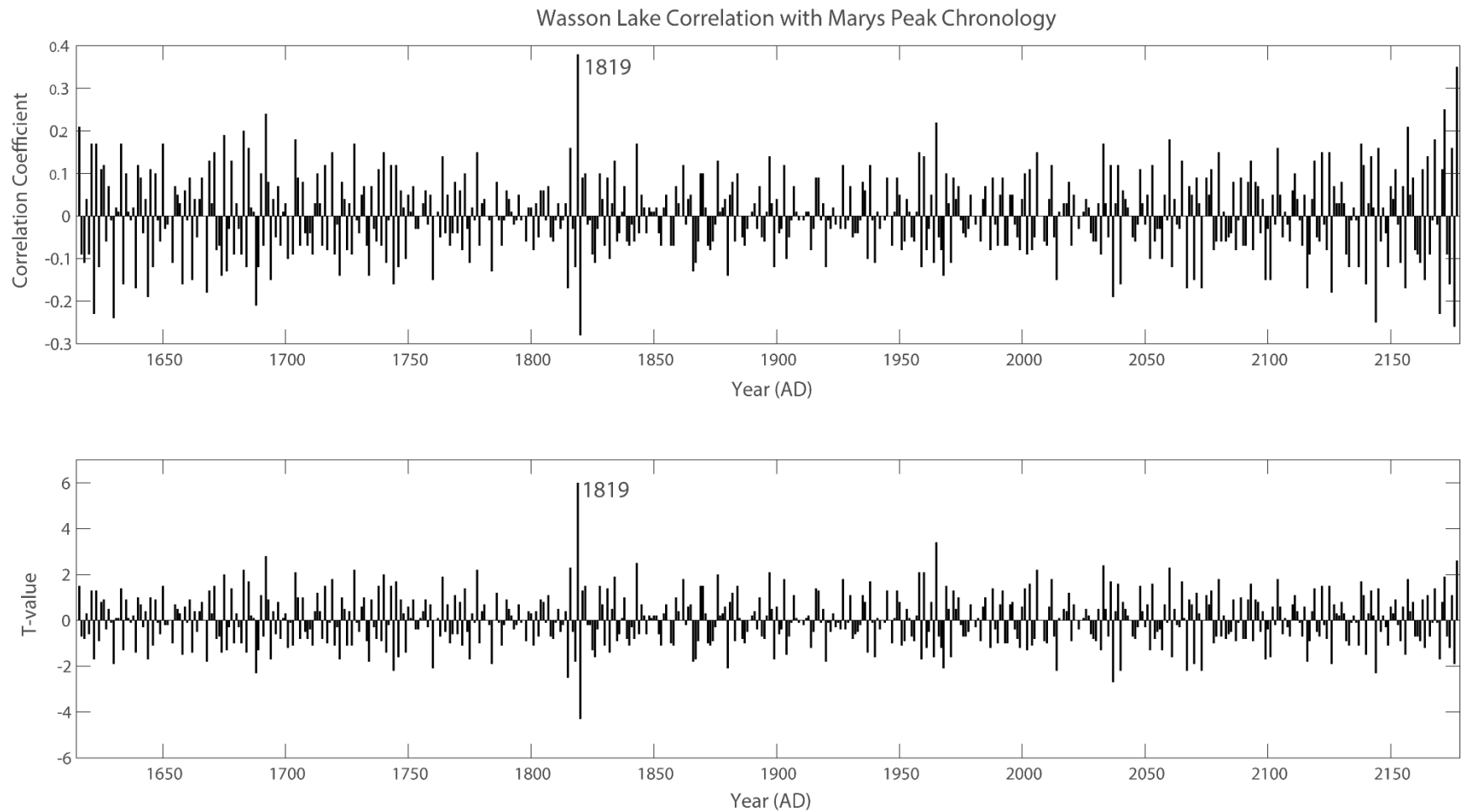
**Figure 8**. **Correlation plots for hanging chronology generated at Wasson Lake lagged against chronology from Marys Peak, Oregon** (Black et al., 2015). Both the correlation coefficient and *T* value (correlation coefficient normalized by the sample size) are significantly and conspicuously high for the year A.D. 1819 relative to other years.

33

In addition to dendrochronological analysis of slabs and minimum ages derived from live trees at Wasson Lake, we sampled three rings for radiocarbon analysis. We collected samples from a single slab and are confident that the ages derived from one tree will closely match the others, as they internally cross-date with a series intercorrelation coefficient from six measured transects on three trees of 0.659. The outermost ring yielded a modern $^{14}$C age, which was not unexpected, since the outer rings of all the slabs have undergone chemical alteration, made most apparent by discoloration in the outer ~5 cm of wood. Rings 99 and 180, however, yielded ages of $105 \pm 30$ $^{14}$C yr and $235 \pm 30$ $^{14}$C yr, respectively. These $^{14}$C ages correspond to two possible calendar year ages because each $^{14}$C age crosses the radiocarbon calibration curve at multiple points. One scenario places the age of the dead tree between A.D. 1920 and 1990 (Figure 10). However, the time of landslide occurrence at Wasson Lake is not historically documented, and the trees on the landslide began growing in the A.D. 1840s, which is much too early for landslide occurrence to be in the twentieth century. The second scenario, spanning from A.D. 1810 to 1850, is consistent with the year of death of A.D. 1819 derived from dendrochronology methods, as well as the finding that trees on the landslide deposit began growing in the 1840s to early 1850s (Figure 10). Hence, despite higher uncertainty in these ages relative to the dendrochronology ages, these two radiocarbon samples from drowned snags helped to corroborate the landslide age.

In addition to collecting radiocarbon samples from rings of standing snags, we also collected detrital samples from the Wasson Lake landslide deposit. Two detrital charcoal samples were dated to ca. 7100–6700 B.C. and 1900–1700 B.C. Two additional pieces of wood from the deposit were dated to approximately the late A.D. 1400s to
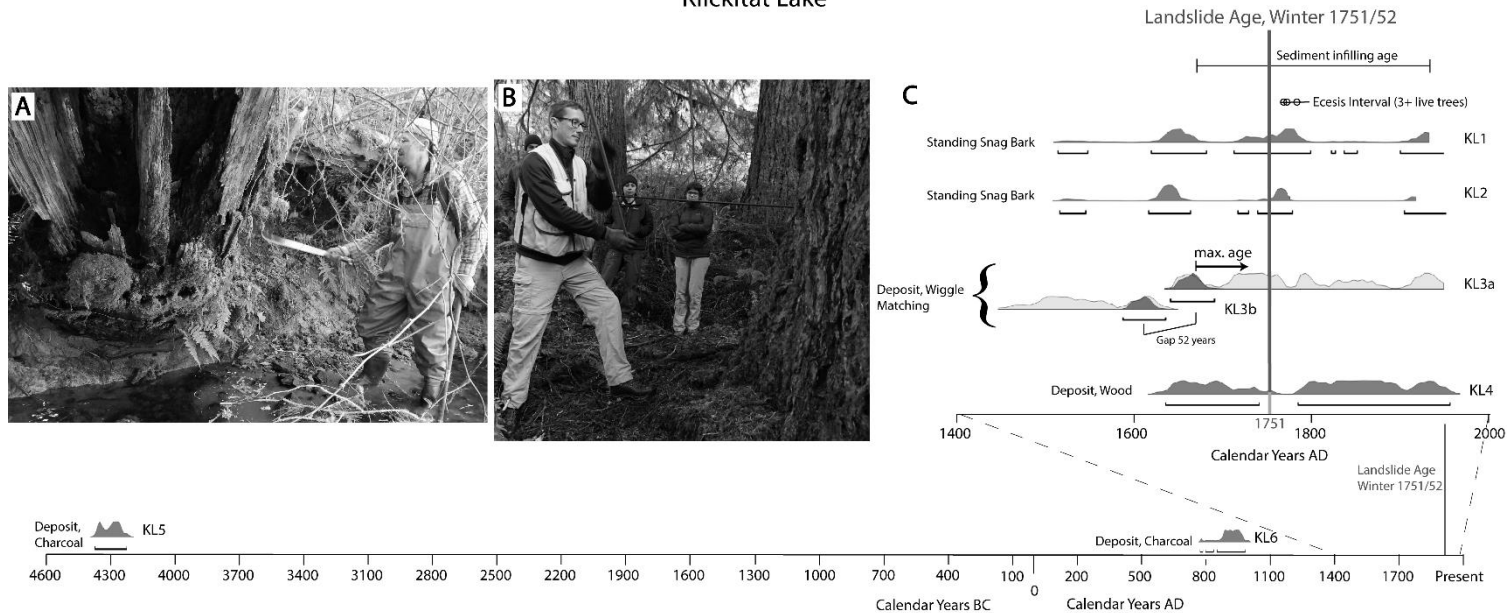
**Figure 9**. **Klickitat Lake $^{14}$C.** (A) Example of large log buried by a landslide deposit. Samples from this tree were collected from the outermost exposed wood (KL3). (B) Collection of live cores from live old growth on the landslide deposit. (C) Dating results from Klickitat Lake. Each radiocarbon sample is labeled according to the type of material (wood, bark, charcoal) and its relative location (lake, deposit). Each sample age is displayed as a probability distribution function (PDF), based on where its $^{14}$C age and error lie relative to the $^{14}$C calibration curve. Multiple PDFs for a single sample represent locations where a single radiocarbon age, including its error, intercepts the "wiggly" radiocarbon calibration curve. Sample KL3a and KL3b are wiggle-matched samples from a single tree, where wood from an inner ring (KL3b) is separated by 52 rings from an outer ring (KL3a). Wiggle matching produced two separate PDFs, which were then constrained given the 52 yr separation. The sediment infilling ages were calculated from alluviated portions of the landslide-dammed lake and valley and span over a range of potential erosion rates. Absolute landslide age from dendrochronology is represented as a vertical line in the winter of A.D. 1751–1752. The ecesis interval was determined by age of living Douglas fir trees on the landslide surface. These trees cannot be older than the dendrochronology-derived age. The cores from these trees showed that they began growing approximately a decade after landslide emplacement; at least three trees (of 10 sampled) started growing within at least 20 yr of landslide emplacement, the oldest of which began growing no later than A.D. 1770. The center of the tree (pith) was not sampled in any of these cores, so their ages are minimum ages.

35
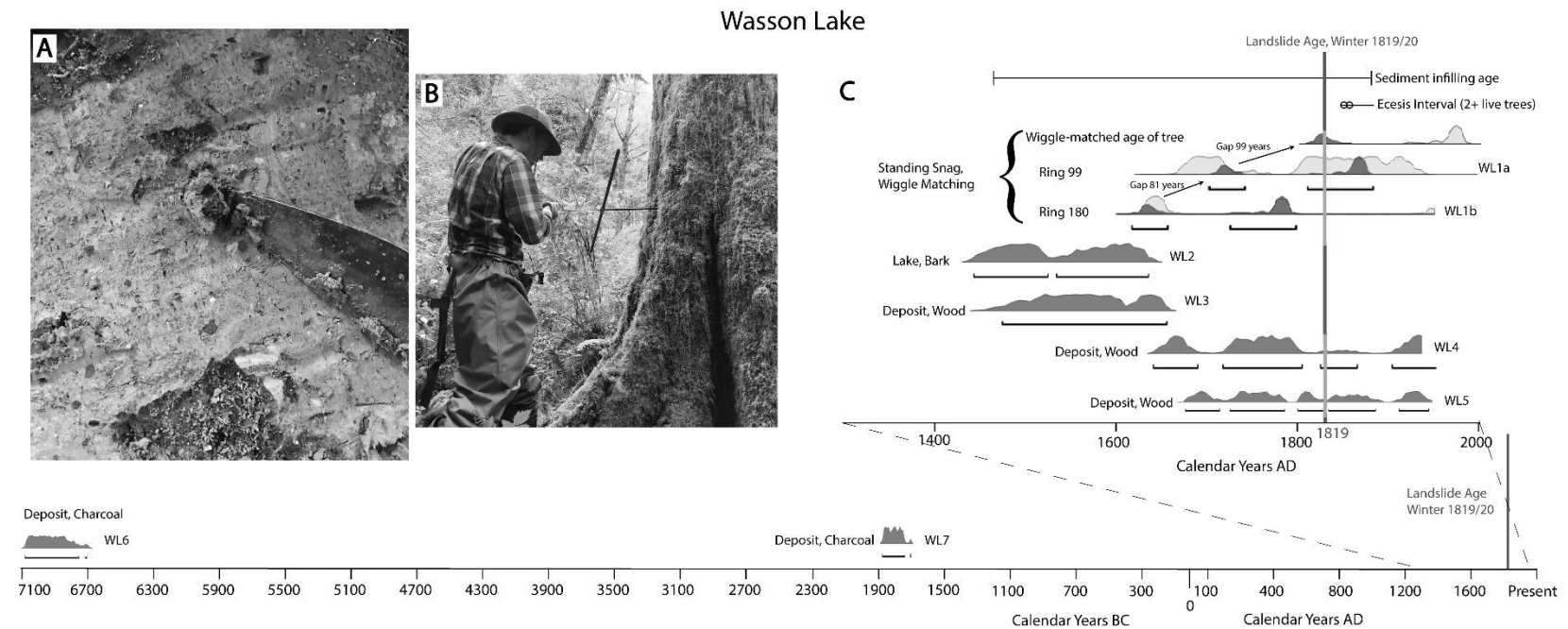
**Figure 10**. **Wasson Lake** [14]C (A) Charcoal buried in the landslide deposit at Wasson Lake. (B) Collection of cores from live old growth on the landslide deposit. (C) Dating results from Wasson Lake. Each sample is labeled according to the type of material (wood, bark, charcoal) and its relative location (lake, deposit). Each sample age is displayed as a probability distribution function (PDF), based on where its ^{14}C age and error lie relative to the ^{14}C calibration curve. Multiple PDFs for a single sample represent locations where a single radiocarbon age, including its error, intercepts the "wiggly" radiocarbon calibration curve. Wiggle matching constrains the time of death PDF by fitting the array of properly spaced radiocarbon ages of the wood samples with the radiocarbon calibration curve and then adjusting the final PDF to account for the 81 yr gap between the inner and outer rings. Counting out the final 99 yr to the edge of the tree provides the year the tree died (WL1). The sediment infilling ages were calculated from alluviated portions of the landslide-dammed lake and valley and span over a range of potential erosion rates. Absolute landslide age from dendrochronology is represented as a vertical line in the winter of A.D. 1819–1820. The ecesis interval was determined by the age of living Douglas fir trees on the landslide surface. These trees cannot be older than the dendrochronology-derived age. The cores show that at least two trees (of four sampled) started growing within at least 30 yr of landslide emplacement, the oldest of which began growing no later than A.D. 1841. The center of the tree (pith) was not sampled in any of these cores, so their ages are minimum ages.

36

middle 1600s and the middle A.D. 1600s to the near-present, respectively (Figure 10).

Bark from a standing snag in Wasson Lake also had an age ranging from the early A.D.

1400s to early 1600s. Taken together, these $^{14}$C dates would suggest a range of potential

landslide ages spanning potentially over 9000 yr.

Similar to Klickitat Lake, we estimated the age of Wasson Lake based on

sediment accumulation since landslide emplacement. Using several potential

sedimentation rates, we determined a range of 553–138 yr necessary to deposit the

calculated total volume of sediment behind the landslide dam, which translates to

landslide emplacement between A.D. 1465 and 1880, bracketing our calculated age of

A.D. 1819 (Figure 10).

**7. Discussion**

Using dendrochronology of drowned trees to date landslides in Cascadia with

high precision is a novel approach, and it provides the only means to improve our ability

to constrain the effects of past ground motion and high-magnitude precipitation events on

Cascadian landscapes (Pringle, 2014; Reynolds et al., 2015; Suter et al., 2013). We are

confident that the time of death we calculated for the ghost forests represents the age of

the landslides; valley inundation will rapidly follow landslide emplacement, as recently

observed for landslides triggered during the 2016 Kaikoura earthquake (Jibson et al.,

2018). In addition, submergence of Douglas fir roots should quickly result in tree

mortality within a matter of weeks to a couple months (Gadgil, 1971), ending ring growth

and preserving the sequence of outer rings that can be used to date events with subannual

precision. While the landslides we dated here were not contemporaneous with the A.D.

1700 Cascadia subduction zone earthquake, it may be possible that the earthquake

initially destabilized or conditioned slopes in the Oregon Coast Range, including at

Klickitat and Wasson Lakes, and then catastrophic failure occurred later (Schulz et al.,

2012), a possibility that cannot currently be confirmed. Despite the lack of convincing

contemporaneity with the A.D. 1700 event, the landslides we dated extend existing

western Oregon tree-ring chronologies and may improve understanding of the climate-

driven impacts on slope stability in the Pacific Northwest. Furthermore, given the

considerable number of deep-seated landslides in the Oregon Coast Range that remain

undated—many of which impound lakes or marshes with standing snags—our approach

provides the opportunity to develop an unprecedented landslide database in Cascadia and

beyond.

*7.1. Advantages and Pitfalls of Radiocarbon*

We utilized radiocarbon techniques to corroborate the ages of Klickitat and

Wasson Lakes that we derived from dendrochronology. While the corroboration of

landslide age with $^{14}$C dating proves useful, our results also demonstrate the limitations of

$^{14}$C methods for dating landslides precisely. When including detrital charcoal in our

analysis, our radiocarbon results provide an uncertainty of landslide age spanning >6000

yr at Klickitat Lake and >8000 yr at Wasson Lake. The issue of inheritance of older

carbon in landslide deposits highlights the potential for long residence times to bias

landslide age estimates based on detrital samples collected from landslide deposits. Large

or particularly resilient material that takes longer to decay may exist on Earth's surface

for decades and potentially much longer prior to landslide emplacement (Figures 9 and

10). Our data demonstrate that this is the case for detrital charcoal. The general practice

when collecting detrital organic material from a landslide deposit for radiocarbon

analysis often fails to account for factors that likely affect the calculated age. For example, the assumption that the age of detrital material in a landslide is the same as the landslide relies on several key assumptions, many of which are not always valid. Specifically, when sampling larger wood from a landslide, one must concede that the wood may be much older than the landslide, as the interior wood of a tree must predate the time of death by many years and perhaps even centuries (Gavin, 2001; Trumbore, 2000). This is particularly true if the outer rings of the tree are missing or otherwise not available for sampling, which is not always obvious at the time of sample collection (Clague, 2015). Further, if the tree died prior to landslide failure, its residence time on the landscape remains unknown (Clague, 2015; Gavin 2003). In addition, the residence time of organic material, including pine needles and cones and leaves, on hillslopes may sometimes be remarkably long, spanning centuries for wood to millennia for charcoal (Figures 9 and 10). Long residence times may be increasingly likely for materials that are buried deeper in the soil column (Trumbore, 2000). Hence, assuming no contamination of younger carbon in a landslide deposit via bioturbation, for example, landslide ages derived from $^{14}$C dating of deposits should be considered a maximum age.

The issue of residence time on the landscape becomes less relevant for dating very old landslides because the proportion of the residence time to landslide age shrinks. In addition, for landslide ages that correspond to steeper and more linear portions of the radiocarbon calibration curve (few "wiggles"), including >500 yr B.P., uncertainty will be lower. However, as landslide age decreases, the importance of residence time increases because the residence time of datable detritus may be greater than the age of the landslide. In addition, for landslides that occurred <500 yr B.P., the intense oscillation in

the radiocarbon calibration curve increases uncertainty of derived ages (Figure 2). If analyses are exclusively derived from charcoal, landslide ages appear to be significantly older, as we demonstrated at Klickitat and Wasson Lakes. Charcoal-derived ages suggest that Klickitat Lake formed up to 6300 yr ago and Wasson Lake formed up to 9100 yr ago (Figures 9 and 10), which contradicts our dendrochronology ages by millennia. Radiocarbon dating of charcoal provides the age of the wood when the fire that burned the wood occurred (Gavin, 2003, 2001; Pessenda et al., 2001; Scharer et al., 2011; Trumbore, 2000), and that charcoal can persist in the landscape for millennia.

In landslide-dammed lakes where drowned, standing snags are absent or poorly preserved, sampling buried trees in landslide deposits can be conducted to minimize systematic bias. Depending on the quality of the preserved wood, dendrochronological analysis of buried trees in landslide deposits can provide highly accurate estimates of landslide age (e.g., Bégin and Filion, 1988; Filion et al., 1991). In addition, bark should be avoided for ^{14}C dating, as it grows slowly and incorporates organic material throughout the life of the tree, often resulting in an older calculated age (Atwater, 2017, personal commun.; Gavin, 2018, personal commun.). We encountered this problem when attempting to use bark for preliminary dating of snags at Wasson and Klickitat Lakes; ^{14}C ages from bark of the standing snags in Wasson Lake produced ages ∼200 yr too old (Figure 10). While bark from Klickitat Lake provided ages that bracketed the true age of A.D. 1751, the location of the ages on the radiocarbon calibration curve provided an ambiguous date, with A.D. 1751 being only one of many possible ages (Figure 9). Given these potential complications when dating a landslide using radiocarbon, great care

should be taken to sample material that will derive the age most likely to be contemporaneous with landslide occurrence.

*7.2. Calibration of Other Landslide Dating Techniques*

Dendrochronology provides landslide ages with subannual precision, a capability currently unmatched by other dating techniques. However, dating methods such as radiocarbon, tephrochronology, landslide creep rates, and surface roughness dating are more widely used, given the limited settings in which dendrochronology is applicable (Booth et al., 2018, 2017; Cerovski-Darriau et al., 2014; Clague, 2015; LaHusen et al., 2016; Leithold et al., 2018; Schulz et al., 2012). Calibration of these methods with the landslide ages that we derived by dendrochronological means may facilitate the use and testing of these techniques, particularly in forested landscapes subject to similar geomorphic processes as the Oregon Coast Range.

Calibration of the surface roughness dating technique by dendrochronology could greatly enhance its utility, especially if a large suite of landslide ages from dendrochronology could be used to refine a surface roughness calibration curve for western Oregon (Booth et al., 2017, 2009; LaHusen et al., 2016). Surface roughness dating could then be applied to numerous landslides in western Oregon of variable size and morphology. Clarification of the frequency and magnitude of recent landslides (<1 k.y.) will improve assessments of modern landslide hazards, and dating of the oldest landslides from soil residence times or exposure ages will be useful for studies of landscape evolution in the Oregon Coast Range (e.g., Almond et al., 2007).

To preliminarily determine if surface roughness is a good indicator of landslide age in the Oregon Coast Range, we calculated the surface roughness (standard deviation

of slope) of the landslides at Klickitat and Wasson Lakes. Using a 15 m moving window, we found average surface roughness values of 4.4 at Klickitat Lake and 7.3 at Wasson Lake. These values indicate lower roughness at Klickitat Lake and higher roughness at Wasson Lake, which is consistent with the older age of Klickitat Lake. We compared these surface roughness values to the roughness-age calibration curve of LaHusen et al. (2016) and found that the roughness of the landslide at Wasson Lake is consistent with a landslide age of A.D. 1819. The low roughness of the landslide at Klickitat Lake, however, suggests a landslide age of ~7000 yr B.P., which is much older than the calculated age of A.D. 1751. Therefore, calibration of the roughness-age curve for the Oregon Coast Range is necessary, as our data thus far are not consistent with roughness-age curves constructed in different lithologies (LaHusen et al., 2016). Further, the landslides that formed Klickitat and Wasson Lakes, while large, do not exhibit the same deep-seated morphology as the landslides that often define entire hillslopes throughout the Oregon Coast Range (Cruden and Varnes, 1996; Roering et al., 2005). The Klickitat and Wasson landslides are morphologically more consistent with large flow-like failures, as their form is elongate, and they appear to have had a more fluid and longer runout (Cruden and Varnes, 1996). The scale of these landslides also complicates measurement of surface roughness, as bare earth LiDAR data resolution on heavily vegetated landslides in the Oregon Coast Range results in low point densities that potentially artificially introduce erroneous surface roughness. If surface roughness dating is to be used in the Oregon Coast Range to constrain forcing mechanisms and provide targeted sites for dendrochronology, additional work is needed to constrain how lithology and landslide style influence morphology, which provides the basis for age-roughness curves.

In addition, refiltering of LiDAR data is necessary at some sites to ensure sufficient ground coverage.

The ages that we calculated from sediment infilling at Klickitat and Wasson Lakes bracket the ages determined from dendrochronology. The volume of alluvial sediment that filled in the valleys upstream from the landslide dams is useful beyond simply corroborating the dendrochronology-derived landslide ages. Assuming prior knowledge of erosion rate and prelandslide topography, calculating landslide ages from sediment infilling could be applied rapidly to sites throughout Cascadia. Initial calculation of ages with sediment infilling may pinpoint sites suitable for targeted dendrochronological analysis, especially if searching for landscape response to a specific triggering event, such as the A.D. 1700 earthquake. However, confirmation that dams are actively trapping sediments and are not infilled is necessary. In addition, the alluvial record preserved upstream of landslide dams is an effective tool for extracting paleoclimate, biotic, and surface process records (e.g., Mackeyet al., 2011; Marshall et al., 2017; Morey et al., 2013; Richardson et al., 2018; Schachtman et al., 2019).

The complementary nature of radiocarbon, tephrochronology, creep rates, sediment infilling, and surface roughness dating methods with dendrochronology is useful because dendrochronology, while more accurate, is more time-intensive and limited to sites with standing snags. The ability of techniques such as sediment infilling and surface roughness dating to generate age estimates for large portions of the landscape in Cascadia allows for targeted dendrochronology field work and investigation of spatial patterns that may relate to seismic triggering or other forcing mechanisms.

*7.3. Improved Dating of Existing Landslide Ages*

Standing Douglas fir snags at landslide-dammed lakes not only provide high-precision ages for landslides, but they also extend existing tree-ring chronologies for the region, which can increase the temporal reach of paleoclimate studies in Cascadia and improve the probability of dating older landslides. While using dendrochronology to date landslides is not applicable in locations where trees are not available, it may be a viable dating mechanism at some locations to constrain the age of landslides. For example, Leithold et al. (2018) provided a single radiocarbon age for a subaerial landslide in the Olympic Mountains, Washington, and posited that it may have been connected to the A.D. 1700 Cascadia earthquake. For their radiocarbon analysis, they collected wood from the outermost ring of a snag found in a terrace deposit adjacent to the landslide. For sites such as these, it may be possible to cross-date the tree-ring time series from the snag and neighboring snags with existing chronologies in the region to better constrain the age of that landslide (Leithold, 2018, personal commun.). Similarly, other large landslides with established ages in the Oregon Coast Range may have heretofore unidentified standing snags that may help either to constrain the age of the landslide, or, if too old for cross-dating with existing chronologies, to provide important data on paleoclimate in the region. As more landslides, specifically in a single region, are dated with precise dendrochronological methods, existing tree-ring chronologies will continue to be extended, improving the possibility of dating even older landslides and the forcing mechanisms that triggered them.

## 8. Conclusions

We exploited the ubiquitous signature of deep-seated landslides in the Oregon Coast Range to assess the ability of landslide dating techniques, including dendrochronology and $^{14}$C, to produce precise landslide ages that link landslide emplacement with seismic or hydrologic triggering events. Using "ghost forests" at landslide-dammed lakes in the Oregon Coast Range, we calculated subannually precise landslide ages including the winter of A.D. 1751–1752 and the winter of A.D. 1819–1820 at Klickitat and Wasson Lakes, respectively. Even though we have yet to link the A.D. 1700 earthquake with specific landslides, the precise ages that we derived for landslides in the Oregon Coast Range allow for in-depth investigation of slope-triggering mechanisms, including severe climatic forcing mechanisms as well as earthquake-triggered landslide initiation followed by delayed catastrophic failure. In addition, development of extended tree-ring chronologies from standing snags at landslide-dammed lakes, in conjunction with existing chronologies in western Oregon, will provide key constraints on the regional climate in Cascadia throughout the last 600 or more years.

While dendrochronology provides high, often subannual, precision dating of landslides, ghost forests are not common features. We have demonstrated that the variance of ages for detrital $^{14}$C dating of landslides can be large, up to 6000 yr at Klickitat Lake and almost 9000 yr at Wasson Lake; however, cautious and redundant sampling of landslide detritus for $^{14}$C analysis will increase the probability of obtaining a representative age. In addition, sediment infilling calculations of landslide age are useful for pinpointing sites for future targeted dendrochronological studies, as our results from sediment infilling rates bracket dendrochronology-derived landslide ages. Hence,

traditional methods, such as $^{14}$C dating, sediment infill dating, and surface roughness dating, are key tools for determining landslide ages. Calibration of these methods using dendrochronology will promote more accurate ages, particularly in regions that are subject to similar surface processes as the Oregon Coast Range. These enhanced dating techniques may then be used to construct a landslide age database for western Oregon, which will allow for testing of both seismic and climatic triggering mechanisms on slope stability in Cascadia.

## 9. Bridge

In Chapter II, I utilized dendrochronology and $^{14}$C dating to establish with seasonal accuracy the timing of bedrock landsliding in the Oregon Coast Range. Specifically, Klickitat and Wasson Lakes formed in the winters of 1750-1751 and 1819-1820 AD, respectively. I additionally demonstrated that $^{14}$C dating alone cannot provide the accuracy necessary to link landslide timing with a particular triggering event. $^{14}$C dating of detrital organics from the landslide deposits at Klickitat and Wasson Lakes predicted landslide ages many thousands-of-years too old. While constraining the timing of these two landslide-dammed lakes is useful for establishing an effective dating technique, it does not fully clarify the distribution of landslide ages in the Oregon Coast Range. In Chapter III, I build on this dendrochronological technique to date 20 landslides in the Oregon Coast Range, more closely consider potential landslide triggering mechanisms, and geomorphometric characteristics that dictate landslide dam preservation.

# ATMOSPHERIC RIVERS TRIGGER AND LARGE WOODY DEBRIS PRESERVES ABUNDANT LANDSLIDE DAMS IN WESTERN OREGON

Reproduced with permission from Struble, W.T., Roering, J.J., Black, B., Burns, W., Calhoun, Wetherell, L, (in review). Atmospheric Rivers Trigger and Large Woody Debris Preserves Abundant Landslide Dams in Western Oregon. *Journal of Geophysical Research: Earth Surface*.

## 1. Introduction

In regions of high relief, landsliding is a dominant geomorphic process that dictates landscape response to tectonically driven uplift (Hovius et al., 1997; Korup et al., 2007; Li et al., 2014; Montgomery & Brandon, 2002). Over short timescales (10–$10^3$ yr), landslides contribute significant volumes of sediment to river networks (Finnegan et al., 2019; Li et al., 2016; Roering et al., 2015) and represent a significant societal hazard (e.g. Burns et al., 2017; Fan et al., 2019; Swanson et al., 1986). Furthermore, landslides that impound valleys and form lakes and/or become sediment-filled serve as secondary drivers of landscape evolution, potentially over long timescales (>$10^4$ yr; e.g. Korup, 2004; Korup et al., 2006). Landslide dams locally store immense quantities of sediment that cover and armor bedrock channels (e.g. Hewitt, 1998; Korup et al., 2004; Lancaster & Grant, 2006), and upstream low-gradient valley reaches foster ecological diversity and sequester organic carbon (Beeson et al., 2018; Bilby & Likens, 1980; Mackey et al., 2011; May et al., 2013). As a cascading hazard, when landslide dams become unstable, they often release large outburst floods (Costa & Schuster, 1988; Fan et al., 2019; Shang et al., 2003), making characterization of the timing and persistence of landslide dams

critical for hazard mitigation. As such, well-dated landslide dam inventories coupled with robust geomorphometry provide clear linkages between landslide triggering mechanisms and landscape characteristics that promote landslide dam preservation.

Landslide dams result from both earthquakes and hydrologic events (e.g. Fan et al., 2020 and references therein; Massey et al., 2018). The 2016 $M_w$ 7.8 Kaikōura earthquake on the South Island of New Zealand triggered >10,000 landslides, many of which dammed rivers and then breached following heavy rains, releasing large floods (Massey et al., 2018). Similarly, landslide dams were recorded during the 2008 Wenchuan earthquake, and several of these landslide dams have reactivated several times since coseismic dam emplacement (Fan et al., 2018). While often considered a coseismic process, landslide dam formation is also triggered by major hydrologic events such as heavy rainfall and rapid snowmelt (e.g. Costa & Schuster, 1988; Swanson et al., 1986; Wu et al., 2014)

Landslide dams typically have a relatively predictable level of stability based on geomorphometric values such as landslide volume, upstream drainage area, impounded lake volume, dam height, and relief (e.g. Fan et al., 2020; Korup, 2004). In New Zealand, Korup (2004) observed that large dams that impound high-volume lakes tend to be the most stable and persistent in the landscape. In contrast, small dams, particularly those with a large upstream drainage area, tend to be unstable and least likely to persist in the landscape and impound upstream lakes for a significant length of time (Korup, 2004). Specifically, Korup (2004) formulated the Impoundment Index, $I_b$, among other stability metrics, as the relative magnitude of landslide dam volume to upstream drainage area, expressed as

$$I_b = log \ (V_D A_C^{-1}), \qquad\qquad (1)$$

where $V_D$ is the landslide dam volume and $A_C$ is upstream drainage area. He observed that

New Zealand dams where $I_b > 7$ were very stable and long-lived, and dams where $I_b < 4$

were unstable, though he recognized that this threshold varies widely between landscapes

(Korup, 2004). For instance, Fan et al. (2020) noted using a global landslide dam

compilation that impoundments where $I_b < 5$ are often unstable. In addition, while Korup

(2004) observed that tall landslide dams may be more stable for a given upstream relief

(difference in elevation between highest point in catchment and elevation at dam), he

noted considerable scatter existed in the data and that different thresholds would exist for

different landscapes. As such, other factors contribute to landslide dam longevity,

particularly lithology and landslide style (i.e. volcanic debris avalanches, debris flows,

translational and rotational deep-seated failures, etc.), dam height, climate, valley width,

and the influence of vegetation (e.g. Dal Sasso et al., 2014; Fan et al., 2020, and

references therein; Tacconi Stefanelli et al., 2016). Although multiple metrics exist for

quantifying the stability of landslide dams, interpreting the tradeoffs and interactions of

these controlling factors and accurately transferring these relationships to diverse

landscapes to predict long-term dam stability remains an acute challenge.

The Cascadia Subduction Zone (CSZ) region exhibits myriad slope failures,

including many landslide dams (Figure 1). The relative importance of different triggering

mechanisms for instigating these slope failures remains unclear. Shaking during great

(M>8.0) CSZ earthquakes is expected to be high, potentially producing peak ground

accelerations up to 0.6g in the western forearc (Frankel et al., 2018; Madin & Burns,

2013; Wirth et al., 2018). Such shaking would suggest triggering of over 50,000 bedrock

slope failures (Keefer, 1984; Marc et al., 2016). However, the distribution and intensity of landsliding during CSZ earthquakes has remained unclear, in part due to the relative dearth of landslides during observed subduction zone earthquakes elsewhere compared to shallow crustal earthquakes (e.g. Serey et al., 2019; Wartman et al., 2013). In addition, a lack of age constraints on mapped prehistoric landslides throughout Cascadia have complicated efforts to explicitly link slope failures with seismic or hydrologic triggers. In Cascadia and other convergent margins, it has been suggested that hydrologically triggered bedrock landslides may be more common than those triggered by earthquakes, and those that do occur as a result of earthquakes are often overprinted by hydrologically induced failures and landslide reactivations, thus complicating efforts to accurately parse relevant bedrock landslide triggering mechanisms (LaHusen et al., 2020; Marc et al., 2019). Landslide-dammed lakes, however, are uniquely well-suited to record an individual landslide event, even if the damming landslide undergoes several episodes of movement (Struble et al, 2020). As such, an increased number of dated landslide dams coupled with known triggering events will vastly improve slope failure models for the Cascadia forearc, clarify the relative importance of hydrologic and seismic triggers, and inform analyses of dam preservation and downstream impacts.

---

**Figure 1** (next page). **Landslide dams in the Oregon Coast Range**. Black dots are mapped landslide dams and white squares are dated landslide dams. Dams with numeric labels are those we date in this study and are numbered according to Table 1. Dams with text labels are dams with existing age control. Black box corresponds to border of Figure 2. Impounded valleys with existing age control are: A: Ayers Lake (1975 AD; Thrall et al., 1980), G: Gould Lake (1894 AD; Zybach, 2003), K: Klickitat Lake (winter 1751/52 AD; Struble et al., 2020), L: Loon Lake (~1460 yr B.P.; Baldwin, 1958), S: Sitkum (>3000 yr B.P.; LaHusen et al., 2020; Lane, 1987), T: Triangle Lake (>42,000 yr B.P.; Worona & Whitlock, 1995), W: Wasson Lake (winter 1819/20 AD; Struble et al. (2020)).
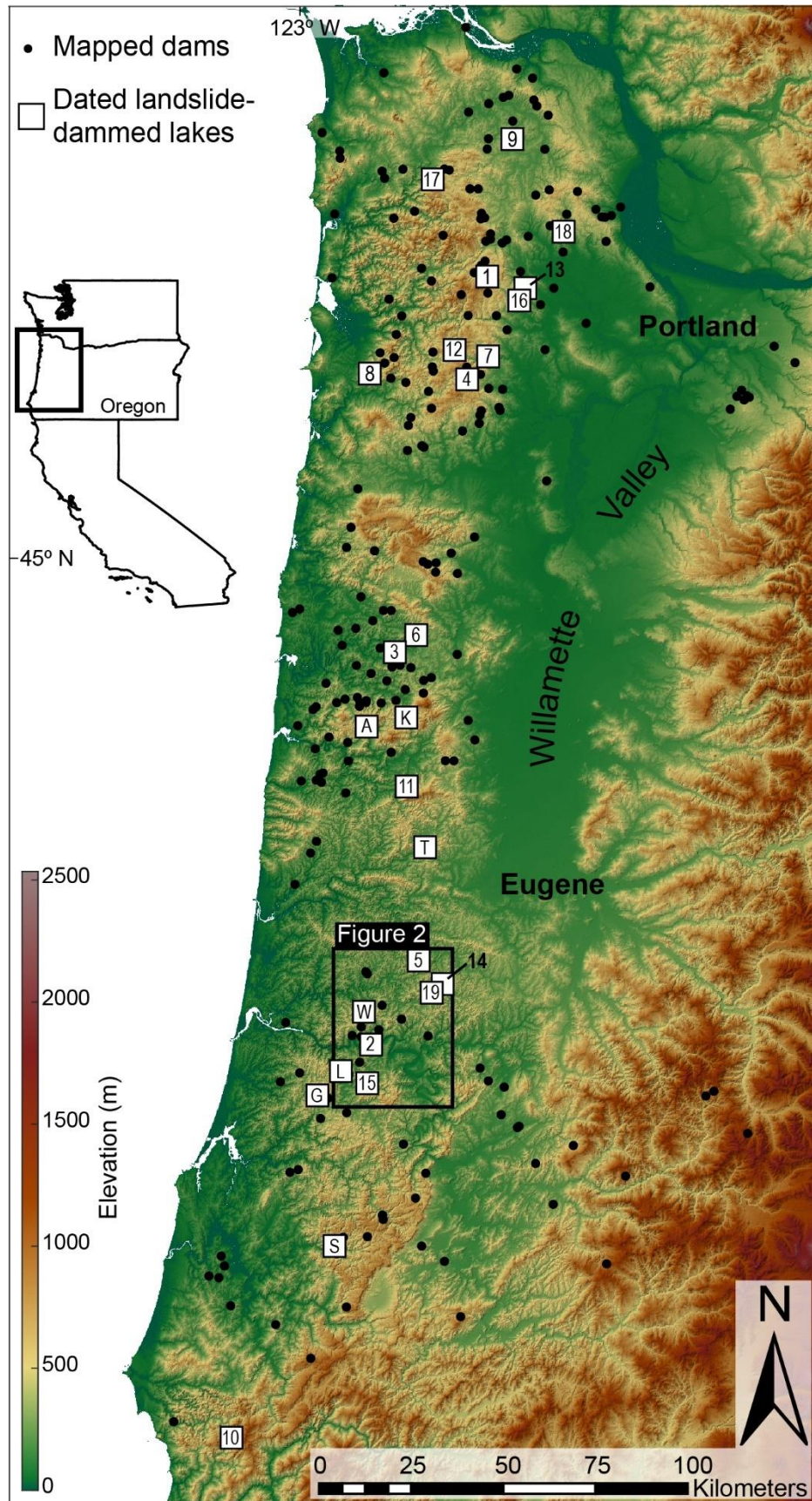
Here, we utilize drowned Douglas Fir trees, or 'ghost forests,' at landslide-dammed lakes to establish age control for 20 landslide-dammed lakes in the Oregon Coast Range to clarify the contributions of seismic ground motion and extreme precipitation triggers, notably atmospheric rivers, to bedrock landslide dam formation in Cascadia. In addition, these new landslide ages inform topographic analyses to pinpoint characteristic locations in the Oregon Coast Range where landslide dams are most likely to persist. We specifically consider the role of upstream drainage area and valley width as well as the presence of woody debris in dictating the stability and longevity of landslide dams.

## 2. Study Area

### 2.1. Geologic setting

Landslides are ubiquitous throughout the Oregon Coast Range (OCR), a swath of unglaciated topography that parallels the CSZ for >300 km from the Klamath Mountains to the Columbia River (Figures 1 and 2). The OCR is primarily underlain by Eocene accreted volcanic terranes and marine siltstone and sandstone facies, notably the Tyee Formation in the central and southern OCR (Heller & Dickinson, 1985; Wells et al., 2014). In the central to northern OCR, the Tyee Formation transitions to similar Eocene-Oligocene marine sedimentary rocks, overlain by Miocene Columbia River Basalts in northern OCR catchments (Walker & MacLeod, 1991). The OCR is widely recognized for regions of characteristically uniform topography, where incision is dominated by debris flows (Penserini et al., 2017; Stock & Dietrich, 2003), and the range has often been suggested to approximate a balance between uplift and erosion (Montgomery, 2001; Reneau & Dietrich, 1991), with uplift and erosion rates of ~0.05-0.3 mm yr$^{-1}$ and ~0.05-

0.14 mm yr$^{-1}$, respectively (e.g. Balco et al., 2013; Kelsey et al., 1996; Penserini et al., 2017). Much of the topography of the OCR, however, is locally defined by hummocky, low-relief hillslopes that demarcate deep-seated, bedrock landslides. This conspicuous topographic imprint is prevalent on dip slopes and becomes increasingly prominent moving from south to north, corresponding to a higher siltstone-to-sandstone ratio in Tyee Formation turbidite sequences (Roering et al., 2005). In addition, ridge capping volcanic units resting on marine sedimentary rocks in the northernmost OCR, correspond with significant bedrock slope instabilities (Theule, 2008).

*2.2. Landslides*

Landslides take many forms in the OCR. Shallow, colluvial landslides that mobilize into debris flows are ubiquitous in the OCR during the rainy season, when increased pore pressures from heavy rainfall result in abrupt failure of colluvial hollows (e.g. Montgomery et al., 2000; Schmidt et al., 2001; Stock & Dietrich, 2003). Debris flows often travel for several kilometers, and thousands of such failures have been observed during major storms in western Oregon (e.g. May, 2002; Schmidt et al., 2001; Wiley, 2000). These debris flows, which can generate local and ephemeral sediment impoundments that temporally retain sediment and wood and occasionally form small, temporary lakes (e.g. Lancaster & Casebeer, 2007; Lancaster & Grant, 2006; Petersen, 1948), do not tend to form persistent landslide-dammed lakes. In contrast to the observed pervasiveness of shallow landslides and debris flows, deep-seated, bedrock landslides that fail catastrophically are conspicuously rare, though not completely absent, during historic (<200 ybp) rain events (Orr & Orr, 1999; Roering et al., 2005). The morphologic pervasiveness of deep-seated, bedrock slope failures in the OCR – >20,000 have been

53

mapped to date (Franczyk et al., 2019; LaHusen et al., 2020) – coupled with observations of >200 landslide dams that we observe here, however, would seem to suggest that deep-seated slides occur with some regularity and/or persist in the landscape for extensive periods. In an effort to clarify the discrepancy that few bedrock landslides in the OCR have failed catastrophically in the past few hundred years but abound in the landscape, earthquake ground motion from the CSZ and shallow crustal faults has commonly been invoked to explain the distribution of deep-seated landslides in the Cascadia forearc (e.g. Leithold et al., 2018; Morey et al., 2013; Pierson et al., 2016; Richardson et al., 2018; Roering et al., 2005; Schulz et al., 2012; Schuster et al., 1992). However, no landslide has been definitively linked with ground motion from the last great earthquake, which occurred on January 26, 1700 AD (Atwater et al., 2005; Yamaguchi et al., 1997).

Prior to this study, only two stable landslide-dammed lakes, Gould and Ayers Lakes, were historically observed and documented (Thrall et al., 1980; Zybach, 2003). Most landslide dams in the OCR are formed by deep-seated bedrock translational or rotational landslides, though some have the appearance of being large deep-seated flow-like slides, such as those that formed Wasson and Klickitat Lakes (Lane, 1987; Struble et al., 2020). Importantly, unlike the shallow colluvial failures that mobilize into debris flows that are much more prolific in the OCR, the slides that form stable dams have deeper failure surfaces and are composed of bedrock, even if highly disaggregated, such as is commonly observed in distal facies of the Tyee Formation with a high percentage of siltstone (Lane, 1987; Roering et al., 2005).

Some of the most notable landslide dams in the OCR include Loon Lake, forming ~1460 yrs B.P. (Baldwin, 1958), Triangle and Little Lakes >40,000 yrs B.P. (Worona &
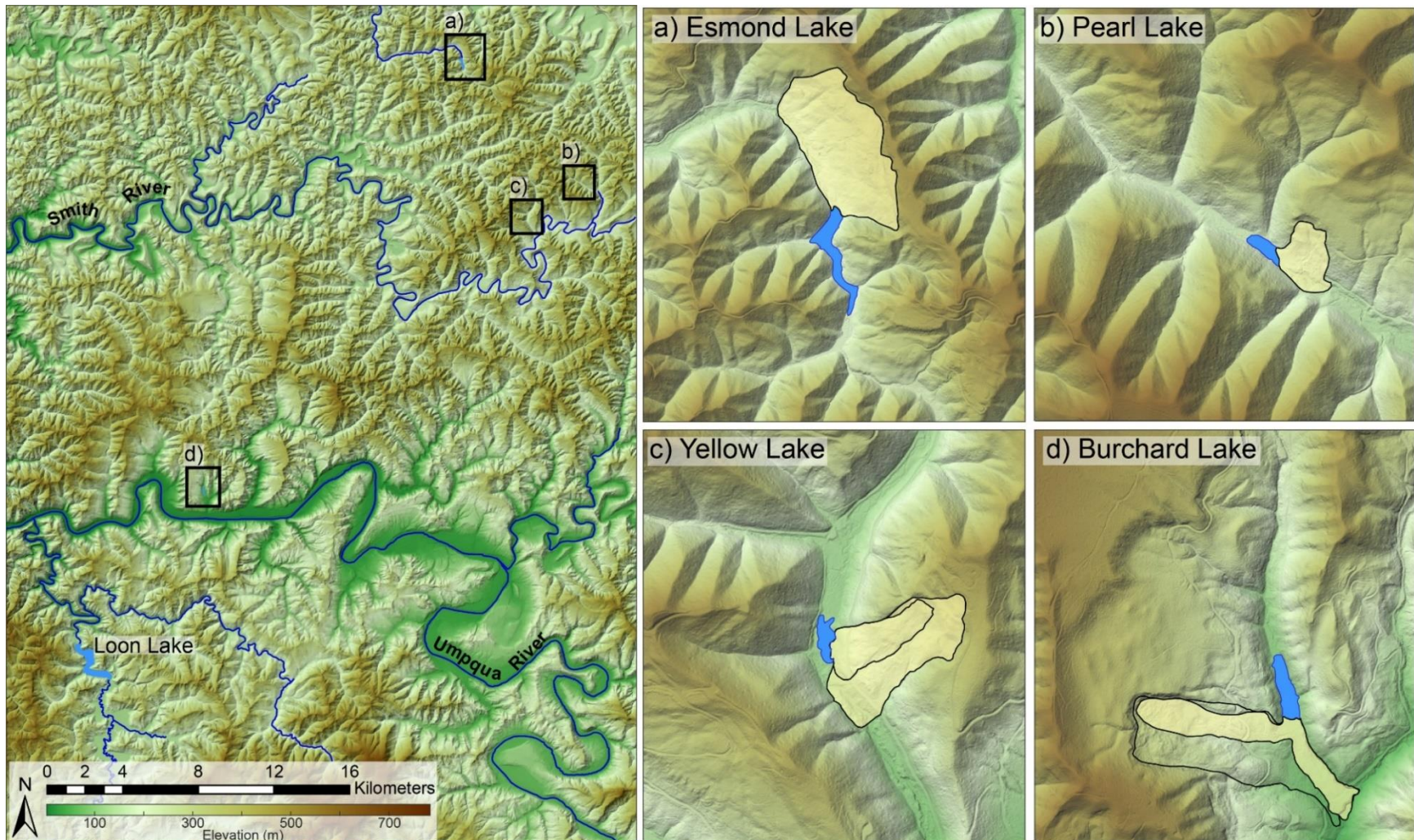
**Figure 2**. **Landslides that cluster in the winter 1889/90 AD in the central OCR**. Note location of Loon Lake in the southwest corner of the main map. Insets include a) Esmond Lake; b) Pearl Lake; c) Yellow Lake, note that there are at least two discrete failures; d) Burchard Lake, note that the damming slide is nested in a larger, older slide (outlined in black, unfilled), which is additionally nested in a much larger landslide complex.

Whitlock, 1995), and sediment-filled Sitkum Lake, estimated to have formed between 4110 yrs B.P. (LaHusen et al., 2020) and 3125 yrs B.P. (Lane, 1987). These sites have conspicuously high upstream drainage areas (Loon: 230.6 km$^2$; Triangle: 137.6 km$^2$; Sitkum: 208.2 km$^2$; Lane, 1987). Younger dated landslide-dammed lakes include Wasson and Klickitat Lakes, which formed in the winters of 1819/20 and 1751/52, respectively (Struble et al., 2020), and Ayers and Gould Lakes which were observed failures in 1975 and 1896, respectively (Thrall et al., 1980; Zybach, 2003). The relative dearth of stable landslide dams in the OCR, in contrast to the prolific number of debris flows, raises several questions: 1) What are the mechanisms that are most likely to trigger bedrock landslides that form stable dams? 2) Have factors (i.e. vegetation, climate, geomorphology) that control the stability of landslide dams temporally changed? and 3) What are the geomorphic characteristics that dictate where landslide dams are the most stable in the OCR?

*2.3. Climate and atmospheric rivers*

The OCR is a humid landscape characterized by cool, wet winters and warm, dry summers (PRISM Climate Group, 2016). Most of the precipitation falls during the winter, a significant portion of which is supplied by atmospheric rivers (ARs), narrow and intense bands of moisture originating in the tropics of the Pacific Ocean that are driven onto the Pacific coast of North America. ARs provide moisture that is vital for ecosystem and societal health and are responsible for 20-50 percent of the precipitation along the Pacific coast of North America (Dettinger et al., 2018 and references therein), though they are also responsible for the vast majority of intense rainfall events that trigger landslides and floods (Neiman et al., 2008; Ralph et al., 2006). Sequences of the

most extreme ARs, which individually last approximately one to two days, provide high-intensity, long-duration rainfall that leads to record and generation-defining floods (Ralph et al., 2006 and references therein; Rantz, 1959). While AR intensity is variable and can vary dramatically within individual storms (Ralph et al., 2019), AR orientation relative to topography additionally affects precipitation totals (Dettinger et al., 2018), which complicates prediction of landscape impacts such as landsliding. In addition, runoff and flooding can be highly augmented when warm and heavy AR rainfall events melt snow (e.g. Neiman et al., 2008). For instance, cold temperatures and heavy snow followed by a series of AR events in January and February of 1996 caused major flooding in western Oregon and triggered tens of thousands of shallow landslides that mobilized into debris flows (Schmidt et al., 2001; Wiley, 2000). A similar sequence of heavy snow followed by several ARs caused major flooding in western Oregon in 1964, 1890, and 1861/62, among others (Harr, 1981). In short, high-intensity winter storms on the Pacific coast, including western Oregon, are demonstrably AR-driven and are responsible for the lion's share, potentially up to 90 percent, of rain-triggered slope failures and debris flows (Chen et al., 2018; Harr, 1981; Oakley et al., 2018; Ogle, et al., 2018; Ralph et al., 2006).

*2.4. Dating landslide dams*

In attempts to link OCR bedrock slope failures with known triggering mechanisms, most prior landslide dating has relied on $^{14}$C dating of organic material collected from landslide deposits. In addition, surface (topographic) roughness dating of landslides, where rougher (smoother) landslide deposits are younger (older), has been used to map and construct landslide age databases (Booth et al., 2017, 2009; LaHusen et al., 2016, 2020). In the OCR, in particular, calibrated surface roughness dating of

landslide deposits does not reveal a significant abundance of landslide ages

corresponding to 1700 AD or previous Cascadia subduction earthquakes, suggesting that

precipitation is the primary driver of Cascadia forearc deep-seated slope instability

(LaHusen et al., 2020). However, to explicitly link potential bedrock landslide triggering

mechanisms with the timing of individual slope failures, landslide ages must be

determined with annual to sub-annual accuracy. Although $^{14}$C and topographic roughness

dating techniques provide landslide ages that allow for construction of large landslide age

databases (e.g. Benda, 1990; Booth et al., 2017; Clague, 2015; LaHusen et al., 2016,

2020; Lang et al., 1999), these approaches lack sufficient accuracy to rigorously test

potential event-based triggering. When used in isolation, $^{14}$C dating, for example, has the

complication of contamination by recalcitrant carbon, especially charcoal, which can

persist in the landscape for millennia and provide potentially much older sample ages

than are representative (Gavin, 2001; Scharer et al., 2011; Streig et al., 2020; Struble et

al., 2020; Trumbore, 2000). In addition, $^{14}$C dating cannot by itself differentiate between

initial slope failures that entrained organic material and later landslide reactivations

(Gavin, 2001; Struble et al., 2020; this study). We note, however, that Bayesian

constraint of $^{14}$C ages using 'wiggle matching,' which utilizes either tree rings or

stratigraphy to constrain the sample age probability density function, is an enhanced $^{14}$C

dating technique that can provide comparatively robust ages (e.g. Bronk Ramsey, 2009;

Hogg et al., 2019; Scharer et al., 2011; Streig et al., 2020; Struble et al., 2020). When

possible, dendrochronology, or tree ring analysis, provides the only known tool to

explicitly link the timing of slope failure with individual triggering events (e.g. Pringle,

2014; Šilhán, 2020; Struble et al., 2020). Although this approach is limited by the

timescale of existing tree ring records, the Pacific Northwest is well-suited due to the longevity of trees and their relative abundance in the landscape.

Dendrochronology, particularly of 'ghost forests,' has been applied successfully in Cascadia to date earthquakes and landslides. 'Ghost forests' along the Cascadia coast famously constrained the timing of the last CSZ earthquake to the winter of 1699/1700 AD (written records of the tsunami striking Japan narrowed the timing further to ~9 p.m. (local time) on January 26, 1700; Atwater et al., 2005; Yamaguchi et al., 1997). Similarly, 'ghost forests' are common at numerous landslide-dammed lakes and marshes in the OCR, where still-standing trees drowned as water rose behind the landslide dam (Figure 3). Struble et al. (2020) dated landslide dams in the OCR with subannual accuracy by coupling dendrochronology and $^{14}$C dating at Klickitat and Wasson Lakes to determine that they formed in the winters of 1751/52 and 1819/20 AD, respectively.

**3. Methods**

Improved landslide dating techniques, including dendrochronology, present the opportunity to construct improved landslide-age databases for the OCR, which will clarify potential linkages between landslide timing and seismic or hydrologic triggers. We, therefore, follow a similar technique to Struble et al. (2020), by using dendrochronology and $^{14}$C 'wiggle matching' to estimate the age of 20 landslide-dammed lakes in the OCR. The improved landslide ages we calculate here coupled with the widespread topographic signal of bedrock landsliding in the OCR spurs continued investigation of recent slope failures and calibration of dating techniques that parse landslide triggering mechanisms. In addition, consideration of geomorphometric values such as upstream drainage area, valley width, and the presence of large woody debris

59

**Figure 3.  Standing snags at landslide-dammed lakes**. a) Burchard Lake, formed winter 1889/90 AD. b) Esmond Lake, formed winter 1889/90 AD. c) Klickitat Lake, formed winter 1751/52 AD (Struble et al., 2020).

clarify characteristic locations in the landscape where triggered landslide dams are most likely to persist and remain stable in the OCR. Restriction of geomorphometric analysis to dated landslides will allow for parsing of how earthquake and hydrologic triggers affect landslide dam emplacement behavior in the OCR.

*3.1. Dendrochronology and $^{14}C$ wiggle matching*

We recorded >200 landslide-dammed lakes in the OCR using high-resolution (1-m) airborne lidar digital elevation models (DEMs). We selected a smaller subset for dating, preferentially pinpointing sites that are likely young enough to be datable with dendrochronology, such that the drowned tree ring sequence overlaps with existing tree ring records (up to ~800 years in western Oregon), and potentially coincide with the 1700 AD earthquake. More specifically, sites were selected if they: 1) appear to be recent failures (hundreds of years), defined by the presence of sharp scarps and minimal channel incision on the deposit surface (Booth et al., 2017, 2009; Burns & Madin, 2009; LaHusen et al., 2016); 2) appear to be the result of a single damming event; and 3) appear in aerial imagery to have standing, drowned trees. The degree of preservation of standing snags and ease of access, defined by land ownership, delta progradation, and marginal sedimentation, further refined the list of sites to be dated (Table 1; Figure 1).

Standing snags at each landslide-dammed lake are primarily Douglas Fir (*Pseudotsuga menziesii*), the predominant tree species throughout the OCR, though at some sites the best-preserved snags are western red cedar (*Thuja plicata*). From each standing snag, we extracted slabs of sufficient width to account for ring width variability around the tree (~20-30 cm; Figure 4A-B), being careful to limit visual impact at the site. We dried, sanded, and polished the slabs, finishing with 15 μm lapping film. We visually crossdated samples within each site, beginning with trees for which bark was still attached and expanding to trees in which outermost increments were not preserved. We then scanned the slabs and measured total ring widths on at least two separate transects to accommodate ring width variation around the tree using the dendrochronology software
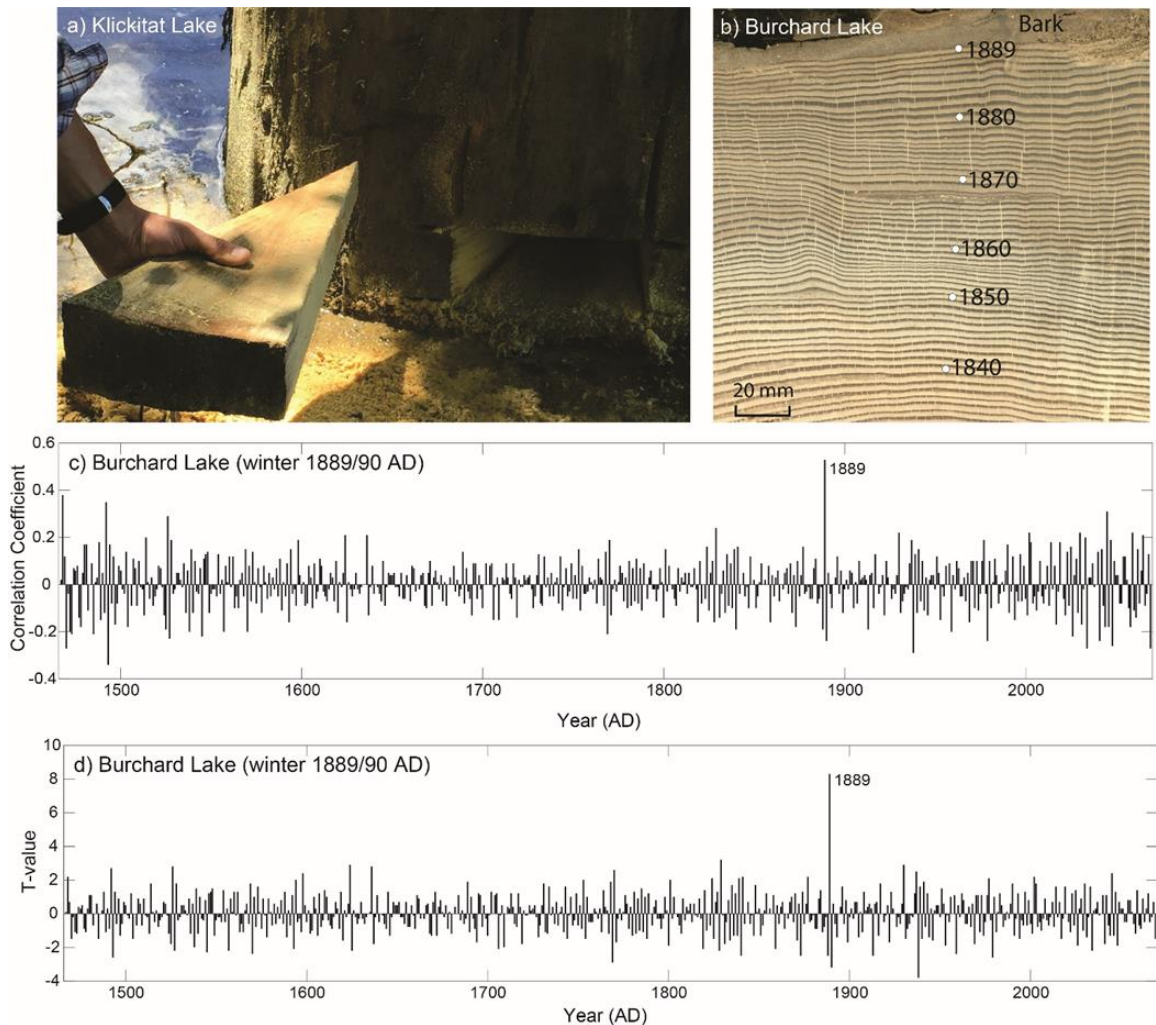
**Figure 4**. **Extracted slabs, ring measurements, and dating**. a) Example of extracted slab, in this case from Klickitat Lake. b) Slab from Burchard Lake dated to the winter of 1889/90. The death ring is labeled as 1889, and the preceding five decades also labeled. Note that bark is still attached in this case. c) Correlation coefficients of Burchard Lake ring measurements lagged against Marys Peak chronology. Note that the conspicuously high correlation coefficient corresponds to the year 1889. d) T-values for same ring series as in (c). T-values take into account the amount of overlap between dead-collected rings and the live tree chronology for each lag. Thus, samples with a high correlation and significant overlap with the live tree chronology produce high T-values. Again, note 1889 as the final growth increment. See Table 1 for T-values from each site.

CooRecorder (Larsson, 2013). Dating within the site was further corroborated by extracting the high-frequency, interannual component of growth variability using the "heavy detrend" option and visually comparing these patterns among measurement time series in the program CDendro (Larsson, 2013). For each site, we began by comparing

62

time series within trees followed by comparisons among trees. Finally, crossdating was statistically checked within each site using the program Cofecha (Holmes, 1983). First, each measurement time series was fit with a highly flexible cubic spline with a 50% frequency-cutoff of 32 years after which measurements were divide by those predicted by the spline. This removed low-frequency variability and long-term trends, isolating the interannual, high-frequency component of growth that is unique to climate variability and meets assumptions of correlation analysis. Any remaining autocorrelation was removed using low-order autoregressive functions to ensure serial independence. Then the high-frequency component of each measurement time series was correlated to the mean of all others. If a dating error had occurred, it would have frameshifted the growth pattern in time and caused a conspicuously low correlation. The wood for any samples with low correlations was visually re-inspected and measurements corrected if an error was confirmed.

The high-frequency component of growth was averaged across all measurement time series within a site and then compared against the high-frequency component of growth in existing, absolutely dated tree ring chronologies for western Oregon, primarily from Marys Peak in the OCR (44.504° N, -123.553° W) and sites in the western Cascade Range (Black et al., 2015). To compare each pair of chronologies, we calculated for all possible lags with at least 30 years overlap both Pearson correlation coefficients and "T scores," where

$$T\ score = c\sqrt{\frac{n-2}{1-c^2}},\tag{2}$$

and *c* is the correlation coefficient, and *n* is the number of overlapping years (Larsson, 2013). Thus, for a given correlation coefficient, the T-score decreases as overlap between

the two chronologies decreases (Figure 4). This provides a more stable metric of covariability than correlation coefficients, which are prone to spuriously high values when degrees of freedom are low. The date of the outermost increment formed under the bark indicates the year of lake formation, and the extent of increment formation (earlywood only, latewood fully formed, etc.) provides evidence as to the season of tree death. For sites where bark is not present and there is evidence of decay in the outermost growth increment(s), landslides must have occurred more recently than the calculated date. Although subjective, we considered dating confidence "high" if overlap with the absolutely dated chronology was >150 yrs, the T-score was approximately 6 or greater, and the T-score was very conspicuously greater than all other lags. Spurious dates are very unlikely under these circumstances. We considered dating confidence "moderate" if the T-score was very conspicuously greater than all other lags, but less than six based on overlap less than 150 years. Finally, we considered dating confidence "poor" if the T-score was not conspicuously greater than all other lags.

For landslides that did not cross correlate with existing live tree chronologies or measurement time series from landslide-dammed lakes, and for independent corroboration of the dendrochronological dating at a subset of dated lakes, we collected wood from rings spaced ~40 years apart or more in extracted slabs for [14]C 'wiggle matching.' We used the Bayesian statistical tool OxCal to convert ^{14}C years to calendar years and constrain the output probability density functions for calendar age using the known number of rings that separated each sample (i.e. 'wiggle matching;' Bronk Ramsey, 1995). We additionally ^{14}C wiggle matched a branch and log found in the Burchard and Yellow Lakes landslide deposits, respectively.

*3.2. Landslide dam geomorphometry*

In accordance with criteria often used to quantify landslide dam stability and to determine the preservation potential of landslide dams in western Oregon, we measured geomorphometric values such as upstream drainage area, valley width, local relief, and landslide size (e.g. Fan et al., 2020, and references therein) at each dated landslide dam. We used 30-m Shuttle Radar Topography Mission (SRTM) DEMs to calculate upstream drainage area at all >200 mapped landslide dams. To determine if landslide dams tend to persist at characteristic locations in the landscape, we also calculated upstream drainage area for all nodes in the drainage network in western Oregon. We plotted normalized histograms of upstream drainage area for both the landslide dam dataset and the mapped stream network. We note that due to the size of the full landslide dam dataset, which precludes adequate field analysis of all sites, including whether or not the dams still impound lakes or sediment-filled valleys, we limit the consideration of geomorphic metrics such as mean local relief (100-meter window on 30-m SRTM), valley width, and landslide size to dated landslide dams only, where we have observed in the field that these dams actively impound lakes or marshes.

We used 1-m lidar DEMs to record landslide deposit surface area, landslide failure depth, slope angle of the failed surface, and landslide type at the 20 dated sites where lidar data exist (no lidar at Laird Lake; Table S1; Burns & Madin, 2009), as well as at previously dated OCR landslide dams including Klickitat (winter 1751/52), Wasson (winter 1819/20), Gould (1894), and Ayers (1975) Lakes (Thrall et al., 1980; Struble et al., 2020; Zybach, 2003).

To isolate whether topographic relief dictates the size of landslide dams that remain stable and persist in the landscape, we explored the potential relationship between mean local relief and landslide surface area. In addition, to determine if landslide dams emplaced at high drainage areas need to be larger in order to remain stable, we plot landslide dam volume as a function of upstream drainage area, and we calculate the Impoundment Index, $I_b$, defined in Equation 1 by Korup (2004). The impoundment index quantifies the relationship between landslide size and upstream drainage area such that for a given drainage area, larger landslides are more stable. Previous landslide dam compilations have observed that landslide dams are typically stable when $I_b>5$ (e.g. Fan et al., 2020; Korup, 2004). To include landslide volume in the calculation of $I_b$, we calculated the volume of each landslide using the power-law scaling between landslide surface area and volume defined by Larsen et al. (2010).

Finally, we considered the role of valley width on controlling landslide dam preservation, with the expectation that dams are more likely to remain stable at smaller valley widths. We measured valley width downstream from each landslide dam to ensure that the aggraded valleys upstream from each deposit did not systematically produce overestimated valley widths (May et al., 2013). Width was measured as the distance from the slope break at the base of bedrock or soil mantled hillslopes on each side of the valley and plotted in a histogram with a bin size of 10 meters.

**4. Results**

*4.1. Landslide dam ages*

Crossdating was strong within each of the lake sites except Sunago Lake, in which tree lifespan was too short (<50 yr) for dating, and Spruce Run, in which samples

could not be dated with one another. Otherwise, the correlation between each measurement time series and the average of all others (e.g. the interseries correlation as reported by Cofecha) ranged from 0.57 to 0.85 (Table 1). In almost all cases, the tree species was Douglas Fir with the exception of Yellow Lake, in which only red cedar samples were available, and also Pearl Lake in which red cedar and Douglas Fir were both available and could be crossdated (Table 1). Replication was low within each lake generally ranging from two to four trees, though tree lifespan was sufficient to generally allow >150 yrs overlap with other sites (Table 1).

The strength of dating varies among sites with ten meeting the criteria for "high" confidence, four meeting the criteria for "moderate" confidence, and two meeting the criteria for "poor" (Figure 5). The first of the "poor" confidence lakes is Scoggins Valley for which the T-score is not exceptional relative to other lags, and the period of overlap is low at only 67 years (Table 1). The date of 1875 assigned to the outermost ring must be interpreted with caution. The other "poor" confidence site is Hemlock Lake in which the highest T-score against the mean of all other lakes corresponds to 1715 AD while the highest T-score against Marys Peak corresponds to 1866 AD. Both T-scores are low at 4.0 and 4.5 and do not stand out against the distribution of other T-scores (Table 1). Given these weak, inconsistent relationships and low overlap of only 89 years, we do not have confidence in a Hemlock date, though $^{14}$C 'wiggle matching' suggests the landslide dam may have been emplaced after 1896-1910 AD (Figure 5).

Our collected landslide ages record persistent deep-seated, bedrock landslide damming activity throughout the OCR in the past few centuries (Figure 5). Samples that were sufficiently long-lived to have suitable overlap but did not date to regional
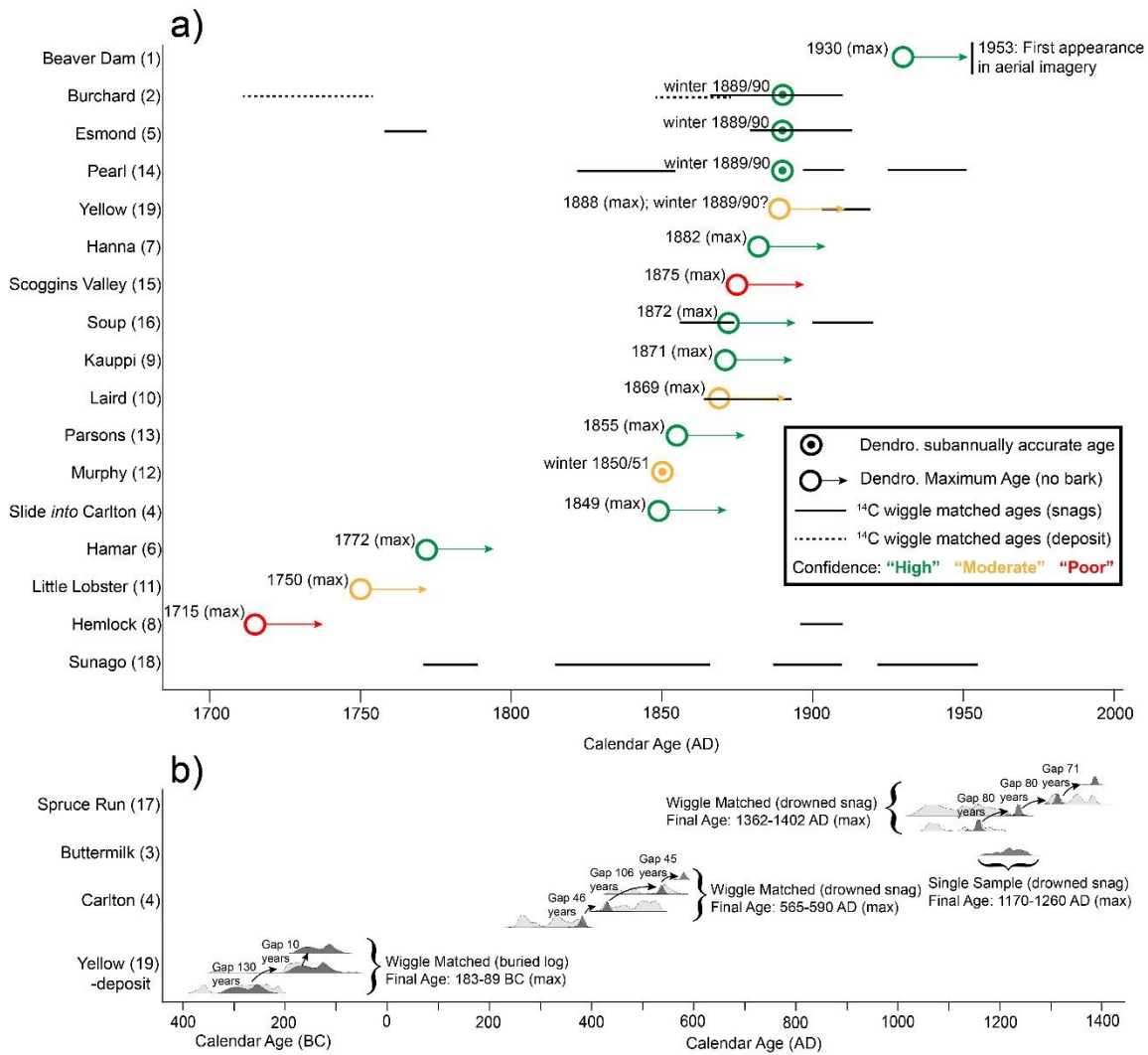
**Figure 5. Landslide dam ages in the OCR**. a) Landslides that postdate the 1700 AD earthquake. Bull eye symbols are landslides where the timing of formation has been determined to the season. Note cluster of landslides in the winter of 1889/90, potentially corresponding to major flooding in February 1890. Open circles are sites dated with dendrochronology, but where a lack of bark precludes annual accuracy. These are maximum ages. Black solid lines are wiggle matched ^{14}C samples from standing snags at select sites. Dashed line is wiggle matched ^{14}C from a branch buried in the deposit at Burchard Lake. Note that there was no clear age from dendrochronology at Sunago Lake, so only a ^{14}C wiggle matched age is plotted. Green ages are those where dating confidence is "high," orange is "moderate" confidence, and red is "poor" confidence (see text for explanation). b) Landslides that pre-date the 1700 AD earthquake. Note that these landslides are too old to date with current tree ring chronologies. Light gray PDFs are ^{14}C ages for individual samples. Dark gray are PDFs constrained for each sample after wiggle matching. Gaps are the number of rings that separate samples in each snag. At Buttermilk Lake, only a single sample of the outer exposed rings was collected. Note that the age of a log wiggle matched from the deposit at Yellow Lake differs from the dendrochronology age at Yellow Lake in (a) by >1900 years. All uncalibrated ^{14}C ages are in Table S2.

absolutely dated chronologies died in the relatively distance past according to $^{14}$C wiggle matching. At Spruce Run, Buttermilk, and Carlton Lakes, ages from $^{14}$C 'wiggle matching' (single sample $^{14}$C age at Buttermilk Lake) show that tree death pre-dates the start of the 500 yr Marys Peak chronology at 1362-1402 AD, 1170-1260 AD, and 565-590 AD, respectively (Figure 5B; Table 1).

At four sites, the preservation of bark allowed for determination of a sub-annually accurate date using dendrochronological techniques (Figure 5). At all other sites at which dendrochronological techniques could be used to establish a date, bark was not attached and there was evidence of decomposition in the outermost rings such that the lake formed more recently than the last ring would suggest. Yet, even with the inaccuracy from decomposition of the outer rings, these results indicated that no slide was clearly associated with the 1700 AD CSZ earthquake.

Of the older lakes dated, Little Lobster and Hamar Lakes formed no earlier than 1750 and 1772 AD, respectively. All other landslides cluster in the mid- to late-1800s, with only Beaver Dam Lake forming in the twentieth century, sometime between 1930 (dendrochronology date on rotted slab) and 1953 (first appearance in aerial imagery). Due to the preservation of bark, and thus the outermost growth increments, we are able to establish landslide ages with annual accuracy at four sites, specifically, Murphy (winter 1850/51 AD), Burchard (winter 1889/90 AD), Esmond (winter 1889/90 AD), and Pearl (winter 1889/90 AD) Lakes. The remaining landslide dams for which we have established a maximum age include: a small landslide that slid *into* Carlton Lake (1849), Parsons (1855), Laird (1869), Kauppi (1871), Soup (1872), Scoggins Valley (1875), Hanna (1882), and Yellow (1888) Lakes (Figure 5, Table 1). Trees at Sunago Lake were

too short-lived to correlate with existing tree ring records, though $^{14}$C wiggle matching suggests failure sometime between 1771-1956 AD (Figure 5A).

While most $^{14}$C samples were collected from standing snags, at Burchard and Yellow Lakes, we wiggle matched a branch and log, respectively, both buried in the landslide deposits. The branch from the deposit at Burchard Lake potentially dates to within a couple decades of landslide occurrence in 1889/90 AD, though an age from the early 1700s is possible as well (Figure 5A). The buried log at Yellow Lake predates lake formation by nearly 2,000 years (Figure 5B) with a death date no earlier than 183-89 BC.

*4.2. Temporal clustering*

Notably, we observe temporal clustering of landslides during the winter of 1889/90 AD at Burchard, Esmond, and Pearl Lakes and potentially Yellow Lake, all of which lie within ~25 km of each other (Figures 2 and 5; Table 1). We note that while one snag at Pearl Lake and all snags at Yellow Lake are western red cedar, we were able to calculate a conspicuously strong T-score between these sites and also with the absolutely dated WA129 "Long Island, Willapa Bay, Washington" red cedar chronology contributed to the International Tree-Ring Databank by Yamaguchi et al. (1997). In addition, while the lack of bark on the Yellow Lake slabs precludes sub-annually accurate dating, each collected slab dates to within a couple years of 1889/90 (1885, 1887, 1888 for three slabs; Table 1), suggesting that a similar, and likely small, amount of bark is missing from each tree. At Burchard, Esmond, and Pearl Lakes, where bark was preserved, the trees died before earlywood formed in the spring of 1890, so we cannot definitively determine whether the trees died in late 1889 or early 1890. Examination of potential landslide

70

| ID # | Lake | Lat (° N) | Long (° W) | T-value | COFECHA ISC | # yrs overlap | Lake Formation | $^{14}$C Ages |
|---|---|---|---|---|---|---|---|---|
| 1 | Beaver Dam | 45.581 | -123.387 | 10.7 | 0.709 | 247 | 1930 or more recent | - |
| 2 | Burchard | 43.668 | -123.765 | 8.5 | 0.605 | 178 | Winter 1889/90 | 1866 AD-present (snag) & 1711-1873 AD (deposit) |
| 3 | Buttermilk | 44.641 | -123.691 | - | - | - | - | 1170-1260 AD |
| 4 | Carlton | 45.320 | -123.443 | - | - | - | - | 565-590 AD |
| 4 | Slide *into* Carlton | 45.321 | -123.442 | 12.1 | 0.704 | 278 | 1849 or more recent | - |
| 5 | Esmond | 43.873 | -123.600 | 6.7 | 0.656 | 222 | Winter 1889/90 | 1685-1928 AD |
| 6 | Hamar | 44.684 | -123.620 | 5.9 | 0.641 | 184 | 1772 or more recent | - |
| 7 | Hanna | 45.377 | -123.372 | 8.1 | 0.598 | 174 | 1882 or more recent | - |
| 8 | Hemlock | 45.333 | -123.793 | 4.5 | 0.57 | 89 | 1715 or more recent | 1896-1910 AD |
| 9 | Kauppi | 45.917 | -123.294 | 6.3 | 0.775 | 178 | 1871 or more recent | - |
| 10 | Laird | 42.700 | -124.204 | 4.1 | 0.726 | 263 | 1869 or more recent | 1864-1893 AD |
| 11 | Little Lobster | 44.310 | -123.646 | 4.6 | 0.829 | 181 | 1750 or more recent | 1679-1940 AD (LaHusen et al., 2020) |
| 12 | Murphy | 45.395 | -123.491 | 4.5 | 0.854 | 206 | Winter 1850/51 | - |
| 13 | Parsons | 45.540 | -123.244 | 6.9 | 0.688 | 145 | 1855 or more recent | - |
| 14 | Pearl | 43.816 | -123.521 | 7.9 | 0.686 | 123 | Winter 1889/90 | 1682-1932 AD |
| 15 | Scoggins Valley | 45.522 | -123.262 | 5.5 | - | 67 | 1875 or more recent | - |
| 16 | Soup | 43.570 | -123.783 | 7.2 | 0.651 | 171 | 1872 or more recent | 1856-1920 AD |
| 17 | Spruce Run | 45.818 | -123.570 | - | - | - | - | 1362-1402 AD |
| 18 | Sunago | 45.690 | -123.108 | - | - | - | - | 1771-1956 AD |
| 19 | Yellow | 43.799 | -123.556 | 4 | 0.736 | 208 | 1888 or more recent | 1903-1919 AD (snag) & 183-89 BC (deposit) |

**Table 1**. **Dated landslides in the Oregon Coast Range**. Sites mapped on Figure 1 labeled according to ID#. Note that the two Carlton slides are both labeled as #4. T-values record strength of correlation between dead-collected samples and live tree chronologies. Higher T-values correspond to higher dating confidence. COFECHA interseries correlation (ISC) records the internal consistency between trees at each site. Note that three sites (Buttermilk, Carlton, and Spruce Run) are too old for dating with dendrochronology and Sunago does not exhibit a clear correlation with live trees. "Lake Formation" age is sub-annually accurate if bark was preserved on sampled snags. Otherwise ages are a maximum. $^{14}$C ages are wiggle matched from drowned snags, except for a single sample at Buttermilk Lake as well as wiggle matched samples from a buried branch and log at Burchard and Yellow Lakes, respectively. Note that listed $^{14}$C ages here include the entire range of potential ages, while Figure 5 plots the ranges corresponding to 95.4 percent of the total area of the output distributions with the highest probability from OxCal. See Table S2 for uncalibrated $^{14}$C ages.

triggers from the winter of 1889/90, however, provides a compelling explanation for landslide failure.

*4.3. Dam geomorphometry: few landslide dams at large drainage area, valley width*

We compared the upstream drainage area of landslide dams to the upstream drainage area for all mapped channel network nodes. First, we estimated the median upstream drainage area for all mapped landslide dams (n = 238) as 2.8 km$^2$. Notably, the distribution of upstream drainage area at landslide dams is distinct from the distribution of drainage area for all nodes in the channel network (includes channels with and without landslide dams), implying that landslide dams are uncommon in steep, low-order colluvial channels and in channels with drainage areas >~8 km$^2$ (Figure 6; Montgomery, 2001). Furthermore, plotted histograms for both the landslide dataset and the stream network reveal an overrepresentation of landslide dams in the landscape at drainage areas between ~3-10 km$^2$ relative to the stream network (Figure 6). In order to confirm landslide impoundment, we limit our additional analyses to dams where we have field confirmation of landslide dammed lakes. We observe that, except for Carlton Lake (drainage area of ~23 km$^2$), all landslide dams included in our analysis (Table S1) are emplaced at a drainage area <8 km$^2$ (Figure 7B). In addition, all of our dated landslides have Impoundment Indices, $I_b > 5$, which is the stability threshold that Fan et al. (2020) observed in several landslide dam compilations.

Similar to the paucity of landslide dams with upstream drainage areas >8 km$^2$, we observe a dearth of landslide dams above a threshold valley width. Specifically, all but two of the dated landslide dams occur at valley widths <80 m, and all but five occur at valley widths <60 m (n = 23; Figure 7C, Table S1), which intriguingly corresponds to the
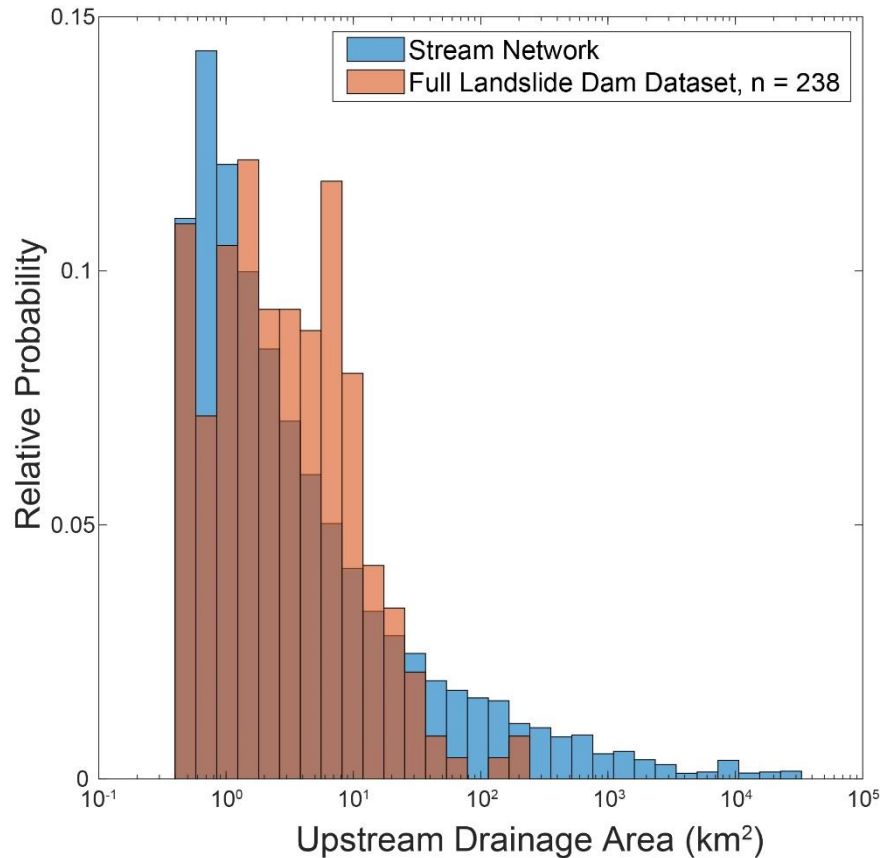
**Figure 6. Landslide dam upstream drainage area.** Histogram of upstream drainage area recorded at all mapped landslide dams (orange; black dots in Figure 1) compared to histogram of upstream drainage for all stream network nodes from 30-m SRTM DEM of western Oregon (blue). Note that landslide dams are somewhat underrepresented in the upper most channels of the drainage network (~0.5-1 km$^2$), but dams are overrepresented at drainage areas of ~1-10 km$^2$. Note paucity of landslide dams at drainage areas >10 km$^2$. Given this dataset includes all mapped dams, where field observations are limited, it is possible that not all dams currently impound lakes/marshes. Relative probability is number of data points in each bin normalized by the size of the dataset.

height of mature coastal Douglas Fir trees, ~76 m (Franklin & Waring, 1979). The two

landslides with the largest valley widths, Hamar (113.0 m) and Klickitat (87.4 m) Lakes

occur in low-gradient reaches. Hamar Lake resides in a valley bottom where a large

complex of landslides renders the relevant valley width ambiguous, and Klickitat Lake

occurs upstream from a knickpoint at a gabbroic dike that has pinned the valley and

resulted in low channel gradients. At all other sites, we suggest that valley widths are too

narrow for large woody debris to bypass and erode landslide dams. Indeed, at most dated sites, we observe large logs floating upstream of the landslide deposit, suggesting that large woody debris typically does not pass through the dams (Figure 8).

Finally, in general agreement with previous studies that suggest that stable landslide dams at high drainage areas tend to be bigger (e.g. Korup et al., 2006), we observe a weak ($R^2 = 0.2116$), though statistically significant (p<0.03), negative exponential relationship between landslide size (surface area and/or volume estimated from Larsen et al. (2010)) and local relief, such that landslide dams that occur in areas of low relief tend to be larger than their high relief counterparts (Figure 7A).

## 5. Discussion

### 5.1. Dendrochronology as a landslide dating technique

Dendrochronology is ideal for pinpointing landslide triggering mechanisms since determination of landslide age with sub-annual accuracy is often possible. Tree ring analysis, however, is not immune to dating difficulties. As our calculated landslide ages demonstrate, the lack of bark and final growth increments on multiple samples limits our ability to date landslides with the desired accuracy to link dam formation with specific triggers. In these situations, maximum landslide ages are the best possible result without further data collection. Furthermore, spurious correlations between dead- and live-collected data are possible, particularly when sample sizes are low and environmental signals may be weak. We acknowledge that sample sizes at our dated landslide-dammed lakes are low, but time series length is greater than 100 and often 150 years, crossdating is robust among samples within each site, and multiple measurement transects help maximize signal-to-noise ratios. Moreover, T-scores between dead-collected lake trees
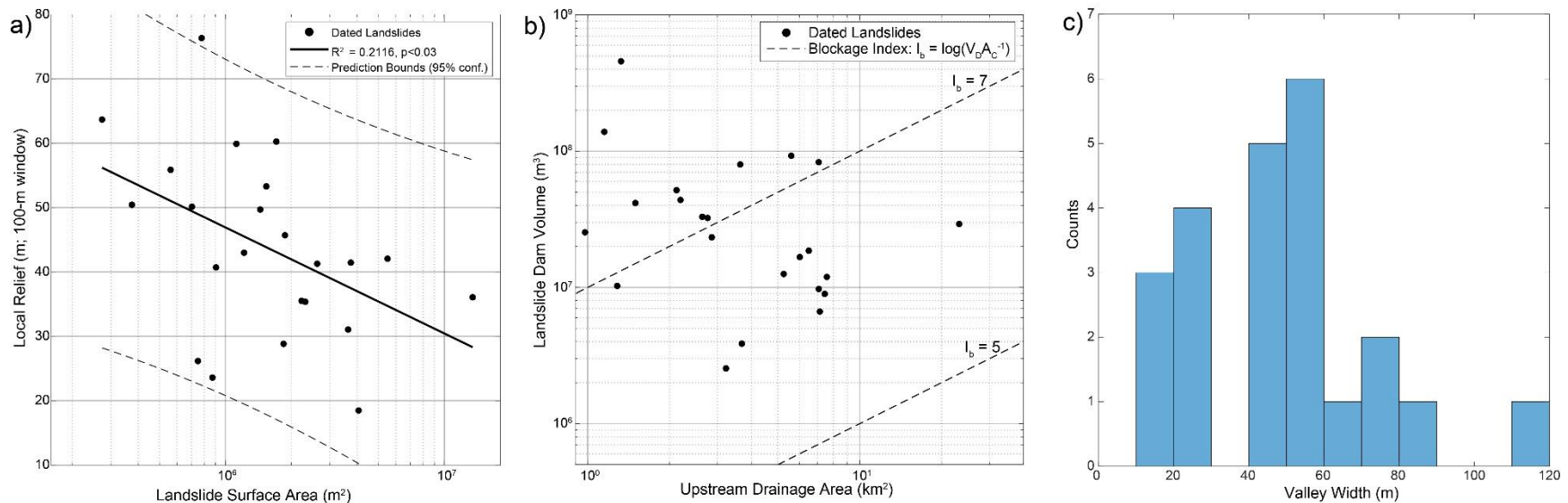
**Figure 7. Landslide dam geomorphometry**. a) Local relief (100-m window) and landslide surface area at each dated landslide dam. A weak negative exponential ($R^2 = 0.2116$), but significant ($p<0.03$), relationship between relief and landslide size. b) Landslide dam volume, $V_D$, estimated from Larsen et al. (2010) as $V_D = \alpha A_D \gamma$, where $A_D$ is landslide surface area, $\log(\alpha) = -0.836$, and $\gamma = 1.332$, plotted as a function of upstream drainage area. Note the paucity of landslides above drainage area of ~8 km$^2$. Carlton Lake is sole exception. There is no clear relationship, otherwise, between landslide size and upstream drainage area. All dated landslide dams are above the $I_b=5$ stability threshold observed by Fan et al. (2020). c) Histogram of measured valley width. All but two stable landslide dams occur below a valley width of 80 m, a length that is approximately the height of mature Douglas Fir trees. All but five stable dams occur below a valley width of 60 m. Note that the two landslide dams with the largest valley widths occurred within larger landslide complexes, making downstream valley width ambiguous.

75

and live-collected trees were sufficiently high to have a low probability of error. Importantly, ^{14}C wiggle matching corroborates dendrochronological dates, such as at Burchard, Esmond, and Laird Lakes (Figure 5A), and at sites where we are not confident in dendrochronology-derived landslide ages, ^{14}C wiggle matching often clarifies any ambiguities. Most notably, we were unable to find robust correlation coefficients and T-scores for collected samples at Carlton and Spruce Run Lakes. [14]C wiggle matching revealed that these sites pre-date existing tree ring chronologies in western Oregon (Figure 5B). Furthermore, poor internal correlation of samples at Carlton Lake reinforced the importance of careful geomorphic field observations when collecting samples. Specifically, a second landslide occurred after the primary damming event on the north side of Carlton Lake. This smaller landslide formed some small sag ponds where we also collected slabs from dead snags. While we were aware of this secondary slide during sampling, we were not certain whether the trees died during the primary or secondary failure. The lack of intercorrelation between all collected trees but strong intercorrelation between trees collected upstream from the primary dam and those sampled at the secondary failure, respectively, clearly distinguishes two separate tree mortality events at Carlton Lake, with the primary damming event occurring no earlier than 565-590 AD and the secondary failure after 1849 AD.

Similarly, at Yellow Lake, conflicting dendrochronology and ^{14}C wiggle matching ages reinforce the importance of careful field observations. The age of the log buried in the landslide deposit (183-89 BC) pre-dates the dendrochronology-derived landslide age by two millennia. Lidar data appear to show a history of several failures and reactivations within the landslide deposit at Yellow Lake (Figure 2C). It is possible,

**Figure 8. Large wood upstream from landslide dams.** a) Esmond Lake (formed winter 1889/90), looking upstream from dam. Note logs that are tilting are partially buried by the landslide dam. b) Ayers Lake (formed December 1975), looking upstream from dam. c) Pearl Lake (formed winter 1889/90), looking downstream towards the deposit. d) Burchard Lake (formed winter 1889/90), looking downstream towards dam from delta at upstream end of lake. For scale, note that large snag in middle is same as that in Figure 3A.

therefore, that the log was buried and preserved prior to lake formation sometime after

1888 AD. Given the log was clearly entrained in the deposit among blocky landslide

debris this is our preferred interpretation. Nevertheless, the discrepancy in calculated

landslide ages here reinforces that ^{14}C dating must be undertaken carefully and coupled

with landscape interpretation using high resolution topographic data when possible.

There is likely a preservation bias in dated landslide-dammed lakes, as 1) the

oldest landslides deposits erode over time and impounded valleys fill up with sediment,

and 2) snags at older sites become more decayed, limiting our ability to date older slides, including those that may have occurred during the 1700 AD earthquake. However, the dating of Spruce Run, Buttermilk, and Carlton Lakes to ~300, ~500, and ~1200 years, respectively, *prior* to 1700 AD suggest that tree decay does not preclude dating of events associated with the last CSZ earthquake. Indeed, several landslides date to the 1700s AD (Figure 5A, Table 1), and wood is often well preserved at these sites. Due to logistical and safety concerns, our sampling technique is currently limited to slab extraction above or near water level, though excavation into adjacent sediment often exposes bark. Wood preservation, however, is greatly enhanced underwater, where trees in western Oregon have been observed to remain intact for >3,000 years (Deligne et al., 2013). Future underwater tree ring sampling may provide an expanded inventory of potentially datable landslide-dammed lakes.

While the last CSZ earthquake occurred in January 1700 AD, earlier CSZ earthquakes may have also triggered landslides. We note that while the ages of Spruce Run, Buttermilk, and Carlton Lakes fall within uncertainty of the T2A (1402 ± 114, 122 AD), T3 (1154 ± 109, 117 AD), and T4A (528 ± 126, 137 AD) CSZ events, respectively, as recorded by Goldfinger et al. (2012), the uncertainty in calibrated $^{14}$C ages and decay of outermost rings on drowned snags does not allow for explicit linkage of these CSZ events with landsliding (Struble et al., 2020). Future extension of tree ring records in western Oregon, however, may allow for improved ages at Spruce Run, Buttermilk, and Carlton Lakes, and thus a more robust comparison to CSZ earthquake records.

Finally, continued construction of a large dataset of dendrochronologically-dated landslides in western Oregon improves our ability to date landslides throughout the OCR

and Pacific Northwest. Dated dead-collected samples extend the western Oregon tree ring record, allowing for dating of even older landslide events. Furthermore, dating of landslides from various parts of the OCR and adjacent mountain ranges, where interannual climate variability is comparable, allows for multiple checks on dating. For example, dating between lake-collected trees and the Marys Peak chronology was identical, if not somewhat stronger, than dating between the same lake-collected trees and Douglas Fir chronologies from the western Cascade Range. As such, extensive dating of landslides not only improves our ability to date even older landslides, but it allows us to move further afield in dating efforts. In addition, continued extension of the tree ring record over a broad region will facilitate reconstruction of paleoclimate of the Cascadia region for the past 1-2 ka.

*5.2. Landslide triggering: Atmospheric rivers*

We observe that impoundment of valleys by landslide dams has been persistent throughout the OCR since the last CSZ earthquake in 1700 AD. In general, we observe that bedrock landslide dams have been emplaced more often than has been often assumed, and multiple landslides that could be considered historic (Figure 5A), were not documented. The lack of a single landslide age that corresponds with the 1700 AD earthquake, while at first surprising and contradicting the oft-held assumption that most OCR deep-seated landslides are coseismically triggered, supports and reinforces recent interpretations that OCR slope failures may often be a result of large hydrologic events such as ARs (LaHusen et al., 2020; Struble et al., 2020). Indeed, shallow landslides and some deep-seated failures have been historically observed to coincide with major AR events, including the 1996/97 floods in western Oregon (e.g. Schmidt et al., 2001; Wiley,

79

2000). Temporal clustering of landslides to the winter of 1889/90 AD, which corresponds to prolonged heavy snow followed by warm, heavy rain, likely from one or more atmospheric rivers, demonstrates that multiple deep-seated landslides that impound streams can be triggered in a single or short sequence of storms.

Major flooding was widely observed throughout western Oregon and northern California in early February 1890. Comparison of recent instrumented flooding events (e.g. 1964, 1996/97) to historical accounts, suggest that the February 1890 flood was the second largest flooding event in western Oregon, after the 1861/62 floods (Andree, 1910; Harden et al., 1978; Miller, 1999). We note, however, that 20th century dams built on many major catchments in western Oregon complicate comparison of the 1890 flood extent to the largest events of the twentieth century (e.g. Rantz, 1959). Although we are generally unable to locate measurements of rainfall or streamflow during the winter of 1889/90 in western Oregon (most measurements did not begin until 1892), some rainfall measurements were recorded in coastal northern California as was a single stage reading from the Willamette River in Portland, Oregon. Crescent City, California (~25 km from Oregon border), notably, received 17.2 in (436.8 mm) of rain between January 31 and February 4, 1890 (Harden et al., 1978), while the Willamette River peaked at 28.4 feet (8.66 m) in Portland on February 6, 1890 (Andree, 1910). While such rainfall totals are significant, the runoff responsible for major flooding and landsliding was not strictly derived from rainfall. As has been the case for many major floods in western Oregon, historic accounts record that the 1890 flood was preceded by cold weather and heavy snow, which fell from late December 1889 until early February 1890 (Harden et al., 1978; Petersen, 1948). Rapidly melting snow may have contributed to the runoff from the

warm and heavy rains, such that flooding incorporated a significant snowmelt component (Harden et al., 1978). Landslides were observed throughout western Oregon, including a landslide that dammed Cow Creek, the southernmost Umpqua River catchment, for several days. Unfortunately, historic records are not clear about the exact location of this landslide, and subsequent construction of roads and railroads along Cow Creek have obscured any obvious signature of a landslide dam. In addition, a large debris flow temporarily dammed the Siuslaw River north of Mapleton, Oregon, but was breached within two to three days (44.047 N, -123.880 W; Petersen, 1948).

Although we are unaware of recorded measurements of streamflow or sediment flux during the 1890 flooding event (except for the single stage measurement in Portland; Andree, 1910), Richardson et al. (2018) observe an event bed that they date to 1890 AD in a lake core from Loon Lake (43.595 N, -123.847 W), which lies ~10 km west of Burchard Lake, the nearest member of the 1890 landslide cluster (Figure 2). The 1890 event bed records a marked increase in lake sedimentation, comparable to other sedimentation peaks that Richardson et al. (2018) posit are a result of great earthquakes and anthropogenic land use impacts. Curiously, they do not observe a prominent event bed corresponding to the 1861/62 flood, widely considered the largest historic flood in western Oregon, though they do observe an increase in sedimentation from the 1964 floods, which they partially attribute to timber harvest and land-clearing. The Coos Fire, which burned much of the southern OCR in 1868, including portions of the Loon Lake catchment (Zybach, 2003), occurred a couple decades prior to the 1890 floods, potentially explaining the disparate sediment response to flooding in 1862 and 1890 in the Loon Lake core (Richardson et al., 2018). The 1890 landslide cluster likely did not

occur on hillslopes burned by the Coos Fire (Zybach, 2003). Nevertheless, the striking correspondence between high sedimentation in Loon Lake and temporal clustering of nearby landslides emphasizes the significance of the 1890 flood over the observable record.

In the 20th century, few catastrophic bedrock landslides have produced dams that impound long-lived lakes in the OCR, with the only known exceptions being Ayers Lake in 1975 (Thrall et al., 1980) and Beaver Dam Lake sometime between 1930 and 1953 (Figure 5), possibly due to the stand-replacing Tillamook Fire in 1933 (Zybach, 2003). The relative paucity of recent deep-seated landslide dams in the OCR, therefore, implies that storms of a similar magnitude to those that caused the February 1890 floods have not occurred in the past century and/or western Oregon in the nineteenth century experienced an anomalously high number of intense major atmospheric rivers. Indeed, our landslide ages not only demonstrate temporal clustering in the winter of 1889/90, but record several landslide damming events throughout the 19th century. However, numerous prolonged ARs have been observed since the major 1890 floods, many of which triggered tens of thousands of debris flows (e.g. Schmidt et al., 2001; Wiley, 2000), though these failures did not form landslide-dammed lakes. While clarification of this discrepancy is beyond the scope of this work, consideration of factors such as snowmelt, land use, fire suppression, and changes to the El Niño-Southern Oscillation or Pacific Decadal Oscillation, both of which could be examined with lengthened tree ring records, would be useful for explaining potential changes in AR intensity and propensity for landslide-dammed lake formation.

*5.3. Landslide triggering: crustal fault earthquakes*

While no landslide clearly corresponds to the 1700 AD CSZ earthquake, smaller crustal faults in the Cascadia forearc are capable of producing ground motion that can trigger landslides. While recorded earthquakes in the 1800s, the time period corresponding to the bulk of our dated landslides, are sparse, some noteworthy events may have left an imprint on the OCR landscape. Firstly, a $M_w$ ~6.75 earthquake on November 23, 1873 was felt throughout northern California and southern Oregon, with the most intense ground motion in Crescent City, California, though shaking was felt as far north as Portland, Oregon (Wong & Bott, 1995). While the fault that triggered the 1873 earthquake is unknown, the maximum ages of Laird (max age 1869 AD) and Soup (max age 1862 AD) Lakes and their proximal locations to northern California do not preclude seismic triggering by this earthquake, though the lack of preserved bark on sampled trees does not make such a specific linkage currently possible. Furthermore, the Gales Creek Fault and similar crustal faults in the northern OCR may produce ground motion sufficient to destabilize hillslopes (McPhee et al., 2014; Wells et al., 2020; Wong & Bott, 1995), though whether there have been any recent earthquakes that may correspond to the landslides we date here is unclear.

*5.4. Dam persistence and stability*

Based on the Impoundment Index of Korup (2004), all our dated landslide dams fall well within the "stable" category (Figure 7B). Given these dated landslide dams have clearly been stable for >~100 years (Figure 5), this result is not surprising; however, the paucity of landslides above a drainage area of ~8 km$^2$, even at drainage areas where $I_b$>5, suggests other processes dictate landslide dam stability in the OCR at high drainage

areas. The drainage area where we observe a paucity of landslide dams, ~8 km$^2$, approximately corresponds with where smaller OCR streams empty into larger third order channels, which suggests that while we do not observe a systematic correlation between landslide size and drainage area, the abrupt increase in drainage area and/or valley width at these confluences serves as the threshold of stability for such dams. The dams with the largest upstream drainage areas, particularly at Triangle (137.6 km$^2$), Loon (230.6 km$^2$), and Sitkum (208.2 km$^2$) Lakes all occur within the southern Tyee Formation, which is composed of highly indurated and blocky sandstone beds that may be more likely to remain stable (Lane, 1987). In addition, deep-seated landslides in the OCR are often structurally controlled, such that dip slopes tend to fail more readily (Roering et al., 2005). The correspondence between landslide size and local relief may be partially explained by such regional patterns in structurally controlled relief (Figure 7A; Roering et al., 2005). Further, Baldwin (1958) noted that many landslide dams in the OCR are composed of weak, poorly consolidated, weathered Tyee Formation and are only stable in small catchments. Most dams, particularly at high drainage areas, fail quickly (Baldwin, 1958). For instance, he noted that a landslide-dammed lake formed on Camp Creek, near the Umpqua River, in the winter of 1955/56, and he suggested that the combination of poorly consolidated landslide material and a large drainage area resulted in rapid lowering of the lake and subsequent disappearance of the dam (Baldwin, 1958). This mirrors historic observations of the landslide that dammed Cow Creek and debris flow that dammed the Siuslaw River in February 1890 AD. Cow Creek and the Siuslaw River both have large drainage areas, so prolonged stability, even without anthropic intervention in the case of Cow Creek, was unlikely.

Our observation of dense large woody debris accumulation behind landslide dams (Figure 8) and a scarcity of stable landslide dams at valley widths >80 m (Figure 7C) suggests that landslide dams in the Oregon Coast Range are not only protected from the erosional effects of through-flowing floods and debris flows by the extensive, low-gradient reaches behind the dam, but also by large wood armoring and potentially structurally supporting the deposits. While thorough measurement of large wood at lake outlets and within deposits is beyond the scope of this analysis, large wood likely plays a major role in catchment dynamics and longer timescale ($>10^3$ yr) evolution of headwater channels in the OCR. Indeed, this drainage area and corresponding valley width corresponding to a threshold transport capacity of large wood has been observed in an extensive literature of large wood and rivers, particularly in Cascadia (e.g. Baillie et al., 2008; Benda, 1990; Benda et al., 2003; Lancaster et al., 2001; Lancaster & Grant, 2006; Wohl, 2017 and references therein), as has the ability of large wood to slow flows during flood events and limit substrate erosion (e.g. Hinshaw et al., 2020). Hence, without the battering effects of through-flowing wood and coarse sediment, particularly in the OCR where the Tyee Formation produces ethereal gravels that degrade exceptionally quickly (O'Connor et al., 2014), downcutting by sediment-starved water is the primary means of incision through the deposits, allowing for prolonged landscape residence times. At dams where landslide material is exceptionally resistant and blocky, such as at the large Sitkum and Loon deposits, large blocks, often >10 m (LaHusen et al., 2020; Lane; 1987; this study), further inhibit channel incision into the landslide deposits (e.g. Shobe et al., 2016). Finally, some sites where channels have formed epigenetic gorges on old bedrock

hillslopes, such as at Triangle Lake (Lane, 1987), may be more likely to remain stable for a prolonged period.

The stability of landslide dams in the OCR has broad implications for sediment transport and storage throughout the OCR (Benda, 1990; Benda et al., 2003; Lancaster & Grant, 2006). As these landslide dams are copious throughout the OCR, they serve as invaluable archives and recorders of fire, earthquakes, anthropogenic landscape impacts, paleoclimate, and erosion rates (e.g. Marshall et al., 2017; Richardson et al., 2018). Landslide dam stability further promotes diverse aquatic habitats and ecological complexity in mountain streams (Baillie et al., 2008; Beeson et al., 2018; Mackey et al., 2011; May et al., 2013). These factors, in addition to the contribution of landslide dams to surface processes that act over timescales pertinent to landscape evolution (Korup, 2004; Korup et al., 2006) and potentially to carbon sequestration (Bilby & Likens, 1980; Scott & Wohl, 2020), necessitates close future detailed examination of this important geomorphic process.

## 6. Conclusions

We identify >200 landslide-dammed lakes in the Oregon Coast Range and establish age control for 20 of these sites. Calculated landslide ages demonstrate that the Oregon Coast Range has experienced episodic emplacement of persistent landslide dams since the 1700 AD subduction zone earthquake, suggesting that major hydrologic events trigger or reactivate a significant proportion of slope failures observed throughout the range. Furthermore, in addition to landslides historically observed in February 1890, temporal clustering in the winter of 1889/90 AD of *at least* 4 landslides, the only dated landslides in the Oregon Coast Range observed to temporally cluster to the same year,

reinforces that atmospheric rivers are major contributors to slope instability in Cascadia. We further observe that stable landslide dams have a threshold drainage area and valley width, which we attribute in part to the inability of large woody debris to be transported and pass over landslide dams at these locations in the landscape. The congregation of large wood on the upstream side of landslide dams may then serve as a dam preservation mechanism, such that wood armors the upstream side of dams and tempers the largest floods that may inundate the low-gradient valleys upstream from landslide deposits. The growing dataset of dated landslide dams in the Oregon Coast Range provides unprecedented temporal detail of landslide dam emplacement. Continued clarification of the timing of landsliding in the Oregon Coast Range warrants further examination of the mechanisms that support landslide dam stability, the anthropogenic, fire, and climatic impacts that trigger such failures, and the subsequent implications for ecological stability and diversity, sediment storage, carbon sequestration, and landscape evolution.

**7. Bridge**

In Chapter III, I utilized dendrochronology to accurately date 20 landslide dams in the Oregon Coast Range. Notably, I observed temporal clustering of at least 4 landslides to the winter of 1889/90 AD, corresponding to one or a series of atmospheric rivers that produced likely the second largest recorded flood in western Oregon. Further, I noted that there exists a paucity of landside dams at drainage areas $>8$ km$^2$ and $>80$ m. I attributed this change in dam preservation due to the accumulation of large woody debris upstream from landslide dams. I suggested that large woody debris tempers flow from the largest floods and prevents transit of debris flows and coarse sediment. In order to more specifically consider how landforms of particular scales control the stability and extent of

drainage basins, I utilize topographic transformation techniques, including continuous

wavelet transforms and Gaussian filtering to identify characteristic landforms in the

Cascadia forearc and predict future drainage basin reorganization.

## CHAPTER IV

## CHARACTERISTIC SCALES OF DRAINAGE REORGANIZATION IN

## CASCADIA

Reproduced with permission from Struble, W.T., Roering, J.J., Dorsey, R.,

Bendick, R., (in revision). Characteristic Scales of Drainage Reorganization in Cascadia.

*Geophysical Research Letters*.

### 1. Introduction

The dynamic and tenuous nature of watershed boundaries, which define water

resources, aquatic habitat, and the flux of sediment and organic materials, is readily

apparent in landscapes that exhibit stream capture and drainage divide migration. The

spatial extent and morphology of terrestrial river networks are dictated by the

contribution of uplift acting over multiple spatiotemporal scales and the competing

effects of erosion superimposed on variable bedrock lithologies (e.g. Forte et al., 2016;

Gallen, 2018; Goren et al., 2014; Mitchell and Yanites, 2019; Whipple et al., 2017b).

Where landscapes exist in a state of disequilibrium, such that drainage network

morphology is not well adjusted to external drivers of uplift or erosion, channels respond

by vertically incising or steepening (or aggrading and gentling; e.g. Kirby and Whipple,

2012), and drainage divides that separate adjacent catchments may horizontally migrate

(e.g. Goren et al., 2014; Whipple et al., 2017b; Willett et al., 2014). As such, as uplift and

erosion fluctuate over space and/or time, drainage basins continually evolve and morph

from prior configurations in order to move toward 'steady state' (Goren et al., 2014;

Willett et al., 2014), though reorganization may continue long after significant uplift

ceases (Beeson et al., 2017).

Prediction of the topographic scales responsible for setting drainage basin boundaries, and consequently the geophysical processes that drive drainage reorganization, has been an ongoing effort. River systems on Earth deviate markedly from predicted drainage pathways defined by long wavelength (>1000 km) topography owing to tectonic processes that act over shorter wavelengths and timescales, unlike on other planetary bodies such as Mars or Titan (Black et al., 2017). In terrestrial landscapes undergoing drainage reorganization, unstable divides appear to migrate toward long wavelength filtered (synthetic) topographic divides (Moodie et al., 2018; Wegmann et al., 2007). However, the precise scale of landforms that define the extent and stability of drainage basins remains unclear. Furthermore, while the direction of divide migration and in some cases the magnitude of disequilibrium can be predicted by local relief and river steepness (Forte and Whipple, 2018; Whipple et al., 2017b), hillcrest asymmetry (Mudd and Furbish, 2005), and the $\chi$ metric, an integrated quantity of drainage area along a river profile (Perron and Royden, 2013; Willett et al., 2014), it is challenging to define the scale of processes responsible for drainage basin disequilibrium or diagnose why catchments exist in a state of dynamic adjustment (O'Hara et al., 2019; Whipple et al., 2017a; Yang et al., 2015).

Signal processing has proven successful in topographic and geophysical studies including drainage network and stream profile analysis (Black et al., 2017; Moodie et al., 2018; Roberts, 2019; Roberts et al., 2019; Wegmann et al., 2007), landform extraction and morphometrics (Doane et al., 2019; Lashermes et al., 2007; Perron et al., 2008; Sare et al., 2019), and measurement of lithospheric thickness, mantle flow, and crustal strain rates (Audet, 2011, 2014; Bomberger et al., 2018; Davies et al., 2019; Turcotte et al.,

2002). Here, we demonstrate that 2-dimensional continuous wavelet transforms of topography highlight the scale of landforms defined by local structural, lithologic, and baselevel controls as well as regional landforms defined by subduction and mantle flow; many of these landforms do not correspond with mapped drainage divides. In addition, we separately establish the scale-dependency of drainage basins by mapping synthetic drainage networks on topography Gaussian filtered to progressively longer wavelengths. Where the elevation and location of topographic highs differ between Gaussian filtered digital elevation models, major river divides appear to migrate. We isolate the scale-dependency of drainage basins by quantifying the similarity between synthetic drainage basin boundaries and those of the actual landscape by using the Jaccard Similarity Index, a statistic of the degree of overlap (i.e. similarity) between sample sets (Jaccard, 1900).

We focus on the central and southern Cascadia forearc, including the Klamath, Rogue, Umpqua, and Willamette Rivers (Figure 1), where drainage reorganization is a common and ongoing process. Multiple large discrete stream captures have been mapped at the crest of the Oregon Coast Range (OCR) along the western margin of the Willamette Valley (WV; Baldwin and Howell, 1949; Chylek, 2002; Moeller, 1990; Niem, 1976) and in the Umpqua and Rogue River catchments (Figures 1, S2, and S3), where rivers that used to flow directly from the Cascades to the Pacific Ocean (arc-to-coast) were diverted into margin-parallel catchments such as the Willamette River. The driver of these reorganization events, including the role of uplift in the OCR, remains ambiguous; potential controls on river network changes include crustal faults bounding alluviated valleys that contribute to basin subsidence and geomorphic adjustment (Blakely et al., 2000; von Dassow, 2018; Wells et al., 1998, 2017; Yeats et al., 1996) as

well as deeper subduction processes (e.g. Becker et al., 2014; Blakely et al., 2005; Delph et al., 2018; Ramachandran et al., 2006).
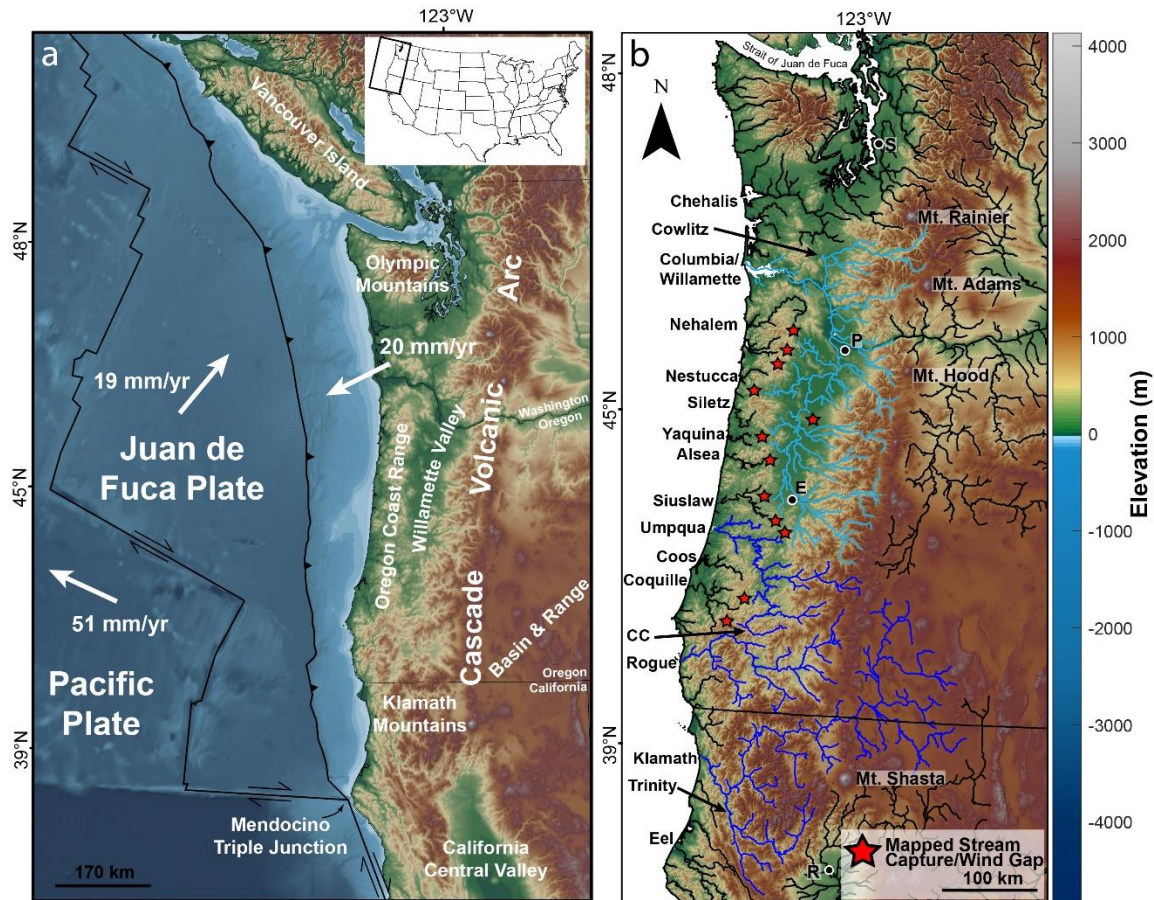


**Figure 1. Study area. a)** Regional tectonics of Cascadia subduction zone. Arrows are absolute plate motions in a hotspot reference frame (DeMets et al., 2010). Modified from Bodmer et al. (2019). **b)** Map of study area, extending from northern California to the Strait of Juan de Fuca. Significant forearc rivers labeled at their outlet in the Pacific Ocean. Light blue: forearc-draining portions of Columbia River, including Willamette River. Note that the Willamette, which empties into the Columbia at Portland, is labeled concurrently with the Columbia. Dark blue: arc-to-coast rivers focused on in this study (Umpqua, Rogue, Klamath Rivers). Arrows point to notable tributaries: Cow Creek (CC) and the Cowlitz and Trinity Rivers. Red stars are wind gaps and stream captures previously mapped or noted here. Basin and Range Province rivers omitted. Cities: **R:** Redding, **E:** Eugene, **P:** Portland, **S:** Seattle.

## 2. Methods

We utilized 3-arc-second (90 m) Shuttle Radar Topography Mission (SRTM) digital elevation models (DEMs), a sufficient resolution to ensure that major rivers route

correctly and low-relief drainage divides are accurately resolved. To visualize the pattern

of dominant landforms over various wavelengths <200 km, we applied continuous

wavelet transforms to a DEM spanning the entire Cascadia margin. This analysis enables

us to identify the wavelengths at which particular physiographic features become readily

apparent. Separately, in order to identify the scales at which discrete changes in

catchment boundaries and substantial modifications to the regional drainage network

configuration occur, we filtered (i.e. smoothed), topography over progressively longer

wavelengths using Gaussian filtering and mapped synthetic drainage networks and

corresponding drainage divides. We then quantified the similarity of these synthetic

drainage basins to those generated for the unfiltered DEM to establish the scale-

dependency of the drainage network and constrain the topographic wavelengths that are

responsible for drainage basin evolution.

*2.1. Continuous Wavelet Transforms: Ricker Wavelet*

We applied a 2D continuous wavelet transform (CWT) to the SRTM topographic

data using the Ricker (Mexican Hat) wavelet. The Ricker wavelet is often used in

topographic analyses (Booth et al., 2009; Malamud and Turcotte, 2001; Turcotte et al.,

2002) and depicts the Laplacian of topography (Lashermes et al., 2007; Torrence and

Compo, 1998), revealing concave and convex regions (Figure 2). These mapped concave

and convex regions, or landforms, reveal dominant features as defined by the wavelet

scale. Hence, unlike a Gaussian filter, which removes high-wavenumber information, or a

band-pass filter, which isolates a range of wavelengths, the CWT allows for visualization

of topography corresponding to a specific wavelength. High magnitude wavelet

coefficients denote where the wavelength of topographic curvature corresponds well to

the specified wavelet scale. Thus, a large positive (negative) wavelet coefficient at a particular wavelength indicates that topography is strongly convex (concave) at that wavelength.

The CWT using the Ricker wavelet is computationally efficient, has few edge effects, and does not assume stationarity (constant mean, variance) of topographic data (Torrence and Compo, 1998). The generalized 2D CWT, with a wavelet scale parameter s, elevation z, and location (u,v) is given as

$$C(s, u, v) = \frac{1}{s} \int_{-\infty}^{\infty} \int_{-\infty}^{\infty} z(x, y) \psi\left(\frac{x-u}{s}, \frac{y-v}{s}\right) dxdy, \tag{1}$$

where $\psi$ is a wavelet family and C is the resultant wavelet coefficient. Hence, the 2D CWT is a convolution of z and $\psi$,

$$C(s, u, v) = \frac{1}{s} z(x, y) * \psi\left(\frac{x-u}{s}, \frac{y-v}{s}\right). \tag{2}$$

A wavelet with a large wavelet scale, s, produces a broad $\psi$ that reveals long wavelength elements in z, while small values of s produce a small $\psi$, which in turn defines the finer features in z. In other words, a large (small) wavelet scale extracts long (short) wavelength features in topography.

We defined the relevant scale, s, of the Ricker wavelet using its Fourier wavelength, which is the inverse of its band-pass frequency (Foufoula-Georgiou and Kumar, 1994; Mallat, 1999). The Fourier wavelength for a derivative of a Gaussian is defined as

$$\lambda = \frac{2\pi s}{\sqrt{m+\frac{1}{2}}}, \tag{3}$$

where m is the mth derivative of a Gaussian (Torrence and Compo, 1998). Since the Ricker wavelet is the negative second derivative of a Gaussian, m = 2. Hence, larger

wavelet scales, s, correspond to larger topographic wavelengths, λ. Reorganizing

Equation 3, we solved for s for each topographic wavelength of interest, in this case

wavelengths from 5 km to 200 km in increments of 5 km. For each wavelength, we then

used Equation 2 to convolve topography with the 2D Ricker wavelet, given as,

$$\psi_R(x,y) = (2 - x^2 - y^2) \, exp\left[-\frac{1}{2}(x^2 + y^2)\right]. \tag{4}$$

The resultant wavelet coefficients output from Equation 2 signify concave and convex

topographic landforms corresponding to the input wavelet scale (Figure 2).

*2.2. Gaussian Filter and Jaccard Similarity Index*

To characterize the scale-dependence of forearc drainage networks, we filtered

(i.e. smoothed) the raw SRTM topographic data using a 2D Gaussian function in 5-km

increments up to 200 km. We used the resulting filtered DEMs to map synthetic drainage

networks and drainage divides. Thus, the resultant drainage networks are *those that*

*would form without the influence of topography that corresponds to a wavenumber*

*higher than the filter scale*. The 2D Gaussian function is defined as,

$$\psi_G(x,y) = \frac{1}{2\pi\sigma^2} \, exp\left[-\frac{(u-x)^2 + (v-y)^2}{2\sigma^2}\right]. \tag{5}$$

For each topographic wavelength (5-200 km), we solved for the appropriate scale, s, of

the filter using the Fourier wavelength of a Gaussian function, defined in equation 3. For

a 2D Gaussian function, m = 0 (Torrence and Compo, 1998). We filtered the raw

topography DEM with the appropriately scaled Gaussian function by convolution of $\psi_G$

with topography, z, as denoted in equation 2, thus producing a smoothed DEM (Figure

S4).

We produced synthetic drainage networks that correspond to each Gaussian

filtered DEM by routing flow over each filtered DEM with the D8 flow routing algorithm

in MATLAB using TopoToolbox (Schwanghart and Scherler, 2014), and we mapped the resulting synthetic drainage divides for forearc catchments with trunk channels that drain to sea level (Figures 3, S1, and S4). These synthetic stream networks are those that would form without any influence of landforms smaller than the scale of the Gaussian filter wavelength. We clipped the Columbia River at the crest of the Cascades in the Columbia River Gorge to limit the drainage divides to those that flow into the WV.

In order to pinpoint the wavelengths at which discrete changes to drainage basins occur, we calculated the similarity between each synthetic and unfiltered drainage basin using the Boolean Jaccard Similarity Index (JSI; Jaccard, 1900; Levandowsky and Winter, 1971), defined as:

$$JSI = \frac{|B_o \cap B_f|}{|B_o| + |B_f| + |B_o \cap B_f|}, \tag{6}$$

where $B_o$ is the original, or unfiltered, drainage basin and $B_f$ is the synthetic drainage basin. When JSI = 1, $B_o$ and $B_f$ are identical while when JSI = 0, the drainage basins have no overlap. Thus, fluctuations in JSI correspond to changes in drainage basin extent in the Gaussian filtered DEMs (Figure 4). Specifically, gradual and abrupt drops in JSI at particular wavelengths correspond to synthetic divide migration and stream capture, respectively, between drainage basins in Gaussian filtered and unfiltered DEMs (Figure 4). JSI has been used previously to quantify divide migration between timesteps in a landscape evolution model (O'Hara et al., 2019) and how well modeled lava flows predict real flows (Richardson and Karlstrom, 2019). Our use of JSI here, however, is the first to quantify the scale-dependency of drainage network boundaries as a function of topographic wavelength.

Since Gaussian filtering tends to "smear" topography, thus shifting the coastline and decreasing JSI, we clipped both filtered and unfiltered drainage basin outlets at sea level defined in unfiltered topography. We additionally measured the Euclidean distance between drainage divides mapped on unfiltered and filtered topography to illustrate the offset between synthetic and actual drainage divides (Figure S1).

## 3. Results

### 3.1. 2D CWT reveals Cascadia forearc landforms

The 2D CWT of topography for each applied wavelet scale reveals concave and convex landforms corresponding to particular wavelengths. In other words, high-magnitude wavelet coefficients for a particular scale denote landforms well characterized by that wavelength. Specifically, at small wavelengths (<30 km) we observe that high magnitude wavelet coefficients highlight and correspond well with hillslopes and valleys, volcanoes in the Cascades, and shallow crustal structures, such as normal fault-bounded mountain ranges in the Basin and Range Province (Figure 2A). As wavelength increases, regional landforms that span multiple river catchments become more apparent (Figure 2B). Specifically, for wavelengths at which the contribution of subduction zone deformation is dominant (~80-160 km; Becker et al., 2014; Bomberger et al., 2018 and references therein), the coastal ranges and Cascades arc continuously traverse the entire length of the subduction zone. We similarly observe persistent lengthening of the WV as it merges with nearby depositional basins in the southern and northern extents of the margin (Figure 2C), including the Puget Lowland. We note, however, that connectivity exists between arc-parallel lowland terrain at wavelengths as small as 45 km (Figure 2B). At wavelengths of 100 km and higher, this Cascadia Forearc Lowland extends along the

97

entire margin of the subduction zone, from the Strait of Georgia in the north to Mount

Shasta in the south (Figure 2D-F). While the coastal ranges become less prominent at
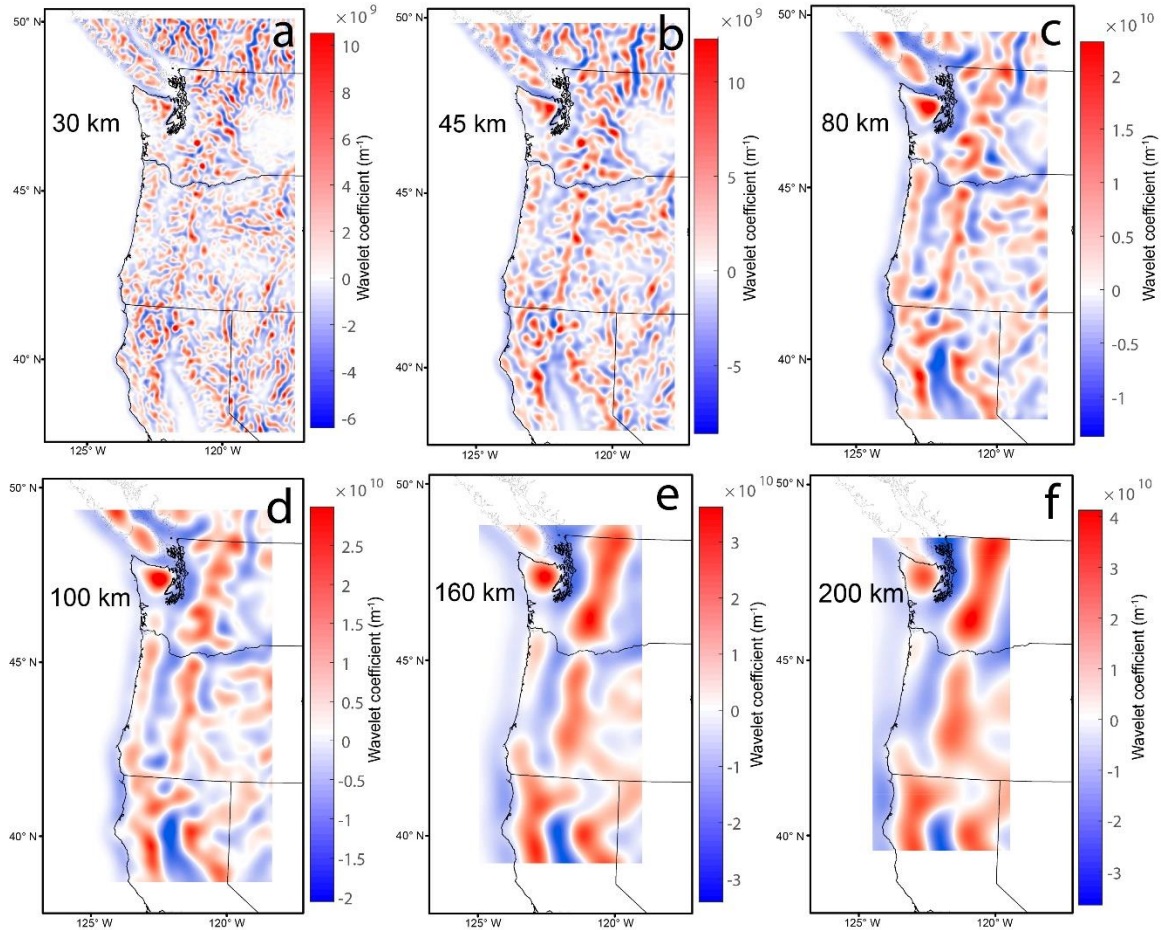


**Figure 2. 2D Continuous wavelet transform (CWT) of topography.** 2D CWT reveals convex (red) and concave (blue) regions corresponding to specified wavelength. Dominant landforms observed: **a)** 30 km wavelength: Hillslopes and valleys, potentially corresponding with lithologic contrasts and shallow crustal faults (Basin and Range). Cascades volcanoes (Mounts Rainier, Shasta, Adams) apparent. **b)** 45 km: Broader landforms reveal influence of regional tectonics. WV displays connectivity with neighboring drainage basins. **c)** 80 km: WV and other forearc lowlands consolidating. **d-e)** 100-160 km: Cascadia Forearc Lowland clearly apparent. **f)** 200 km: Olympic and Klamath Mountains and Cascades Arc persist. Growing white space corresponds with clipped wavelet edge effects, a width approximately four times the wavelet scale.

wavelengths >150 km, the high-elevation Olympic and Klamath Mountains remain

pronounced, potentially a reflection of rapid uplift rates associated with localized mantle

upwelling (Balco et al., 2013; Bodmer et al., 2019; Kelsey et al., 1994). Finally, the

longest analyzed wavelengths (~160-200 km) correspond to integrated whole-lithosphere

effects such as gravitational potential flows and coupling with mantle flow, most

apparent in the Cascades and High Lava Plains (Figure 2E-F; Becker et al., 2014;

Faccenna & Becker, 2020). We acknowledge, however, that the limited size of our study

area and the clipping of edge effects (e.g. Figure 2F) lends caution to our analysis of

these longest wavelength landforms.

*3.2. Synthetic drainage networks reveal the future of Cascadia forearc drainages*

Stream captures are common along the western margin of the WV and Cascadia

Forearc Lowland, where rivers that previously flowed from the arc to the coast were

diverted into the Willamette River (Figures 1 and S2; Baldwin and Howell, 1949;

Chylek, 2002; Moeller, 1990; Niem, 1976). The extension of the WV in 2D CWT

topography beyond its mapped drainage divides and the observation that stream capture

is an ongoing process that appears to be migrating south through time (Baldwin and

Howell, 1949; Chylek, 2002), encourages an examination of how the drainage network is

adjusting to long wavelength landforms and variations in uplift rate between the OCR

and the Cascadia Forearc Lowland.

To constrain the scale dependence of the Cascadia drainage network, we

calculated JSI for the Willamette, Umpqua, Rogue, and Klamath Rivers, as they remain

coherent drainage basins across a wide range of wavelengths. JSI values for the Rogue

and the Umpqua Rivers gradually decrease as Gaussian filter wavelength increases, up to

~15 km, at which point the synthetic divide between the Umpqua and Rogue Rivers shifts

northward as the synthetic Rogue River captures Cow Creek (Figures 1 and S1), the

southernmost tributary of the Umpqua River that was recently captured from the Coquille
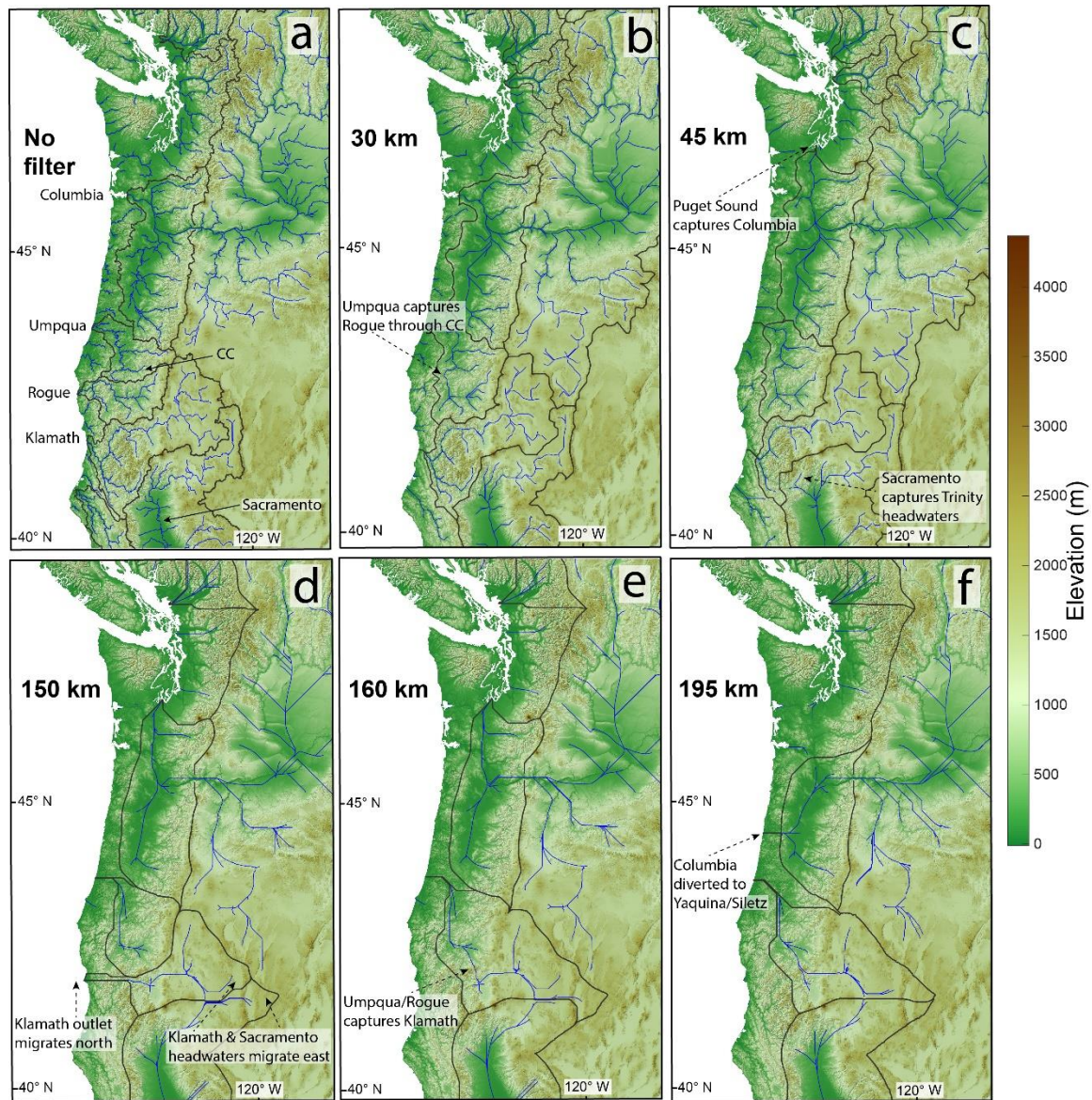


**Figure 3. Synthetic drainage networks.** Actual (a) and synthetic drainage networks corresponding to b) 30, c) 45, d) 150, e) 160, and f) 195 km wavelengths. Blue lines are synthetic drainage networks, and gray lines are synthetic drainage divides corresponding to major forearc drainage basins. Each panel highlights discrete changes to drainage basin extent, defined by drops in JSI (Figure 4). See text for description of each major change. For visual clarity, mapped topography in all panels is unfiltered (Figure S4 for filtered). Linear channels correspond with filled sinks (prevalent in the upper Columbia Basin). These sinks do not affect our results in the forearc. We plot the drainage divide at the crest of the Cascades for Willamette-draining channels (i.e. no upper Columbia). Basin and Range rivers omitted. CC: Cow Creek.

River (Figure S2). Synthetic capture of Cow Creek by the Rogue River is partially explained by the lack of adjustment of Cow Creek to baselevel lowering imposed by the Umpqua basin – knickpoints resulting from recent capture from the Coquille River have yet to migrate to the low-relief headwaters captured by the synthetic Rogue River (Figure S2). This low-relief reach of Cow Creek appears in filtered topography as a broad, poorly integrated surface primed for capture. At a wavelength of 30 km, however, the polarity of synthetic divide migration reverses, and the synthetic Umpqua River captures the Rogue River *through* Cow Creek (Figures 3 and S1), resulting in an abrupt drop in JSI for both the Rogue and Umpqua Rivers (Figure 4). Synthetic capture of the Rogue River by the Umpqua River reflects progressive and continuing growth of the Umpqua drainage basin and suggests that faster uplift in the southern OCR and Klamath Mountains may drive the Rogue River to seek a new route to baselevel (Balco et al., 2013; Bodmer et al., 2019; von Dassow, 2018; Kelsey et al., 1994).

In the Klamath River catchment, we observe multiple abrupt drops in JSI superimposed on a gradual overall decrease (Figure 4). Abrupt drops in JSI at wavelengths <160 km correspond to synthetic drainage basin augmentation in the Klamath River headwaters in the Basin and Range Province and High Lava Plains east of the Cascades and loss of southern tributaries in the Klamath Mountains. The main stem of the Klamath River has kept pace with high uplift rates in the Klamath Mountains, as indicated by its well-entrenched valley system through the range. Entrenchment of the Klamath River is reflected by the remarkable stability of the main stem of the river through a wide range of wavelengths, although the synthetic outlet of the river migrates

101
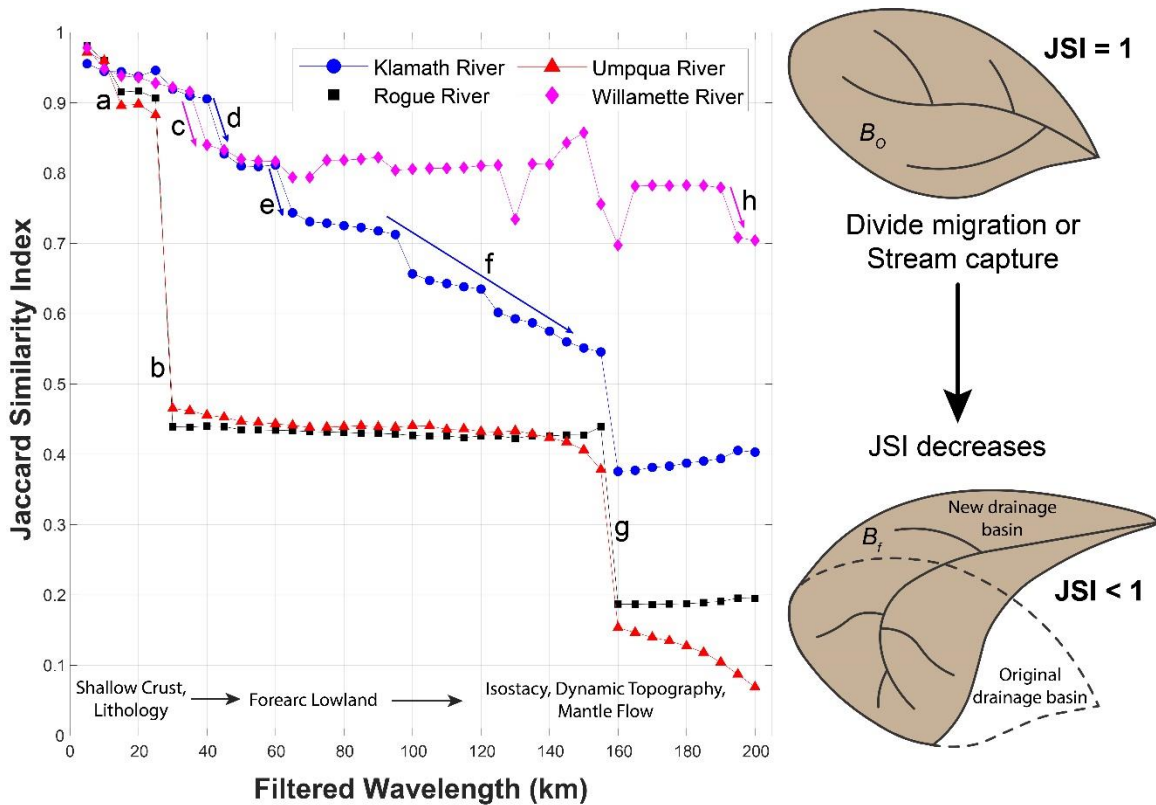
**Figure 4. Jaccard Similarity Index (JSI) quantifies scale-dependence of drainage basins.** High JSI indicates little change between synthetic and unfiltered catchments. Low JSI indicates greater change due to mobile divides and captures. Drops in JSI include: **a)** 15 km wavelength: Synthetic capture of Cow Creek from Umpqua River by Rogue River. **b)** 30 km: Umpqua River captures the Rogue River through Cow Creek, indicating reverse in capture direction. **c)** 40 km: Willamette River diverted into Puget Sound. **d)** 45 km: Sacramento River captures headwaters of the Trinity River (Klamath River tributary). **e)** 65 km: trunk channel of Trinity River drains directly to sea level. **f)** ~90-155 km: Klamath River outlet migrates northward. **(g)** 160 km: Klamath River diverted into merged Umpqua/Rogue system. **h)** 190 km: Willamette River diverted across Marys/Yaquina drainage divide. Oscillation in JSI for Willamette River between 130-160 km due to Columbia River outlet alternating between Chehalis River and Puget Sound. Oscillation an artifact introduced from Pleistocene glaciation due to clipping outlets at sea-level.

northward at longer (100-155 km) wavelengths (Figures 3 and 4). At a wavelength of 160 km, the synthetic Klamath River is diverted northward into the merged Umpqua-Rogue system (Figures 3 and 4). In addition, southern tributaries of the Klamath River, including the Trinity River, which may be experiencing higher uplift as the Mendocino Triple

Junction passes (Balco et al., 2013; Bodmer et al., 2019; Furlong and Govers, 1999; Kelsey et al., 1994; Lock et al., 2018), are diverted at moderate wavelengths (40-45 km; Figures 3 and 4).

The Willamette River experiences the smallest overall decrease in JSI (Figure 4), reflecting concordance between the modern WV and the Cascadia Forearc Lowland that we observe in wavelet-transformed topography (Figures 1 and 2). Regions of simulated divide migration and stream capture support geologic evidence for progressive growth and southward migration of the WV that accentuates the forearc lowland (Figures 3 and S1). Between 40 and 45 km wavelengths, the Columbia River is diverted into the Puget Lowland over the low divide between the Chehalis and Cowlitz Rivers, which is composed of glacial outwash that has inundated the forearc (Figure 3). Despite the significant depth of structural basins in the Puget Lowland (e.g. Ramachandran et al., 2006), the role of tectonics and basin subsidence in driving this capture event may be somewhat modulated by Plio-Pleistocene glaciation in the Puget Lowland, though Columbia River sediments have been mapped at the mouth of the Chehalis River (Walsh et al., 1987). Other regions of simulated transience and capture in the northern WV are concentrated along drainage divides with the Nehalem and Nestucca Rivers and are supported by paleoroutes of the Columbia River (Figure S1), indicated by emplacement patterns of the Columbia River Basalts (Beeson et al., 1989; Reidel and Tolan, 2013). In the southwestern WV, we observe mobility of simulated drainage divides with west-draining OCR rivers (Figure S1), where multiple discrete captures along the divides with the Siuslaw, Alsea, Yaquina, and Siletz Rivers have been observed (Figure 1; Baldwin

and Howell, 1949; Chylek, 2002; Moeller, 1990; Niem, 1976). Given these captures have already occurred, offset between the synthetic and modern divides is minimal.

## 4. Discussion and Conclusions

Application of 2D CWTs and Gaussian filters to topography informs the scale and distribution of catchment-defining landforms, which then dictate drainage divide migration over a broad suite of wavelengths. Notably, in Ricker wavelet-transformed topography, the concave Cascadia Forearc Lowland exhibits some connectivity at wavelengths >30 km (Figure 2A-C), and it clearly extends along the entire subduction zone at wavelengths >100 km (Figure 2D-F). In turn, synthetic drainage networks mapped on Gaussian filtered topography illuminate the scale dependency of drainage basins in the Cascadia forearc (Figure 4) and highlight the influence of hillslope-valley coupling, lithology, and shallow crustal faults at short wavelengths (<30 km), regional tectonic deformation at intermediate wavelengths (30-160 km), and lithospheric mechanics or mantle processes at long wavelengths (160-200 km).

The locations of simulated capture points identified in our analysis coincide with independent geologic evidence for shifting drainages, allowing us to hindcast past captures and predict future captures of coast-draining rivers in southern Cascadia. When coupled with field observations of stream capture and growth of margin-parallel rivers in the forearc (Figures 3, S2, and S3; Baldwin and Howell, 1949; Chylek, 2002; Moeller, 1990; Niem, 1976), the simulated diversion of arc-to-coast rivers at wavelengths >30 km suggests that Gaussian filtered topography is an effective predictor of future divide transience and stream capture between major river catchments. Geologic variability in lithology and structure modulate and control drainage basin morphology and contribute

104

to drainage reorganization on short temporal and spatial scales (Forte et al., 2016; Gallen, 2018), including intra-catchment reorganization. Nonetheless, long-wavelength topography better predicts future drainage configurations (Campbell, 1896; Moodie et al., 2018; Wegmann et al., 2007), as it is more persistent than transitory lithologic and structural heterogeneities. Persistence of long-wavelength topographic divides provides a prolonged, exogenic boundary condition that directs the flow of rivers and alters the geometry of drainage networks (Faccenna et al., 2019; Moodie et al., 2018).

Our results suggest that southern Cascadia arc-to-coast draining rivers (Umpqua, Rogue, Klamath) are evolving into a configuration more evocative of the WV. Observed WV captures and predicted future growth of margin-parallel rivers is likely a result of differential uplift along the margin, continued OCR uplift that outpaces river incision, and/or active subsidence within the forearc topographic low, though the relative importance of these options is unclear. We suggest, however, that observed growth of the WV in concert with the formation of structural basins (e.g. Blakely et al., 2000; McPhee et al., 2014) implicates crustal subsidence as an important boundary condition for setting drainage network geometry and driving forearc drainage reorganization. The spatial variability in uplift rates that would be implied by the transition of the Cascadia forearc to a margin-parallel river system may be due to recent reorganization of oceanic plates and subduction (Bassett and Watts, 2015; Bodmer et al., 2015; Calvert et al., 2011; Hawley and Allen, 2019); mantle wedge serpentinization, corner flow, and high rates of slab sinking driving forearc subsidence and/or OCR uplift (Audet et al., 2010; Becker et al., 2014; Blakely et al., 2005; Brocher et al., 2003; Delph et al., 2018; Hyndman and Peacock, 2003; Johnson and Tebo, 2018; Ramachandran et al., 2006); clockwise rotation

and crustal faulting of the forearc forcing basin formation (Blakely et al., 2000; Wells et al., 1998, 2017; Wells and McCaffrey, 2013); or some combination thereof. Isolating the effect of these mechanisms on topography, while beyond the scope of this work, will elucidate the role of variable-scale tectonic processes on setting drainage basin morphology as well as clarify active processes driving relief formation in forearcs.

Utilization of 2D CWTs and Gaussian filters represents a promising paradigm for interpreting drainage network disequilibrium and predicting future pathways of reorganization as well as investigating the characteristic wavelength of tectonic and surface processes that define and dictate river network extent and morphology. Wavelet- and Gaussian-transformed topography may be exploited to inform fish genetics and paleogeographic reconstructions, sediment provenance, and landscape evolution models and may provide linkages between surface processes and mantle and crustal dynamics measured using seismic tomography and geodesy. Finally, future studies are needed to address how river discharge and sediment supply interact with variable-wavelength topography and whether Gaussian filtered synthetic drainage networks correspond with specific timescales of landscape transience and adjustment.

## CHAPTER III SUPPLEMENTARY MATERIAL

| ID* | Site Name | Type | Geology | Slope | Fail Depth (m) | Area (m$^2$) | Volume (m$^3$; Larsen et al., 2010) | Volume (m$^3$; depth*area) | Valley Width (m) |
|---|---|---|---|---|---|---|---|---|---|
| 1 | Beaver Dam | C | Tidb/Ty | 12 | 10.4 | 13469703 | 457404527.4 | 140084911.2 | 52.4 |
| 2 | Burchard | EF | Tte | 15 | 5.9 | 872576 | 11943949.5 | 5148198.4 | 52.3 |
| 3 | Buttermilk | EF | Tt | 22 | 25.5 | 2227593 | 41621139.8 | 56803621.5 | 48.4 |
| 4 | Carlton | EF | Tidb/Ty | 20 | 38.7 | 1708594 | 29233016.4 | 66122587.8 | 56.1 |
| 5 | Esmond | RS-R | Tt | 30 | 26.4 | 3739156 | 82972072.7 | 98713718.4 | 44.3 |
| 6 | Hamar | EF | Tt | 27 | 27.2 | 4057977 | 92526458.3 | 110376974.4 | 113.0 |
| 7 | Hanna | EF | Ty/Tidb | 22 | 41.0 | 2624851 | 51789888.6 | 107618891 | 16.8 |
| 8 | Hemlock | RS-R | Tbl | 22 | 7.0 | 778392 | 10258266.8 | 5448744 | 19.8 |
| 9 | Kauppi | RS-R | Tk | 17 | 7.3 | 1843269 | 32341588.7 | 13455863.7 | 69.9 |
| 11 | Little Lobster | RS-R + EF | Tt | 35 | 24.4 | 1537172 | 25392974.2 | 37506996.8 | 79.1 |
| 12 | Murphy | C | Tbl/Ty | 22 | 11.3 | 2316532 | 43849194.9 | 26176811.6 | 52.3 |
| 13 | Parsons | EF | Ty/Tidb | 10 | 29.0 | 3634365 | 79889265.8 | 105396585 | 75.3 |
| 14 | Pearl | RS-T | Tt | 27 | 20.4 | 374047 | 3864880.9 | 7630558.8 | 50.1 |
| 15 | Scoggins Valley | RS-R | Tidb | 20 | 7.2 | 749074 | 9746857.5 | 5393332.8 | 20.6 |
| 16 | Soup | RS-R | Tte | 25 | 29.0 | 5501067 | 138762951.6 | 159530943 | 15.2 |
| 17 | Spruce Run | RS-R | Tk | 32 | 16.8 | 562185 | 6650236.8 | 9444708 | 25.2 |
| 18 | Sunago | EF | Tc | 17 | 7.9 | 906167 | 12560284.1 | 7158719.3 | 46.7 |
| 19 | Yellow | RS-R | Tt | 25 | 12.4 | 112542 | 16705859.8 | 1395520.8 | 46.6 |
| K | Klickitat | C | Tt | 32 | 25.9 | 1216903 | 18601994.6 | 31517787.7 | 87.4 |
|  | LP** | EF | Tt | 22 | 18.4 | 1871517 | 33003496.0 | 34435912.8 | 29.8 |
| A | Ayers | C-ES-R+EF | Tt | 21 | 47.0 | 1442290 | 23326739.6 | 67787630 | 54.1 |
| G | Gould | RS-R | Tt | 30 | 33.0 | 703204 | 8960055.3 | 23205732 | 27.3 |
| W | Wasson | EF | Tt | 25 | 12.4 | 273344 | 2545054.6 | 3389465.6 | 41.2 |

**Table S1. Landslide Deposit Measurements.**

* Label in Figure 1

**: LP: Little Paradise, not dated. Visited in the field and verified as active impoundment (43.689 N, -123.568 W).
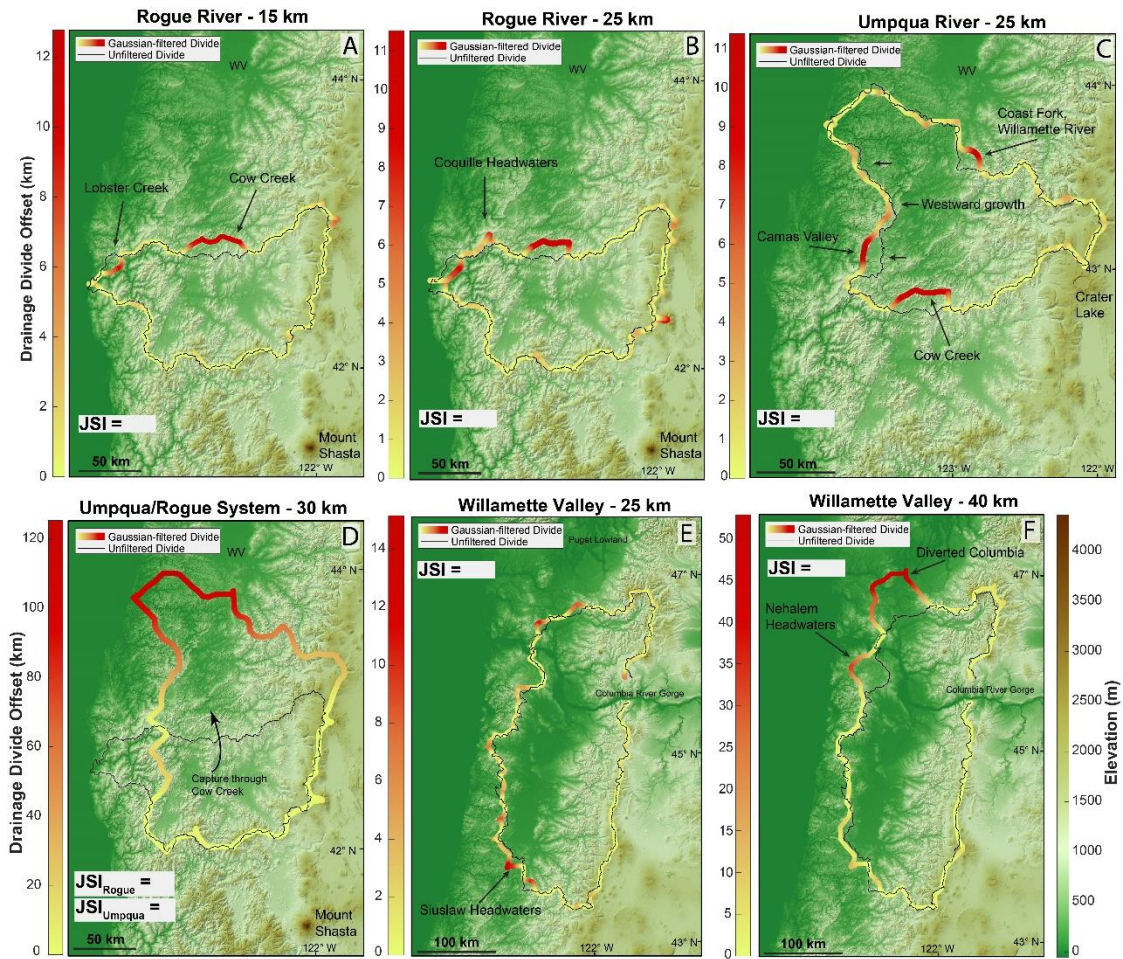
Landslide type labeled as: C: Complex; EF: Earth Flow; ES: Earth Slide; R: Rotational; RS: Rock Slide; T: Translational.

Lithology denoted as: Tc: Columbia River Basalt Group; Tbl: Tillamook Volcanics; Tidb: Depot Bay Basalt; Tk: Keasey Formation; Tt: Tyee Formation; Tte: Elkton Member Tyee Formation; Ty: Yamhill Formation (Walker & Macleod, 1991).

## CHAPTER IV SUPPLEMENTARY MATERIAL



**Figure S1.** Gaussian-filtered catchments. Synthetic and actual drainage divides plotted on unfiltered DEM. Each panel labeled by its respective drainage basin, filtered wavelength, and JSI value. Synthetic divides colored by offset distance from the actual drainage divide (black lines). **a-b**) Synthetic Rogue River at wavelengths of 15 and 25 km. Note offset synthetic divides at Cow Creek (stolen from Umpqua River), Lobster Creek (near Rogue River outlet), and the Coquille Headwaters. **c**) Synthetic Umpqua drainage basin at wavelength of 25 km. Offset synthetic divides concentrate at high elevation, low-relief regions such as Cow Creek (lost to Rogue River), Camas Valley (stolen from Coos River), and the headwaters of the Coast Fork Willamette River (Figure S3). Note westward migration of synthetic divides on eastern slope of the OCR, highlighting the competition between arc-to-coast and margin-parallel river systems. **d**) Merged Umpqua/Rogue River system at wavelength of 30 km. Note filtered divide colored by offset from unfiltered Rogue. **e-f**) Synthetic WV at 25 and 40 km wavelengths. Captures/diversions include: Siuslaw headwaters at 25 km; Nehalem River at 40 km; Columbia River diverted to Puget Sound at 40 km. Eastern drainage divide in Columbia River Gorge omitted. In all panels, note stability of Cascades divide, which remains a persistent topographic high through all wavelengths (Figure 2).
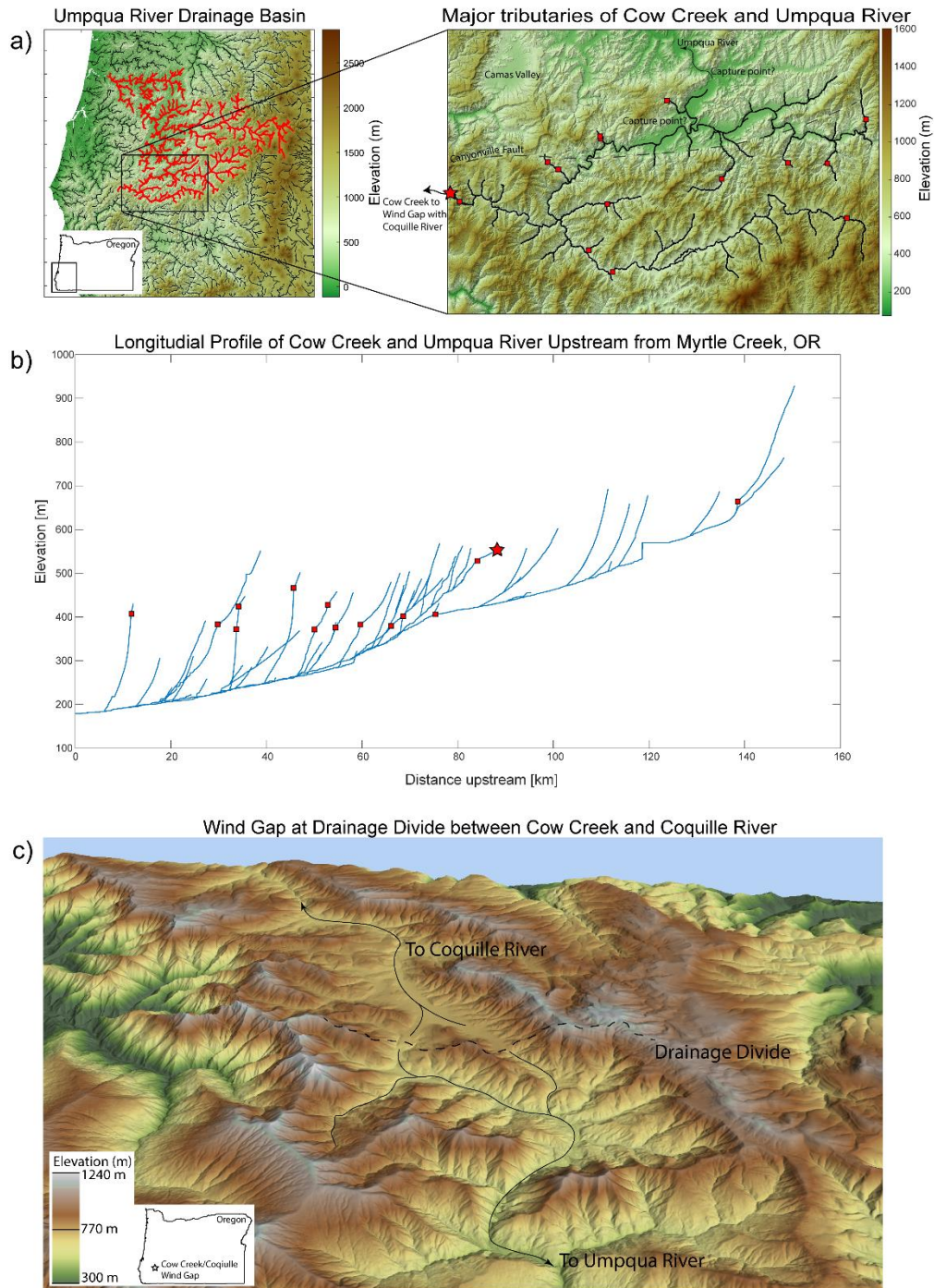
**Figure S2. Southern Umpqua drainage basin transience. a)** Umpqua River (red). Right panel is Umpqua River and Cow Creek (CC) upstream Myrtle Creek, Oregon. Prominent knickpoints denoted by red squares. Two possible capture locations labeled. West fork of Cow Creek continues to wind gap with the Coquille River (red star). Canyonville Fault (dashed). **b)** Longitudinal profile of Umpqua River and CC upstream of Myrtle Creek. Knickpoint at elevation of ~380 m due to capture of CC from Coquille River by the Umpqua River. Knickpoints due to dams (sharp steps) or lithologic contrasts are removed. **c)** Wind gap and barbed tributaries at Cow Creek drainage divide (dashed).
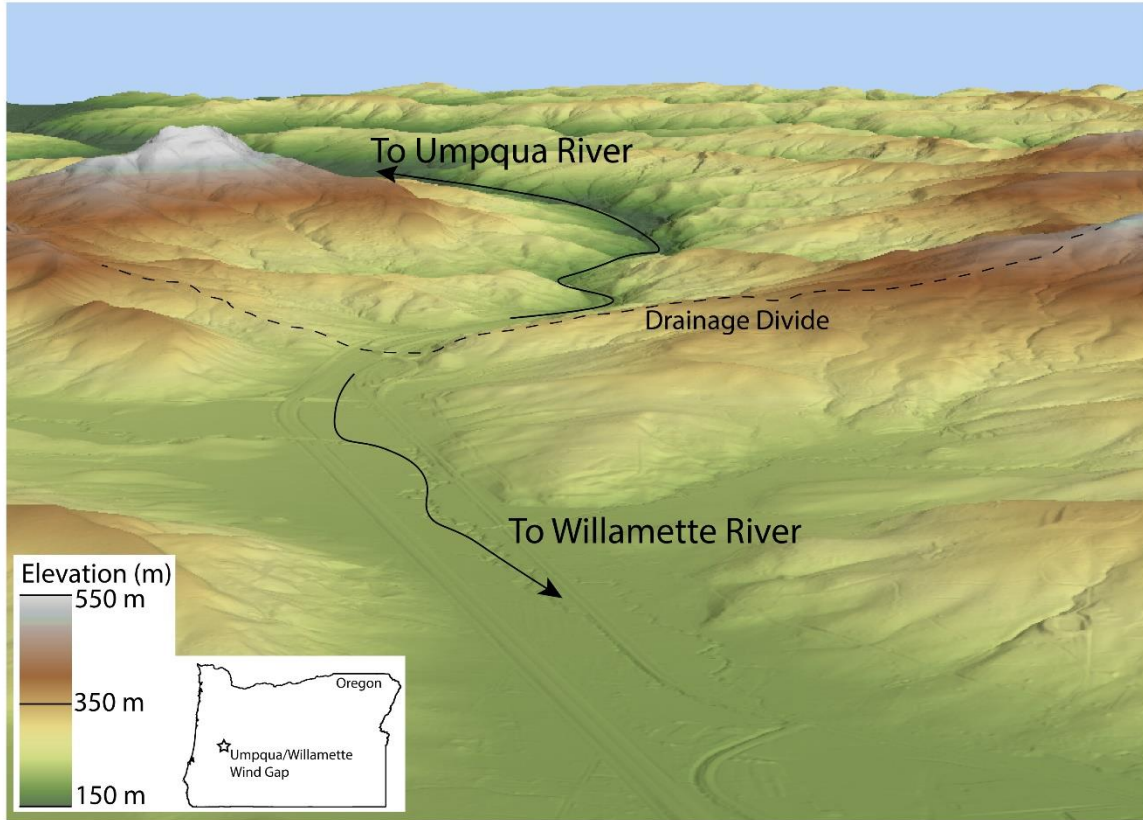
**Figure S3.** The drainage divide between the Umpqua River and Willamette River exhibits a major wind gap south of Eugene, Oregon. Steep, primarily bedrock Umpqua-draining channels contrast strongly with the broad and alluviated valleys of the southern Willamette Valley, suggesting that the Umpqua River is growing at the expense of the southern Willamette Valley.
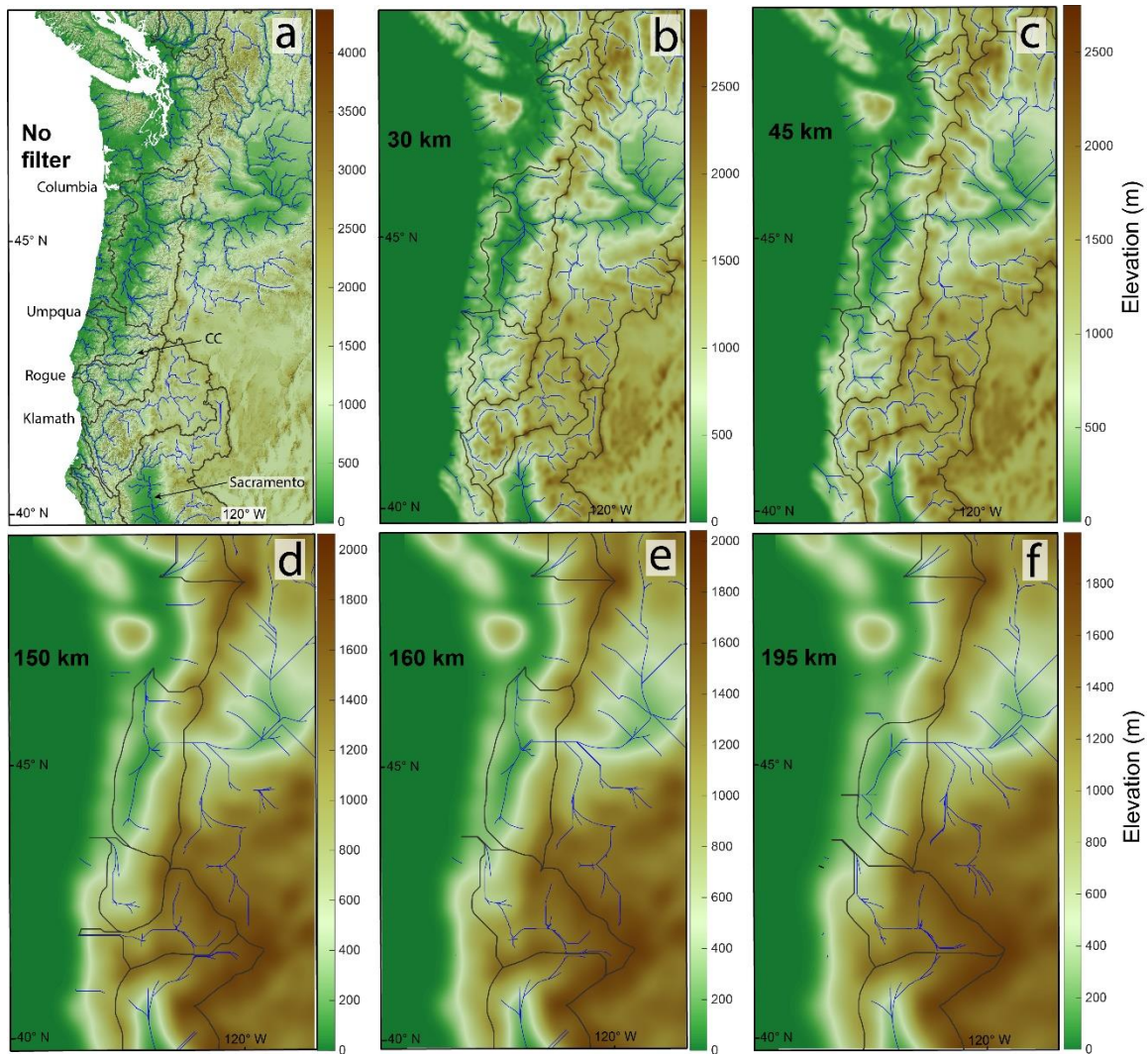
**Figure S4:** Synthetic drainage networks and drainage divides mapped on Gaussian-filtered topography corresponding to wavelengths of b) 30 km, c) 45 km, d) 150 km, e) 160 km, and f) 195 km (topography in a) is unfiltered). Note that the Willamette Valley drainage basin is clipped at the crest of the Cascades (the through-flowing Columbia is included purely for illustration of the synthetic drainage network). See Figure 3 for description of divide migration and stream capture in the synthetic drainage network. Note that elevations of colorbar change as filter wavelength increases. In addition, note that *only divides* are used in comparison of drainage basins using the Jaccard Similarity Index; drainage networks included solely for illustration.

# REFERENCES CITED

**Chapter I**
Black, B.A., Perron, J.T., Hemingway, D., Bailey, E., Nimmo, F., & Zebker, H., (2017). Global drainage patterns and the origins of topography relief on Earth, Mars, and Titan: Science, v. 356, p. 727-731, doi:10.1126/science.aag0171.

**Chapter II**
Allstadt, K., Vidale, J.E., & Frankel, A.D., (2013). A scenario study of seismically induced landsliding in Seattle using broadband synthetic seismograms: Bulletin of the Seismological Society of America, v. 103, p. 2971–2992, doi:10.1785/0120130051.

Almond, P., Roering, J., & Hales, T.C., (2007). Using soil residence time to delineate spatial and temporal patterns of transient landscape response: Journal of Geophysical Research–Earth Surface, v. 112, F03S17, doi:10.1029/2006JF000568.

Atwater, B.F., & Yamaguchi, D.K., (1991). Sudden, probably coseismic submergence of Holocene trees and grass in coastal Washington State: Geology, v. 19, p. 706-709, doi:10.1130/0091-7613(1991)019.

Atwater, B.F., Satoko, M.-R., Kenji, S., Yoshinobu, T., Kazue, U., & Yamaguchi, D.K., (2005). The Orphan Tsunami of 1700: Japanese Clues to a Parent Earthquake in North America: U.S. Geological Society Professional Paper 1707, 135 p.

Balco, G., Finnegan, N., Gendaszek, A., Stone, J.O., & Thompson, N., (2013). Erosional response to northward-propagating crustal thickening in the coastal ranges of the US Pacific Northwest: American Journal of Science, v. 313, p. 790–806, doi:10.2475/11.2013.01.

Baldwin, E.M., (1956). Geologic Map of the Lower Siuslaw River Area, Oregon: U.S. Geological Survey Oil and Gas Investigation Map 186, scale 1:62,500, 1 sheet.

Ballantyne, C.K., & Stone, J.O., (2004). The Beinn Alligin rock avalanche, NW Scotland: Cosmogenic 10Be dating, interpretation and significance: The Holocene, v. 14, p. 448–453, doi:10.1191/0959683604hl720rr.

Bégin, C., & Filion, L., (1988). Age of landslides along Grande Riviére de la Baleine estuary, eastern coast of Husdon Bay, Quebec (Canada): Boreas, v. 17, p. 289-299, doi:10.1111/j.1502-3885.1988.tb00959.x.

Bekker, M.F., Metcalf, D.P., & Harley, G.L., (2018). Hydrology and hillslope processes explain spatial variation in tree-ring responses to the 1983 earthquake at Borah Peak, Idaho, USA: Earth Surface Processes and Landforms, v. 43, no. 15, p. 3074–3085, doi:10.1002/esp.4470.

Benda, L., (1990). The influence of debris flows on channels and valley floors in the Oregon Coast Range, USA: Earth Surface Processes and Landforms, v. 15, p. 457–466, doi:10.1002/esp.3290150508.

Benda, L., & Dunne, T., (1997). Stochastic forcing of sediment supply to channel networks from landsliding and debris flow: Water Resources Research, v. 33, p. 2849–2863, doi:10.1029/97WR02388.

Beschta, R.L., (1978). Long-term patterns of sediment production following road construction and logging in the Oregon Coast Range: Water Resources Research, v. 14, p. 1011–1016, doi:10.1029/WR014i006p01011.

Bierman, P., Clapp, E., Nichols, K., Gillespie, A., & Caffee, M.W., (2001). Using cosmogenic nuclide measurements in sediments to understand background rates of erosion and sediment transport, *in* Harmon, R.S., and Doe, W.W., eds., Landscape Erosion and Evolution Modeling: Boston, Massachusetts, Springer, p. 89–115, doi:10.1007/978-1-4615-0575-4_5.

Black, B.A., Dunham, J.B., Blundon, B.W., Brim-Box, J., & Tepley, A.J., (2015). Long term growth-increment chronologies reveal diverse influences of climate forcing on freshwater and forest biota in the Pacific Northwest: Global Change Biology, v. 21, p. 594–604, doi:10.1111/gcb.12756.

Blakely, R.J., Wells, R.E., Tolan, T.L., Beeson, M.H., Trehu, A.M., & Liberty, L.M., (2000). New aeromagnetic data reveal large strike-slip (?) faults in the northern Willamette Valley, Oregon: Geological Society of America Bulletin, v. 112, p. 1225–1233, doi:10.1130/0016-7606(2000)112.

Booth, A.M., Roering, J.J., & Perron, J.T., (2009). Automated landslide mapping using spectral analysis and high-resolution topographic data: Puget Sound lowlands, Washington, and Portland Hills, Oregon: Geomorphology, v. 109, p. 132–147, doi:10.1016/j.geomorph.2009.02.027.

Booth, A.M., LaHusen, S.R., Duvall, A.R., & Montgomery, D.R., (2017). Holocene history of deep-seated landsliding in the North Fork Stillaguamish River valley from surface roughness analysis, radiocarbon dating, and numerical landscape evolution modeling: Journal of Geophysical Research: Earth Surface, v. 122, p. 456–472, doi:10.1002/2016JF003934.

Booth, A.M., McCarley, J., Hinkle, J., Shaw, S., Ampuero, J.-P., & Lamb, M.P., (2018). Transient reactivation of a deep-seated landslide by undrained loading captured with repeat airborne and terrestrial LiDAR: Geophysical Research Letters, v. 45, p. 4841–4850, doi:10.1029/2018GL077812.

Braitseva, O.A., Sulerzhitsky, L.D., Litasova, S.N., Melekestsev, I.V., & Ponomareva, V.V., (1993). Radiocarbon dating and tephrochronology in Kamchatka: Radiocarbon, v. 35, p. 463–476, doi:10.1017/S00338222000060495.

Bronk Ramsey, C., (1995). Radiocarbon calibration and analysis of stratigraphy: The OxCal Program: Radiocarbon, v. 37, p. 425–430, doi:10.1017/S0033822200030903.

Bronk Ramsey, C., (2009). Bayesian analysis of radiocarbon dates: Radiocarbon, v. 51, p. 337–360, doi:10.1017/S0033822200033865.

Bronk Ramsey, C., (2017). Methods for summarizing radiocarbon datasets: Radiocarbon, v. 59, p. 1809–1833, doi:10.1017/RDC.2017.108.

Brown, G.W., & Krygier, J.T., (1971). Clear-cut logging and sediment production in the Oregon Coast Range: Water Resources Research, v. 7, p. 1189–1198, doi:10.1029/WR007i005p01189.

Burns, W.J., & Madin, I.P., (2009). Protocol for Inventory Mapping of Landslide Deposits from Light Detection and Ranging (LiDAR) Imagery: Oregon Department of Geology and Mineral Industries Special Paper 42, 30 p.

Burns, W.J., & Watzig, R., (2014). Statewide Landslide Information Database of Oregon Release-3.0: Oregon Department of Geology and Mineral Industries SLIDO-3.0, 35 p.

Burns, W.J., Duplantis, S., Jones, C.B., & English, J.T., (2012). LiDAR Data and Landslide Inventory Maps of the North Fork Siuslaw River and Big Elk Creek Watersheds, Lane, Lincoln, and Benton Counties: Portland, Oregon, Oregon Department of Geology and Mineral Industries Open File Report O-12-07, 15 p.

Butterfield, N.J., Bunds, M.P., Zanazzi, A., & Toke, N.A., (2015). A preliminary look at geomorphic impacts and timing of two large, drainage-damming landslides in the central Wasatch: Geological Society of America Abstracts with Programs, v. 47, no. 7, p. 523.

Cerovski-Darriau, C., Roering, J.J., Marden, M., Palmer, A.S., & Bilderback, E.L., (2014). Quantifying temporal variations in landslide-driven sediment production by reconstructing paleolandscapes using tephrochronology and LiDAR: Waipaoa River, New Zealand: Geochemistry Geophysics Geosystems, v. 15, p. 4117–4136, doi:10.1002/2014GC005467.

Clague, J.J., (2015). Paleolandslides, *in* Shroder, J.F., and Davies, T., eds., Landslide Hazards, Risks and Disasters: Amsterdam, Netherlands, Elsevier, p. 321–344, doi:10.1016/C2011-0-07015-1.

Cruden, D.M., & Varnes, D.J., (1996). Landslide types and processes, *in* Turner, A.K., and Schuster, R.L., eds., Landslides-Investigation and Mitigation: Transportation Research Board of the National Academy of Sciences Special Report 247, p. 36-75.

Dadson, S.J., Hovius, N., Chen, H., Dade, W.B., Lin, J.-C., Hsu, M.-L., Lin, C.-W., et al., (2004). Earthquake-triggered increase in sediment delivery from an active mountain belt: Geology, v. 32, p. 733–736, doi:10.1130/G20639.1.

Danišík, M., Shane, P., Schmitt, A.K., Hogg, A., Santos, G.M., Storm, S., Evans, N.J., et al., (2012). Re-anchoring the late Pleistocene tephrochronology of New Zealand based on concordant radiocarbon ages and combined 238U/230Th disequilibrium and (U-Th)/He zircon ages: Earth and Planetary Science Letters, v. 349–350, p. 240–250, doi:10.1016/j.epsl.2012.06.041.

Densmore, A.L., & Hovius, N., (2000). Topographic fingerprints of bedrock landslides: Geology, v. 28, p. 371–374, doi:10.1130/0091-7613(2000)28.

Dietrich, W.E., & Dunne, T., (1978). Sediment budget for a small catchment in mountainous terrain: Zeitschrift für Geomorphologie N.F., v. 29, p. 191–206.

Douglass, A.E., (1941). Crossdating in dendrochronology: Journal of Forestry, v. 39, p.825–831, doi:10.1093/jof/39.10.825.

Dumitru, T.A., Ernst, W.G., Wright, J.E., Wooden, J.L., Wells, R.E., Farmer, L.P., et al., (2013). Eocene extension in Idaho generated massive sediment floods into the Franciscan trench and into the Tyee, Great Valley, and Green River basins: Geology, v. 41, p. 187–190, doi:10.1130/G33746.1.

Fantucci, R., & McCord, A., (1995). Reconstruction of landslide dynamics with dendrochronological methods: Dendrochronologia, v. 13, p. 43–58.

Filion, L., Quinty, F., & Bégin, C., (1991). A chronology of landslide activity in the valley of Riviére du Gouffre, Charlevoix, Quebec: Canadian Journal of Earth Sciences, v. 28, p. 250–256, doi:10.1139/e91-024.

Frankel, A., Wirth, E., Marafi, N., Vidale, J., & Stephenson, W., (2018). Broadband synthetic seismograms for magnitude 9 earthquakes on the Cascadia megathrust based on 3D simulations and stochastic synthetics: Part 1. Methodology and overall results: Bulletin of the Seismological Society of America, v. 108, p. 2347-2369, doi:10.1785/0120180034.

Gadgil, P.D., (1971). Effect of waterlogging on mycorrhizas of radiata pine and Douglas fir: New Zealand Journal of Forestry Science, v. 2, p. 5.

Gallen, S.F., Clark, M.K., Godt, J.W., Roback, K., & Niemi, N.A., (2016). Application and evaluation of a rapid response earthquake-triggered landslide model to the 25 April 2015 Mw 7.8 Gorkha earthquake, Nepal: Tectonophysics, v. 714–715, p. 173–187, doi:10.1016/j.tecto.2016.10.031.

Gavin, D.G., (2001). Estimation of inbuilt age in radiocarbon ages of soil charcoal for fire history studies: Radiocarbon, v. 43, p. 27–44, doi:10.1017/S003382220003160X.

Gavin, D.G., (2003). Forest soil disturbance intervals inferred from soil charcoal radiocarbon dates: Canadian Journal of Forest Research, v. 33, p. 2514–2518, doi:10.1139/x03-185.

Goldfinger, C., Nelson, C.H., Morey, A.E., Johnson, J.E., Patton, J.R., Karabanov, E., Gutierrez-Pastor, et al., (2012). Turbidite Event History: Methods and Implications for Holocene Paleoseismicity of the Cascadia Subduction Zone: U.S. Geological Survey Professional Paper 1661, 170 p., doi:10.3133/pp1661F.

Gorum, T., Korup, O., van Westen, C.J., van der Meijde, M., Xu, C., & van der Meer, F.D., (2014). Why so few? Landslides triggered by the 2002 Denali earthquake, Alaska: Quaternary Science Reviews, v. 95, p. 80–94, doi:10.1016/j.quascirev.2014.04.032.

Heimsath, A.M., Dietrich, W.E., Nishiizumi, K., & Finkel, R.C., (2001). Stochastic processes of soil production and transport: Erosion rates, topographic variation and cosmogenic nuclides in the Oregon Coast Range: Earth Surface Processes and Landforms, v. 26, p. 531–552, doi:10.1002/esp.209.

Heller, P.L., & Dickinson, W.R., (1985). Submarine ramp facies model for delta-fed, sand-rich turbidite systems: American Association of Petroleum Geologists Bulletin, v. 69, no. 6, p. 960–976, doi:10.1306/AD462B37-16F7-11D7-8645000102C1865D.

Heller, P.L., & Ryberg, P.T., (1983). Sedimentary record of subduction to forearc transition in the rotated Eocene basin of western Oregon: Geology, v. 11, p. 380 383, doi:10.1130/0091-7613(1983)11<380:SROSTF>2.0.CO;2.

Heller, P.L., Peterman, Z.E., O'Neil, J.R., & Shafiqullah, M., (1985). Isotopic provenance of sandstones from the Eocene Tyee Formation, Oregon Coast Range: Geological Society of America Bulletin, v. 96, p. 770–780, doi:10.1130/0016-7606(1985)96<770:IPOSFT>2.0.CO;2.

Hovius, N., Meunier, P., Lin, C.-W., Chen, H., Chen, Y.-G., Dadson, S., Horng, M.-J., & Lines, M., (2011). Prolonged seismically induced erosion and the mass balance of a large earthquake: Earth and Planetary Science Letters, v. 304, p. 347–355, doi:10.1016/j.epsl.2011.02.005.

Ivy-Ochs, S., Poschinger, A.v., Synal, H.-A., & Maisch, M., (2009). Surface exposure dating of the Flims landslide, Graubünden, Switzerland: Geomorphology, v. 103, p. 104–112, doi:10.1016/j.geomorph.2007.10.024.

Jibson, R.W., Harp, E.L., & Michael, J.A., (2000). A method for producing digital probabilistic seismic landslide hazard maps: Engineering Geology, v. 58, p. 271-289, doi:10.1016/S0013-7952(00)00039-9.

Jibson, R., Allstadt, K., Rengers, F., & Godt, J., (2018). Overview of the Geologic Effects of the November 14, 2016, Mw 7.8 Kaikoura, New Zealand, Earthquake: U.S. Geological Survey Scientific Investigations Report 2017-5146, 39 p., doi:10.3133/sir20175146.

Kargel, J.S., Leonard, G.J., Shugar, D.H., Haritashya, U.K., Bevington, A., Fielding, E.J., Fujita, K., et al., (2016). Geomorphic and geologic controls of geohazards induced by Nepal's 2015 Gorkha earthquake: Science, v. 351, p. 8353–8353, doi:10.1126/science.aac8353.

Karlin, R.E., Holmes, M., Abella, S.E.B., & Sylwester, R., (2004). Holocene landslides and a 3500-year record of Pacific Northwest earthquakes from sediments in Lake Washington: Geological Society of America Bulletin, v. 116, p. 94–108, doi:10.1130/B25158.1.

Keefer, D.K., (1984). Landslides caused by earthquakes: Geological Society of America Bulletin, v. 95, p. 406–421, doi:10.1130/0016-7606(1984)95&amp;amp;lt;406:LCBE&amp;amp;gt;2.0.CO;2.

Keefer, D.K., (2002). Investigating landslides caused by earthquakes—A historical review: Surveys in Geophysics, v. 23, p. 473–510, doi:10.1023/A:1021274710840.

Kelsey, H.M., & Bockheim, J.G., (1994). Coastal landscape evolution as a function of eustasy and surface uplift rate, Cascadia margin, southern Oregon: Geological Society of America Bulletin, v. 106, p. 840–854, doi:10.1130/0016-7606(1994)106<0840:CLEAAF>2.3.CO;2.

Kelsey, H.M., Engebretson, D.C., Mitchell, C.E., & Ticknor, R.L., (1994). Topographic form of the Coast Ranges of the Cascadia margin in relation to coastal uplift rates and plate subduction: Journal of Geophysical Research, v. 99, p. 12245–12255, doi:10.1029/93JB03236.

Kelsey, H.M., Ticknor, R.L., Bockheim, J.G., & Mitchell, E., (1996). Quaternary upper plate deformation in coastal Oregon: Geological Society of America Bulletin, v. 108, p. 843–860, doi:10.1130/0016-7606(1996)108<0843:QUPDIC>2.3.CO;2.

LaHusen, S.R., Duvall, A.R., Booth, A.M., & Montgomery, D.R., (2016). Surface roughness dating of long-runout landslides near Oso, Washington (USA), reveals persistent postglacial hillslope instability: Geology, v. 44, p. 111–114, doi:10.1130/G37267.1.

Lang, A., Moya, J., Corominas, J., Schrott, L., & Dikau, R., (1999). Classic and new dating methods for assessing the temporal occurrence of mass movements: Geomorphology, v. 30, p. 33–52, doi:10.1016/S0169-555X(99)00043-4.

Larsen, I.J., Montgomery, D.R., & Korup, O., (2010). Landslide erosion controlled by hillslope material: Nature Geoscience, v. 3, p. 247–251, doi:10.1038/ngeo776.

Larsson, L., (2013). CooRecorder and CDendro Programs of the CooRecorder/CDendro Package, Version 9.0.

Leithold, E.L., Wegmann, K.W., Bohnenstiehl, D.R., Smith, S.G., Noren, A., & O'Grady, R., (2018). Slope failures within and upstream of Lake Quinault, Washington, as uneven responses to Holocene earthquakes along the Cascadia subduction zone: Quaternary Research, v. 89, p. 178–200, doi:10.1017/qua.2017.96.

Li, G., West, A.J., Densmore, A.L., Jin, Z., Parker, R.N., & Hilton, R.G., (2014). Seismic mountain building: Landslides associated with the 2008 Wenchuan earthquake in the context of a generalized model for earthquake volume balance: Geochemistry Geophysics Geosystems, v. 15, p. 833–844, doi:10.1002/2013GC005067.

Logan, R.L., Schuster, R.L., Pringle, P.T., Walsh, T.J., & Palmer, S.P., (1998). Radiocarbon ages of probable coseismic features from the Olympic Peninsula and Lake Sammamish: Washington: Washington Geology, v. 26, no. 2-3, p. 59–67.

Mackey, B.H., Roering, J.J., & Lamb, M.P., (2011). Landslide-dammed paleolake perturbs marine sedimentation and drives genetic change in anadromous fish: Proceedings of the National Academy of Sciences of the United States of America, v. 108, p. 18905–18909, doi:10.1073/pnas.1110445108.

Madin, I.P., & Burns, W.J., (2013). Ground Motion, Ground Deformation, Tsunami Inundation, Coseismic Subsidence, and Damage Potential Maps for the 2012 Oregon Resilience Plan for Cascadia Subduction Zone Earthquakes: Oregon Department of Geology and Mineral Industries Open-File Report O-13-06, 36 p. + 38 maps.

Marc, O., Hovius, N., & Meunier, P., (2016a). The mass balance of earthquakes and earthquake sequences: Geophysical Research Letters, v. 43, p. 3708–3716, doi:10.1002/2016GL068333.

Marc, O., Hovius, N., Meunier, P., Gorum, T., & Uchida, T., (2016b). A seismologically consistent expression for the total area and volume of earthquake-triggered landsliding: Journal of Geophysical Research–Earth Surface, v. 121, p. 640–663, doi:10.1002/2015JF003732.

Marineau, M.D., & Wright, S.A., (2017). Daily reservoir sedimentation model: Case study from the Fena Valley Reservoir, Guam: Journal of Hydrologic Engineering, v. 143, 05017003, doi:10.1061/(ASCE)HY.1943-7900.0001344.

Marshall, J.A., Roering, J.J., Bartlein, P.J., Gavin, D.G., Granger, D.E., Rempel, A.W., Praskievicz, S.J., & Hales, T.C., (2015). Frost for the trees: Did climate increase erosion in unglaciated landscapes during the late Pleistocene?: Science Advances, v. 1, e1500715.

Marshall, J.A., Roering, J.J., Gavin, D.G., & Granger, D.E., (2017). Late Quaternary climatic controls on erosion rates and geomorphic processes in western Oregon, USA: Geological Society of America Bulletin, v. 129, p. 715–731, doi:10.1130/B31509.1.

Massey, C., Townsend, D., Rathje, E., Allstadt, K.E., Lukovic, B., Kaneko, Y., Bradley, B., et al., (2018). Landslides triggered by the 14 November 2016 $M_w$ 7.8 Kaikōura earthquake, New Zealand: Bulletin of the Seismological Society of America, v. 108, p. 1630–1648, doi:10.1785/0120170305.

May, C., Roering, J., Eaton, L.S., & Burnett, K.M., (2013). Controls on valley width in mountainous landscapes: The role of landsliding and implications for salmonid habitat: Geology, v. 41, p. 503–506, doi:10.1130/G33979.1.

McKean, J., & Roering, J., (2004). Objective landslide detection and surface morphology mapping using high-resolution airborne laser altimetry: Geomorphology, v. 57, p. 331–351, doi:10.1016/S0169-555X(03)00164-8.

McNeill, L.C., Kulm, L.D., & Yeats, R.S., (2000). Tectonics of the Neogene Cascadia forearc basin: Investigations of a deformed late Miocene unconformity: Geological Society of America Bulletin, v. 112, p. 1209–1224, doi:10.1130/0016-7606(2000)112<1209:TOTNCF>2.0.C);2.

Meunier, P., Hovius, N., & Haines, A.J., (2007). Regional patterns of earthquake triggered landslides and their relation to ground motion: Geophysical Research Letters, v. 34, L20408, doi:10.1029/2007GL031337.

Meunier, P., Hovius, N., & Haines, J.A., (2008). Topographic site effects and the location of earthquake induced landslides: Earth and Planetary Science Letters, v. 275, p. 221–232, doi:10.1016/j.epsl.2008.07.020.

Minear, J.T., & Kondolf, G.M., (2009). Estimating reservoir sedimentation rates at large spatial and temporal scales: A case study of California: Water Resources Research, v. 45, W12502, doi:10.1029/2007WR006703.

Montgomery, D.R., (2001). Slope distributions, threshold hillslopes, and steady-state topography: American Journal of Science, v. 301, p. 432–454, doi:10.2475/ajs.301.4-5.432.

Montgomery, D.R., Schmidt, K.M., Dietrich, W.E., & Greenberg, H., (2000). Forest clearing and regional landsliding: Geology, v. 28, p. 311–314, doi:10.1130/0091-7613(2000)28<311:FCARL>>2.0.CO;2.

Morey, A.E., Goldfinger, C., Briles, C.E., Gavin, D.G., Colombaroli, D., & Kusler, J.E., (2013). Are great Cascadia earthquakes recorded in the sedimentary records from small forearc lakes?: Natural Hazards and Earth System Sciences, v. 13, p. 2441-2463, doi:10.5194/nhess-13-2441-2013.

Newmark, N.M., (1965). Effects of earthquakes on dams and embankments: Geotechnique, v. 15, p. 139–160.

Olsen, M.J., Ashford, S.A., Mahlingam, R., Sharifi-Mood, M., O'Banion, M., & Gillins, D.R., (2015). Impacts of Potential Seismic Landslides on Lifeline Corridors: Oregon Department of Transportation Research Section Final Report SPR 740: Corvallis, Oregon, Oregon State University, 238 p.

Oregon Department of Geology and Mineral Industries (DOGAMI), (2012). Central Coast LiDAR Project 2011 Airborne LiDAR Survey: Oregon Lidar Consortium, distributed by Oregon Department of Geology and Mineral Industries LiDAR Program.

Oregon Department of Geology and Mineral Industries (DOGAMI), (2015). Upper Umpqua 3DEP Airborne LiDAR Survey: Oregon LiDAR Consortium, distributed by Oregon Department of Geology and Mineral Industries LiDAR Program.

Penserini, B.D., Roering, J.J., & Streig, A., (2017). A morphologic proxy for debris flow erosion with application to the earthquake deformation cycle, Cascadia subduction zone, USA: Geomorphology, v. 282, p. 150–161, doi:10.1016/j.geomorph.2017.01.018.

Perkins, J.P., Roering, J.J., Burns, W.J., Struble, W., Black, B.A., Schmidt, K.M., Duvall, A., & Calhoun, N., (2018). Hunting for landslides from Cascadia's great earthquakes: Eos (Washington, D.C.), v. 99, doi:10.1029/2018EO103689.

Personius, S.F., (1995). Late Quaternary stream incision and uplift in the forearc of the Cascadia subduction zone, western Oregon: Journal of Geophysical Research: Solid Earth, v. 100, p. 20193–20210, doi:10.1029/95JB01684.

Pessenda, L.C.R., Gouveia, S.E.M., & Aravena, R., (2001). Radiocarbon dating of total soil organic matter and humin fraction and its comparison with 14C ages of fossil charcoal: Radiocarbon, v. 43, p. 595–601, doi:10.1017/S0033822200041242.

Pierson, T.C., (2007). Dating young geomorphic surfaces using age of colonizing Douglas fir in southwestern Washington and northwestern Oregon, USA: Earth Surface Processes and Landforms, v. 32, p. 811–831, doi:10.1002/esp.1445.

Pringle, P.T., (2014). Buried and submerged forests of Washington and Oregon: Time capsules of environmental and geologic history: Western Forester, v. 59, p. 14-15, 22.

Pringle, P.T., Schuster, R.L., & Logan, R.L., (1998). New radiocarbon ages of major landslides in the Cascade Range, Washington: Washington Geology, v. 26, no. 1, p. 31–39.

PRISM Climate Group, (2016). PRISM Climate Group: Corvallis, Oregon, Oregon State University.

Reimer, P.J., Baillie, M.G., Bard, E., Bayliss, A., Beck, J.W., Blackwell, P.G., Bronk Ramsey, C., et al., (2009). IntCal09 and Marine09 radiocarbon age calibration curves, 0–50,000 years cal BP: Radiocarbon, v. 51, p. 1111–1150, doi:10.1017/S0033822200034202.

Reimer, P.J., Baillie, M.G.L., Bard, E., Bayliss, A., Beck, J.W., Blackwell, P.G., Bronk Ramsey, C., et al., (2013). IntCal13 and Marine 13 radiocarbon age calibration curves 0–50,000 years cal BP: Radiocarbon, v. 55, p. 1869–1887, doi:10.2458/azu_js_rc.55.16947.

Reneau, S.L., & Dietrich, W.E., (1991). Erosion rates in the southern Oregon Coast Range: Evidence for an equilibrium between hillslope erosion and sediment yield: Earth Surface Processes and Landforms, v. 16, p. 307–322, doi:10.1002/esp.3290160405.

Reneau, S.L., Dietrich, W.E., Dorn, R.I., Berger, C.R., & Rubin, M., (1986). Geomorphic and paleoclimatic implications of latest Pleistocene radiocarbon dates from colluvium-mantled hollows: California Geology, v. 14, p. 655–658, doi:10.1130/0091-7613(1986)14<655:GAPIOL>2.0.CO;2.

Reynolds, N., O'Connor, J.E., Pringle, P.T., Schuster, R.L., & Bourdeau, A., (2015). Age of the Bonneville landslide and the drowned forest of the Columbia River, Washington, USA—From wiggle-match radiocarbon dating and tree ring analysis, *in* 10th Washington Hydrogeology Symposium Abstracts: p. 71.

Richardson, K.N.D., Hatten, J.A., & Wheatcroft, R.A., (2018). 1500 years of lake sedimentation due to fire, earthquakes, floods and land clearance in the Oregon Coast Range: Geomorphic sensitivity to floods during timber harvest period: Natural and anthropogenic effects on sedimentation in an Oregon lake: Earth Surface Processes and Landforms, v. 43, p. 1496–1517, doi:10.1002/esp.4335.

Roback, K., Clark, M.K., West, A.J., Zekkos, D., Li, G., Gallen, S.F., Chamlagain, D., & Godt, J.W., (2017). The size, distribution, and mobility of landslides caused by the 2015 Mw 7.8 Gorkha earthquake, Nepal: Geomorphology, v. 301, p. 121–138, doi:10.1016/j.geomorph.2017.01.030.

Robison, E.G., Mills, K., Paul, J., Dent, L., & Skaugset, A., (1999). Storm Impacts and Landslides of 1996: Oregon Department of Forestry Forest Practices Technical Final Report 4, 145 p.

Roering, J.J., Kirchner, J.W., & Dietrich, W.E., (2005). Characterizing structural and lithologic controls on deep-seated landsliding: Implications for topographic relief and landscape evolution in the Oregon Coast Range, USA: Geological Society of America Bulletin, v. 117, p. 654–668, doi:10.1130/B25567.1.

Schachtman, N.S., Roering, J.J., Marshall, J.A., Gavin, D.G., & Granger, D.E., (2019). The interplay between physical and chemical erosion over glacial-interglacial cycles: Geology, v. 47, p. 613–616, doi:10.1130/G45940.1.

Scharer, K.M., Biasi, G.P., & Weldon, R.J., (2011). A reevaluation of the Pallett Creek earthquake chronology based on new AMS radiocarbon dates, San Andreas fault, California: Journal of Geophysical Research, v. 116, B12111, doi:10.1029/2010JB008099.

Schlicker, H.G., Deacon, R.J., Olcott, G.W., & Beaulieu, J.D., (1973). Environmental Geology of Lincoln County, Oregon: Oregon Department of Geology and Mineral Industries Bulletin 81, scale 1:62,500.

Schmidt, K.M., & Montgomery, D.R., (1995). Limits to relief: Science, v. 270, p. 617-620, doi;10.1126/science.270.5236.617.

Schulz, W.H., Galloway, S.L., & Higgins, J.D., (2012). Evidence for earthquake triggering of large landslides in coastal Oregon, USA: Geomorphology, v. 141-142, p. 88–98, doi:10.1016/j.geomorph.2011.12.026.

Schuster, R.L., Logan, R.L., & Pringle, P.T., (1992). Prehistoric rock avalanches in the Olympic Mountains, Washington: Science, v. 258, p. 1620–1621, doi:10.1126/science.258.5088.1620.

Serey, A., Piñero-Feliciangeli, L., Sepúlveda, S.A., Poblete, F., Petley, D.N., & Murphy, W., (2019). Landslides induced by the 2010 Chile megathrust earthquake: A comprehensive inventory and correlations with geological and seismic factors: Landslides, v. 16, no. 6, p. 1153–1165, doi:10.1007/s10346-019-01150-6.

Stefanini, M.C., (2004). Spatio-temporal analysis of a complex landslide in the Northern Apennines (Italy) by means of dendrochronology: Geomorphology, v. 63, p. 191-202, doi:10.1016/j.geomorph.2004.04.003.

Stock, J., & Dietrich, W.E., (2003). Valley incision by debris flows: Evidence of a topographic signature: Water Resources Research, v. 39, 1089, doi:10.1029/2001WR001057.

Studhalter, R.A., (1956). Early history of crossdating: Tree-Ring Bulletin, v. 21, p. 31-35.

Suter, C., Pringle, P.T., & Schuster, R.L., (2013). New environmental and radiocarbon evidence for the ages of two Holocene landslide-dammed lakes in the southern Washington Cascade Range, USA, *in* Northwest Scientific Association 84th Annual Meeting Abstracts, p. 78–79.

Tanyaş, H., Allstadt, K.E., & van Westen, C.J., (2018). An updated method for estimating landslide-event magnitude: Earth Surface Processes and Landforms, v. 43, p. 1836–1847, doi:10.1002/esp.4359.

Tanyaş, H., van Westen, C.J., Allstadt, K.E., Anna Nowicki Jessee, M., Görüm, T., Jibson, R.W., Godt, J.W., et al., (2017). Presentation and analysis of a worldwide database of earthquake-induced landslide inventories: Journal of Geophysical Research: Earth Surface, v. 122, p. 1991–2015, doi:10.1002/2017JF004236.

Thrall, G.F., Jack, R., Johnson, J.J., & Stanley, D.A., (1980). Failure mechanisms of the Drift Creek Slide: Geological Society of America Abstracts with Programs, v. 12, no. 3, p. 156.

Trumbore, S.E., (2000). Radiocarbon geochronology, *in* Noller, J.S., Sowers, J.M., & Lettis, W.R., eds., Quaternary Geochronology: Methods and Applications: American Geophysical Union Reference Shelf 4, p. 41–60, doi:10.1029/RF004p0041.

U.S. Department of Agriculture (USDA), (2000). National Agriculture Imagery Program (NAIP) for the Farm Service Agency's (FSA): USDA and Oregon Imagery Framework Implementation Team.

Valagussa, A., Marc, O., Frattini, P., & Crosta, G.B., (2019). Seismic and geological controls on earthquake-induced landslide size: Earth and Planetary Science Letters, v. 506, p. 268–281, doi:10.1016/j.epsl.2018.11.005.

Veblen, T.T., & Ashton, D.H., (1978). Catastrophic influences on the vegetation of the Valdivian Andes, Chile: Vegetatio, v. 36, p. 149–167, doi;10.1007/BF02342598.

Wartman, J., Dunham, L., Tiwari, B., & Pradel, D., (2013). Landslides in eastern Honshu induced by the 2011 Tohoku earthquake: Bulletin of the Seismological Society of America, v. 103, p. 1503–1521, doi:10.1785/0120120128.

Wells, R.E., & Heller, P.L., (1988). The relative contribution of accretion, shear, and extension to Cenozoic tectonic rotation in the Pacific Northwest: Geological Society of America Bulletin, v. 100, p. 325–338, doi:10.1130/0016-7606(1988)100<0325:TRCOAS>2.3.CO;2.

Wells, R.E., & McCaffrey, R., (2013). Steady rotation of the Cascade arc: Geology, v. 41, p. 1027–1030, doi:10.1130/G34514.1.

Wells, R.E., Weaver, C.S., & Blakely, R.J., (1998). Fore-arc migration in Cascadia and its neotectonic significance: Geology, v. 26, p. 759–762, doi:10.1130/0091-7613(1998)026<0759:FAMICA>2.3.CO;2.

Wirth, E.A., Frankel, A.D., Marafi, N., Vidale, J.E., & Stephenson, W.J., (2018). Broadband synthetic seismograms for magnitude 9 earthquakes on the Cascadia megathrust based on 3D simulations and stochastic synthetics: Part 2. Rupture parameters and variability: Bulletin of the Seismological Society of America, v. 108, p. 2370– 2388, doi:10.1785/0120180029.

Yamaguchi, D.K., (1991). A simple method for cross-dating increment cores from living trees: Canadian Journal of Forest Research, v. 21, p. 414–416, doi:10.1139/x91-053.

Yamaguchi, D.K., Atwater, B.F., Bunker, D.E., Benson, B.E., & Reid, M.S., (1997). Tree-ring dating the 1700 Cascadia earthquake: Nature, v. 389, p. 922–923, doi:10.1038/40048.

**Chapter III**
Andree, H.J. (1910). Flood in the Willamette Valley in February and March, 1910. Monthly Weather Review 38, 474–475.

Atwater, B.F., Satoko, M.-R., Kenji, S., Yoshinobu, T., Kazue, U., & Yamaguchi, D.K. (2005). The orphan tsunami of 1700: Japanese clues to a parent earthquake in North America. USGS Professional Paper 1707.

Baillie, B.R., Garrett, L.G., & Evanson, A.W. (2008). Spatial distribution and influence of large woody debris in an old-growth forest river system, New Zealand. Forest Ecology and Management 256, 20–27, doi:10.1016/j.foreco.2008.01.051.

Balco, G., Finnegan, N., Gendaszek, A., Stone, J.O., & Thompson, N. (2013). Erosional response to northward-propagating crustal thickening in the coastal ranges of the US Pacific Northwest. American Journal of Science 313, 790–806, doi:10.2475/11.2013.01.

Baldwin, E.M. (1958). Landslide lakes in the Coast Range of Oregon. Geological Newsletter, Geological Society of the Oregon Country 24, 23–24.

Beeson, H.W., Flitcroft, R.L., Fonstad, M.A., & Roering, J.J. (2018). Deep-Seated Landslides Drive Variability in Valley Width and Increase Connectivity of Salmon Habitat in the Oregon Coast Range. Journal of the American Water Resources Association 54, 1325–1340, doi:10.1111/1752-1688.12693.

Benda, L. (1990). The influence of debris flows on channels and valley floors in the Oregon Coast Range, USA. Earth Surface Processes and Landforms 15, 457–466, doi:10.1002/esp.3290150508.

Benda, L., Veldhuisen, C., & Black, J. (2003). Debris flows as agents of morphological heterogeneity at low-order confluences, Olympic Mountains, Washington. Geological Society of America Bulletin. 115, 1110, doi:10.1130/B25265.1.

Bilby, R.E., & Likens, G.E. (1980). Importance of Organic Debris Dams in the Structure and Function of Stream Ecosystems. Ecology 61, 1107–1113, doi:10.2307/1936830.

Black, B.A., Dunham, J.B., Blundon, B.W., Brim-Box, J., & Tepley, A.J. (2015). Long term growth-increment chronologies reveal diverse influences of climate forcing on freshwater and forest biota in the Pacific Northwest. Global Change Biology 21, 594–604, doi:10.1111/gcb.12756.

Booth, A.M., LaHusen, S.R., Duvall, A.R., & Montgomery, D.R. (2017). Holocene history of deep-seated landsliding in the North Fork Stillaguamish River valley from surface roughness analysis, radiocarbon dating, and numerical landscape evolution modeling: Landsliding in the N. Fork Stillaguamish. Journal of Geophysical Research: Earth Surface 122, 456–472, doi:10.1002/2016JF003934.

Booth, A.M., Roering, J.J., & Perron, J.T. (2009). Automated landslide mapping using spectral analysis and high-resolution topographic data: Puget Sound lowlands, Washington, and Portland Hills, Oregon. Geomorphology 109, 132–147, doi:10.1016/j.geomorph.2009.02.027.

Bronk Ramsey, C. (1995). Radiocarbon Calibration and Analysis of Stratigraphy: The OxCal Program. Radiocarbon 37, 425–430, doi:10.1017/S0033822200030903.

Bronk Ramsey, C. (2009). Bayesian analysis of radiocarbon dates. Radiocarbon 51, 337-360, doi:10.1017/S0033822200033865.

Burns, W.J., Calhoun, N.C., Franczyk, J.J., Koss, R.J., & Bordal, M.G. (2017). Estimating Losses from Landslides in Oregon. In De Graff, J.V. and Shakoor, A. (eds.), Landslides: Putting Experience, Knowledge and Emerging Technologies into Practice, AEG Special Publication No. 27, p. 473-482.

Burns, W.J., & Madin, I.P. (2009). Protocol for Inventory Mapping of Landslide Deposits from Light Detection and Ranging (Lidar) Imagery (Special Paper 42). Oregon Department of Geology and Mineral Industries.

Chen, X., Leung, L.R., Gao, Y., Liu, Y., Wigmosta, M., & Richmond, M. (2018). Predictability of Extreme Precipitation in Western U.S. Watersheds Based on Atmospheric River Occurrence, Intensity, and Duration. Geophysical Research Letters 45, 11,693-11,701, doi:10.1029/2018GL079831.

Clague, J.J. (2015). Paleolandslides, in: Landslide Hazards, Risks and Disasters. Elsevier, pp. 321–344, doi:10.1016/B978-0-12-396452-6.00010-0.

Costa, J.E., & Schuster, R.L. (1988). The formation and failure of natural dams. Geological Society of America Bulletin 100, 15.

Dal Sasso, S.F., Sole, A., Pascale, S., Sdao, F., Bateman Pinzòn, A., & Medina, V. (2014). Assessment methodology for the prediction of landslide dam hazard. Natural Hazards and Earth System Sciences 14, 557–567, doi10.5194/nhess-14-557-2014.

Deligne, N.I., Cashman, K.V., & Roering, J.J. (2013). After the lava flow: The importance of external soil sources for plant colonization of recent lava flows in the central Oregon Cascades, USA. Geomorphology 202, 15–32, doi:10.1016/j.geomorph.2012.12.009.

Dettinger, M.D., Ralph, F.M., & Rutz, J.J. (2018). Empirical Return Periods of the Most Intense Vapor Transports during Historical Atmospheric River Landfalls on the U.S. West Coast. J. Hydrometeor. 19, 1363–1377, doi:10.1175/JHM-D-17-0247.1.

Fan, X., Dufresne, A., Siva Subramanian, S., Strom, A., Hermanns, R., Tacconi Stefanelli, C., et al. (2020). The formation and impact of landslide dams – State of the art. Earth-Science Reviews 203, 103116, doi:10.1016/j.earscirev.2020.103116.

Fan, X., Scaringi, G., Korup, O., West, A.J., Westen, C.J., Tanyas, H., et al. (2019). Earthquake-Induced Chains of Geologic Hazards: Patterns, Mechanisms, and Impacts. Reviews of Geophysics 57, 421–503, doi:10.1029/2018RG000626.

Fan, X., Zhan, W., Dong, X., van Westen, C., Xu, Q., Dai, et al. (2018). Analyzing successive landslide dam formation by different triggering mechanisms: The case of the Tangjiawan landslide, Sichuan, China. Engineering Geology 243, 128–144, doi:10.1016/j.enggeo.2018.06.016.

Finnegan, N.J., Broudy, K.N., Nereson, A.L., Roering, J.J., Handwerger, A.L., & Bennett, G. (2019). River channel width controls blocking by slow-moving landslides in California's Franciscan mélange. Earth Surface Dynamics 7, 879-894, doi:10.5194/esurf-7-879-2019.

Franczyk, J.J., Burns, W.J., & Calhoun, N.C. (2019). Statewide Landslide Information Database for Oregon Release-4.0, SLIDO 4.0, Oregon Department of Geology and Mineral Industries, Digital Data Series.

Frankel, A., Wirth, E., Marafi, N., Vidale, J., & Stephenson, W. (2018). Broadband Synthetic Seismograms for Magnitude 9 Earthquakes on the Cascadia Megathrust Based on 3D Simulations and Stochastic Synthetics, Part 1: Methodology and Overall Results. Bulletin of the Seismological Society of America 108, 2347-2369, doi: 10.1785/0120180034.

Franklin, J.F., & Waring, R.H. (1979). Distinctive features of the northwestern coniferous forest: Development, structure, and function, in: Forests: Fresh Perspectives from Ecosystem Analysis. Presented at the 40th annual biological colloquium, Oregon State University Press, Corvallis, OR, pp. 59–86.

Gavin, D.G. (2001). Estimation of Inbuilt Age in Radiocarbon Ages of Soil Charcoal for Fire History Studies. Radiocarbon 43, 27–44, doi:10.1017/S003382220003160X.

Goldfinger, C., Nelson, C.H., Morey, A.E., Johnson, J.E., Patton, J.R., Karabanov, E., et al. (2012). Turbidite event history: Methods and implications for Holocene paleoseismicity of the Cascadia subduction zone. US Geological Survey Professional Paper 1661, 170.

Harden, D., R., Janda, R.J., & Nolan, K.M. (1978). Mass Movement and Storms in the Drainage Basin of Redwood Creek, Humboldt County, California - A Progress Report (No. 78–486). United States Geological Survey.

Harr, R.D. (1981). Some characteristics and consequences of snowmelt during rainfall in western Oregon. Journal of Hydrology 53, 277–304, doi:10.1016/0022-1694(81)90006-8.

Heller, P.L., & Dickinson, W.R. (1985). Submarine Ramp Facies Model for Delta-Fed, Sand-Rich Turbidite Systems. AAPG Bulletin 69, doi:10.1306/AD462B37-16F7-11D7-8645000102C1865D.

Hewitt, K. (1998). Catastrophic landslides and their effects on the Upper Indus streams, Karakoram Himalaya, northern Pakistan. Geomorphology 26, 47–80, doi:10.1016/S0169-555X(98)00051-8.

Hinshaw, S., Wohl, E., & Davis, D. (2020). The effects of longitudinal variations in valley geometry and wood load on flood response. Earth Surface Processes and Landforms esp.4940, doi:10.1002/esp.4940.

Hogg, A.G., Heaton, T.J., Ramsey, C.B., Boswijk, G., Palmer, J.G., Turney, C.S.M., et al. (2019). The Influence of Calibration Curve Construction and Composition on the Accuracy and Precision of Radiocarbon Wiggle-Matching of Tree Rings, Illustrated by Southern Hemisphere Atmospheric Data Sets from AD 1500–1950. Radiocarbon 61, 1265–1291, doi:10.1017/RDC.2019.42.

Holmes, R.L. (1983). Computer-assisted quality control in tree-ring dating and measurement. Tree-Ring Bulletin 43: 69-78.

Hovius, N., Stark, C.P., & Allen, P.A. (1997). Sediment flux from a mountain belt derived by landslide mapping. Geology 25, 231, doi:10.1130/0091-7613(1997)025.

Keefer, D.K. (1984). Landslides caused by earthquakes. Geological Society of America Bulletin 95, 406–421, doi:10.1130/0016-7606(1984)95&amp;amp;lt;406:LCBE

Kelsey, H.M., Ticknor, R.L., Bockheim, J.G., & Mitchell, E. (1996). Quaternary upper plate deformation in coastal Oregon. Geological Society of America Bulletin 108, 843–860, doi:10.1130/0016-7606(1996)108<0843:QUPDIC>2.3.CO;2.

Korup, O. (2004). Geomorphometric characteristics of New Zealand landslide dams. Engineering Geology 73, 13–35, doi:10.1016/j.enggeo.2003.11.003.

Korup, O., Clague, J.J., Hermanns, R.L., Hewitt, K., Strom, A.L., & Weidinger, J.T. (2007). Giant landslides, topography, and erosion. Earth and Planetary Science Letters 261, 578–589, doi:10.1016/j.epsl.2007.07.025.

Korup, O., McSaveney, M.J., & Davies, T.R.H. (2004). Sediment generation and delivery from large historic landslides in the Southern Alps, New Zealand. Geomorphology 61, 189–207, doi:10.1016/j.geomorph.2004.01.001.

Korup, O., Strom, A.L., & Weidinger, J.T. (2006). Fluvial response to large rock-slope failures: Examples from the Himalayas, the Tien Shan, and the Southern Alps in New Zealand. Geomorphology 78, 3–21. doi:10.1016/j.geomorph.2006.01.020.

LaHusen, S.R., Duvall, A.R., Booth, A.M., Grant, A., Mishkin, B.A., Montgomery, D.R., et al. (2020). Rainfall triggers more deep-seated landslides than Cascadia earthquakes in the Oregon Coast Range, USA. Science Advances 6, eaba6790, doi:10.1126/sciadv.aba6790.

LaHusen, S.R., Duvall, A.R., Booth, A.M., & Montgomery, D.R. (2016). Surface roughness dating of long-runout landslides near Oso, Washington (USA), reveals persistent postglacial hillslope instability. Geology 44, 111–114, doi:10.1130/G37267.1.

Lancaster, S.T., & Casebeer, N.E. (2007). Sediment storage and evacuation in headwater valleys at the transition between debris-flow and fluvial processes. Geology 35, 1027, doi:10.1130/G239365A.1.

Lancaster, S.T., & Grant, G.E. (2006). Debris dams and the relief of headwater streams. Geomorphology 82, 84–97, doi:10.1016/j.geomorph.2005.08.020.

Lancaster, S.T., Hayes, S.K., & Grant, G.E. (2001). Modeling sediment and wood storage and dynamics in small mountainous watersheds, in: Dorava, J.M., Montgomery, D.R., Palcsak, B.B., Fitzpatrick, F.A. (Eds.), Water Science and Application. American Geophysical Union, Washington, D. C., pp. 85–102. doi:10.1029/WS004p0085.

Lane, J.W. (1987). Relations between geology and mass movement features in a part of the East Fork Coquille River watershed, southern Coast Range, Oregon (Masters Thesis). Oregon State University.

Lang, A., Moya, J., Corominas, J., Schrott, L., & Dikau, R. (1999). Classic and new dating methods for assessing the temporal occurrence of mass movements. Geomorphology 30, 33–52, doi:10.1016/S0169-555X(99)00043-4.

Larsen, I.J., Montgomery, D.R., & Korup, O. (2010). Landslide erosion controlled by hillslope material. Nature Geoscience 3, 247–251, doi:10.1038/ngeo776.

Larsson, L. (2013). CooRecorder and CDendro Programs of the CooRecorder/CDendro Package, Version 9.0.

Leithold, E.L., Wegmann, K.W., Bohnenstiehl, D.R., Smith, S.G., Noren, A., & O'Grady, R. (2018). Slope failures within and upstream of Lake Quinault, Washington, as uneven responses to Holocene earthquakes along the Cascadia subduction zone. Quaternary Research 89, 178–200, doi:10.1017/qua.2017.96.

Li, G., West, A.J., Densmore, A.L., Hammond, D.E., Jin, Z., Zhang, F., et al. (2016). Connectivity of earthquake-triggered landslides with the fluvial network: Implications for landslide sediment transport after the 2008 Wenchuan earthquake. Journal of Geophysical Research: Earth Surface 121, 703–724, doi:10.1002/2015JF003718.

Li, G., West, A.J., Densmore, A.L., Jin, Z., Parker, R.N., & Hilton, R.G. (2014). Seismic mountain building: Landslides associated with the 2008 Wenchuan earthquake in the context of a generalized model for earthquake volume balance. Geochemistry, Geophysics, Geosystems 15, 833–844, doi:10.1002/2013GC005067.

Mackey, B.H., Roering, J.J., & Lamb, M.P. (2011). Landslide-dammed paleolake perturbs marine sedimentation and drives genetic change in anadromous fish. Proceedings of the National Academy of Sciences 108, 18905–18909, doi:10.1073/pnas.1110445108.

Madin, I.P., & Burns, W.J. (2013). Ground motion, ground deformation, tsunami inundation, coseismic subsidence, and damage potential maps for the 2012 Oregon Resilience Plan for Cascadia Subduction Zone Earthquakes: Oregon Department of Geology and Mineral Industries, Open-File Report O-13-06.

Marc, O., Gosset, M., Saito, H., Uchida, T., & Malet, J. (2019). Spatial Patterns of Storm Induced Landslides and Their Relation to Rainfall Anomaly Maps. Geophysical Research Letters. 2019GL083173, doi:10.1029/2019GL083173.

Marc, O., Hovius, N., Meunier, P., Gorum, T., & Uchida, T. (2016). A seismologically consistent expression for the total area and volume of earthquake-triggered landsliding. Journal of Geophysical Research: Earth Surface 121, 640–663: doi:10.1002/2015JF003732.

Marc, O., Hovius, N., Meunier, P., Uchida, T., & Hayashi, S. (2015). Transient changes of landslide rates after earthquakes. Geology 43, 883–886, doi:10.1130/G36961.1.

Marshall, J.A., Roering, J.J., Gavin, D.G., & Granger, D.E. (2017). Late Quaternary climatic controls on erosion rates and geomorphic processes in western Oregon, USA. Geological Society of America Bulletin 129, 715–731, doi:10.1130/B31509.1.

Massey, C., Townsend, D., Rathje, E., Allstadt, K.E., Lukovic, B., Kaneko, Y., et al. (2018). Landslides Triggered by the 14 November 2016 Mw 7.8 Kaikōura Earthquake, New Zealand. Bulletin of the Seismological Society of America 108, 1630–1648, doi:10.1785/0120170305.

May, C.L. (2002). Debris flows through different forest age classes in the central Oregon Coast Range. Journal of the American Water Resources Association 38, 1097-1113, doi:10.1111/j.1752-1688.2002.tb05549.x.

May, C., Roering, J., Eaton, L.S., & Burnett, K.M. (2013). Controls on valley width in mountainous landscapes: The role of landsliding and implications for salmonid habitat. Geology 41, 503–506, doi:10.1130/G33979.1.

McPhee, D.K., Langenheim, V.E., Wells, R.E., & Blakely, R.J. (2014). Tectonic evolution of the Tualatin basin, northwest Oregon, as revealed by inversion of gravity data. Geosphere 10, 264–275, doi:10.1130/GES00929.1.

Miller, G.R. (1999). The Great Willamette River Flood of 1861. Oregon Historical Quarterly 100, 182–207.

Montgomery, D.R. (2001). Slope distributions, threshold hillslopes, and steady-state topography. American Journal of Science 301, 432–454, doi:10.2475/ajs.301.4-5.432.

Montgomery, D.R., & Brandon, M.T. (2002). Topographic controls on erosion rates in tectonically active mountain ranges. Earth and Planetary Science Letters 201, 481–489, doi:10.1016/S0012-821X(02)00725-2.

Montgomery, D.R., Schmidt, K.M., Greenberg, H.M., & Dietrich, W.E. (2000). Forest clearing and regional landsliding. Geology 28, 4, doi:10.1130/0091-7613(2000)28<311:FCARL>>2.0.CO;2..

Morey, A.E., Goldfinger, C., Briles, C.E., Gavin, D.G., Colombaroli, D., & Kusler, J.E. (2013). Are great Cascadia earthquakes recorded in the sedimentary records from small forearc lakes? Natural Hazards and Earth System Science 13, 2441–2463, doi:10.5194/nhess-13-2441-2013.

Neiman, P.J., Ralph, F.M., Wick, G.A., Kuo, Y.-H., Wee, T.-K., Ma, Z., et al. (2008). Diagnosis of an Intense Atmospheric River Impacting the Pacific Northwest: Storm Summary and Offshore Vertical Structure Observed with COSMIC Satellite Retrievals. Monthly Weather Review 136, 4398–4420, doi:10.1175/2008MWR2550.1.

Oakley, N.S., Lancaster, J.T., Hatchett, B.J., Stock, J., Ralph, F.M., Roj, S., & Lukashov, S. (2018). A 22-Year Climatology of Cool Season Hourly Precipitation Thresholds Conducive to Shallow Landslides in California. Earth Interactions 22, 1–35, doi:10.1175/EI-D-17-0029.1.

O'Connor, J.E., Mangano, J.F., Anderson, S.W., Wallick, J.R., Jones, K.L., & Keith, M.K. (2014). Geologic and physiographic controls on bed-material yield, transport, and channel morphology for alluvial and bedrock rivers, western Oregon. Geological Society of America Bulletin 126, 377–397, doi:10.1130/B30831.1.

Ogle, S., Fish, M.A., Wilson, A.M., Oakley, N., Slaughter, S., & Ralph, M. (2018). Atmospheric River Families and their Relationship to Landslides in Washington State. In AGU Fall Meeting 2018. AGU.

Orr, E.L., & Orr, W.N. (1999). The other face of Oregon: Geologic processes that shape our state. Oregon Geology 61, 131–150.

Penserini, B.D., Roering, J.J., & Streig, A. (2017). A morphologic proxy for debris flow erosion with application to the earthquake deformation cycle, Cascadia Subduction Zone, USA. Geomorphology 282, 150–161, doi:10.1016/j.geomorph.2017.01.018.

Petersen, N.E. (1948). High Water and the Great Slide. The Siuslaw Pioneer 17–23.

Pierson, T.C., Evarts, R.C., & Bard, J.A. (2016). Landslides in the western Columbia Gorge, Skamania County, Washington. U.S. Geological Survey Scientific Investigations Map 3358.

Pringle, P.T. (2014). Buried and Submerged Forests of Washington and Oregon: Time Capsules of Environmental and Geologic History. Western Forester 59, 14–15, 22.

PRISM Climate Group (2016), PRISM Climate Group: Corvallis, Oregon, Oregon State University.

Ralph, F.M., Neiman, P.J., Wick, G.A., Gutman, S.I., Dettinger, M.D., Cayan, D.R., & White, A.B. (2006). Flooding on California's Russian River: Role of atmospheric rivers. Geophysical Research Letters 33, L13801, doi:10.1029/2006GL026689.

Ralph, F.M., Rutz, J.J., Cordeira, J.M., Dettinger, M., Anderson, M., Reynolds, D., et al. (2019). A Scale to Characterize the Strength and Impacts of Atmospheric Rivers. Bulletin of the American Meteorological Society 100, 269–289, doi:10.1175/BAMS-D-18-0023.1.

Rantz, S.E. (1959). Floods of January 1953 in western Oregon and northwestern California (Geological Survey Water-Supply Paper No. 1320- D). United States Geological Survey, U.S. Government Printing Office, Washington, doi:10.3133/wsp1320D.

Reneau, S.L., & Dietrich, W.E. (1991). Erosion rates in the southern Oregon Coast Range: Evidence for an equilibrium between hillslope erosion and sediment yield. Earth Surface Processes and Landforms 16, 307–322, doi:10.1002/esp.3290160405.

Richardson, K.N.D., Hatten, J.A., & Wheatcroft, R.A. (2018). 1500 years of lake sedimentation due to fire, earthquakes, floods and land clearance in the Oregon Coast Range: geomorphic sensitivity to floods during timber harvest period. Earth Surface Processes and Landforms 43, 1496–1517, doi:10.1002/esp.4335.

Roering, J.J., Kirchner, J.W., & Dietrich, W.E. (2005). Characterizing structural and lithologic controls on deep-seated landsliding: Implications for topographic relief and landscape evolution in the Oregon Coast Range, USA. Geological Society of America Bulletin 117, 654, doi:10.1130/B25567.1.

Roering, J.J., Mackey, B.H., Handwerger, A.L., Booth, A.M., Schmidt, D.A., Bennett, G.L., & Cerovski-Darriau, C. (2015). Beyond the angle of repose: A review and synthesis of landslide processes in response to rapid uplift, Eel River, Northern California. Geomorphology 236, 109–131, doi:10.1016/j.geomorph.2015.02.013.

Scharer, K.M., Biasi, G.P., & Weldon, R.J. (2011). A reevaluation of the Pallett Creek earthquake chronology based on new AMS radiocarbon dates, San Andreas fault, California. Journal of Geophysical Research 116, doi:10.1029/2010JB008099.

Schmidt, K.M., Roering, J.J., Stock, J.D., Dietrich, W.E., Montgomery, D.R., & Schaub, T. (2001). The variability of root cohesion as an influence on shallow landslide susceptibility in the Oregon Coast Range. Canadian Geotechnical Journal 38, 31, doi:10.1139/t01-031.

Schulz, W.H., Galloway, S.L., & Higgins, J.D. (2012). Evidence for earthquake triggering of large landslides in coastal Oregon, USA. Geomorphology 141–142, 88–98, doi:10.1016/j.geomorph.2011.12.026.

Schuster, R.L., Logan, R.L., & Pringle, P.T. (1992). Prehistoric Rock Avalanches in the Olympic Mountains, Washington. Science 258, 1620–1621, doi:10.1126/science.258.5088.1620.

Scott, D.N., & Wohl, E. (2020). Geomorphology and climate interact to control organic carbon stock and age in mountain river valley bottoms. Earth Surface Processes and Landforms 45, 1911–1925, doi:10.1002/esp.4855.

Serey, A., Piñero-Feliciangeli, L., Sepúlveda, S.A., Poblete, F., Petley, D.N., & Murphy, W. (2019). Landslides induced by the 2010 Chile megathrust earthquake: a comprehensive inventory and correlations with geological and seismic factors. Landslides, doi:10.1007/s10346-019-01150-6.

Shang, Y., Yang, Z., Li, L., Liu, D., Liao, Q., & Wang, Y. (2003). A super-large landslide in Tibet in 2000: background, occurrence, disaster, and origin. Geomorphology 54, 225–243, doi:10.1016/S0169-555X(02)00358-6.

Shobe, C.M., Tucker, G.E., & Anderson, R.S. (2016). Hillslope-derived blocks retard river incision. Geophysical Research Letters 43, 5070–5078, doi:10.1002/2016GL069262.

Šilhán, K. (2020). Dendrogeomorphology of landslides: principles, results and perspectives. Landslides, doi:10.1007/s10346-020-01397-4.

Stock, J., & Dietrich, W.E. (2003). Valley incision by debris flows: Evidence of a topographic signature. Water Resources Research 39, doi:10.1029/2001WR001057.

Streig, A.R., Weldon, R.J., Biasi, G., Dawson, T.E., Gavin, D.G., & Guilderson, T.P. (2020). New Insights into Paleoseismic Age Models on the Northern San Andreas Fault: Charcoal Inbuilt Ages and Updated Earthquake Correlations. Bulletin of the Seismological Society of America 110, 1077–1089, doi:10.1785/0120190307.

Struble, W.T., Roering, J.J., Black, B.A., Burns, W.J., Calhoun, N., & Wetherell, L. (2020). Dendrochronological dating of landslides in western Oregon: Searching for signals of the Cascadia A.D. 1700 earthquake. Geological Society of America Bulletin 130, 17, doi:10.1130/B35269.1.

Swanson, F.J., Oyagi, N., & Tominaga, M. (1986). Landslide dams in Japan, in: Landslide Dams: Processes, Risk, and Mitigation. pp. 131–145.

Tacconi Stefanelli, C., Segoni, S., Casagli, N., & Catani, F. (2016). Geomorphic indexing of landslide dams evolution. Engineering Geology 208, 1–10, doi:10.1016/j.enggeo.2016.04.024.

Theule, J.I. (2008). Determining landslide susceptibility along natural gas pipelines in northwest Oregon (Masters Thesis). Portland State University.

Thrall, G.F., Jack, R., Johnson, J.J., & Stanley, D.A. (1980). Failure mechanisms of the Drift Creek Slide. Presented at the Cordilleran Section of Geological Society of America, Corvallis, Oregon, p. 156.

Trumbore, S.E. (2000). Radiocarbon geochronology, in: Noller, J.S., Sowers, J.M., Lettis, W.R. (Eds.), AGU Reference Shelf. American Geophysical Union, Washington, D. C., pp. 41–60, doi:10.1029/RF004p0041.

Walker, G.W., & MacLeod, N.S. (1991). Geologic Map of Oregon.

Wartman, J., Dunham, L., Tiwari, B., & Pradel, D. (2013). Landslides in Eastern Honshu Induced by the 2011 Tohoku Earthquake. Bulletin of the Seismological Society of America 103, 1503–1521, doi:10.1785/0120120128.

Wells, R., Bukry, D., Friedman, R., Pyle, D., Duncan, R., Haeussler, P., & Wooden, J. (2014). Geologic history of Siletzia, a large igneous province in the Oregon and Washington Coast Range: Correlation to the geomagnetic polarity time scale and implications for a long-lived Yellowstone hotspot. Geosphere 10, 692–719, doi:10.1130/GES01018.1.

Wells, R.E., Blakely, R.J., & Bemis, S. (2020). Northward migration of the Oregon forearc on the Gales Creek fault. Geosphere 16, 660–684, doi:10.1130/GES02177.1.

Wiley, T.J. (2000). Relationship between rainfall and debris flows in western Oregon. Oregon Geology 62.

Wirth, E.A., Frankel, A.D., Marafi, N., Vidale, J.E., & Stephenson, W.J. (2018). Broadband Synthetic Seismograms for Magnitude 9 Earthquakes on the Cascadia Megathrust Based on 3D Simulations and Stochastic Synthetics, Part 2: Rupture Parameters and Variability. Bulletin of the Seismological Society of America 108, 2370–2388, doi:10.1785/0120180029.

Wohl, E. (2017). Bridging the gaps: An overview of wood across time and space in diverse rivers. Geomorphology 279, 3–26, doi:10.1016/j.geomorph.2016.04.014.

Wong, I.G., & Bott, J.D.J. (1995). A look back at Oregon's earthquake history, 1841-1994. Oregon Geology 57, 125–139.

Worona, M.A., & Whitlock, C. (1995). Late Quaternary vegetation and climate history near Little Lake, central Coast Range, Oregon. Geological Society of America Bulletin 10.

Wu, C.-H., Chen, S.-C., & Feng, Z.-Y. (2014). Formation, failure, and consequences of the Xiaolin landslide dam, triggered by extreme rainfall from Typhoon Morakot, Taiwan. Landslides 11, 357–367, doi:10.1007/s10346-013-0394-4.

Yamaguchi, D.K., Atwater, B.F., Bunker, D.E., Benson, B.E., & Reid, M.S. (1997). Tree-ring dating the 1700 Cascadia earthquake. Nature 389, 922–923, doi:10.1038/40048.

Zybach, B. (2003). The Great Fires: Indian Burning and Catastrophic Forest Fire Patterns of the Oregon Coast Range, 1491-1951 (Masters Thesis). Oregon State University, Corvallis, OR.

**Chapter IV**
Audet, P., (2011). Directional wavelet analysis on the sphere: Application to gravity and topography of the terrestrial planets. Journal of Geophysical Research, 116(E1), E01003, doi:10.1029/2010JE003710.

Audet, P. (2014). Toward mapping the effective elastic thickness of planetary lithospheres from a spherical wavelet analysis of gravity and topography. Physics of the Earth and Planetary Interiors, 226, 48–82, doi:10.1016/j.pepi.2013.09.011.

Audet, P., Bostock, M. G., Boyarko, D. C., Brudzinski, M. R., & Allen, R. M. (2010). Slab morphology in the Cascadia fore arc and its relation to episodic tremor and slip. Journal of Geophysical Research, 115, B00A16, doi:10.1029/2008JB006053.

Balco, G., Finnegan, N., Gendaszek, A., Stone, J. O., & Thompson, N. (2013). Erosional response to northward-propagating crustal thickening in the coastal ranges of the US Pacific Northwest. American Journal of Science, 313(8), 790–806, doi:10.4275/11.2013.01.

Baldwin, E. M., & Howell, P. W. (1949). The Long Tom, a Former Tributary of the Siuslaw River. Northwest Science, 23, 112–124.

Bassett, D., & Watts, A. B. (2015). Gravity anomalies, crustal structure, and seismicity at subduction zones: 2. Interrelationships between fore-arc structure and seismogenic behavior. Geochemistry, Geophysics, Geosystems, 16(5), 1541 1576, doi:10.1002/2014GC005685.

Becker, T.W., Faccenna, C., Humphreys, E.D., Lowry, A.R., & Miller, M.S. (2014). Static and dynamic support of western United States topography. Earth and Planetary Science Letters, 402, 234-246, doi:10.1016/j.epsl.2013.10.012.

Beeson, H.W., McCoy, S.W., & Keen-Zebert, A. (2017). Geometric disequilibrium of river basins produces long-lived transient landscapes. Earth and Planetary Science Letters, 475, 34–43, doi:10.1016/j.epsl.2017.07.010.

Beeson, M. H., Tolan, T. L., & Anderson, J. L. (1989). The Columbia River Basalt Group in western Oregon; Geologic structures and other factors that controlled flow emplacement patterns. Geological Society of America, Special Paper 239, 223-246, doi:10.1130/SPE239-p223.

Black, B. A., Perron, J. T., Hemingway, D., Bailey, E., Nimmo, F., & Zebker, H. (2017). Global drainage patterns and the origins of topographic relief on Earth, Mars, and Titan. Science, 356(6339), 727–731, doi:10.1126/science.aag0171.

Blakely, R. J., Wells, R. E., Tolan, T. L., Beeson, M. H., Trehu, A. M., & Liberty, L. M. (2000). New aeromagnetic data reveal large strike-slip (?) faults in the northern Willamette Valley, Oregon. Geological Society of America Bulletin 112(8),1125-1233, doi:10.1130/0016-7606(2000)112<1225:FADRLS>2.0.CO;2.

Blakely, R. J., Brocher, T. M., & Wells, R. E. (2005). Subduction-zone magnetic anomalies and implications for hydrated forearc mantle. Geology, 33(6), 445 448, doi:10.1130/G21447.1.

Bodmer, M., Toomey, D. R., Roering, J. J., & Karlstrom, L. (2019). Asthenospheric buoyancy and the origin of high-relief topography along the Cascadia forearc. Earth and Planetary Science Letters, 115965, doi:10.1016/j.epsl.2019.115965.

Bodmer, Miles, Toomey, D. R., Hooft, E. E., Nábělek, J., & Braunmiller, J. (2015). Seismic anisotropy beneath the Juan de Fuca plate system: Evidence for heterogeneous mantle flow. Geology, G37181.1, doi:10.1130/G37181.1.

Bomberger, C., Bendick, R., Flesch, L., & Ehlers, T. A. (2018). Spatial Scales in Topography and Strain Rate Magnitude in the Western United States. Journal of Geophysical Research: Solid Earth, 123(7), 6086–6097, doi:10.1029/2018JB016135.

Booth, A. M., Roering, J. J., & Perron, J. T. (2009). Automated landslide mapping using spectral analysis and high-resolution topographic data: Puget Sound lowlands, Washington, and Portland Hills, Oregon. Geomorphology, 109(3–4), 132–147, doi:10.1016/j.geomorph.2009.02.027.

Brocher, T. M., Parsons, T., Trehu, A. M., Snelson, C. M., & Fisher, M. A. (2003). Seismic evidence for widespread serpentinized forearc upper mantle along the Cascadia margin. Geology, 31(3), 267–270, doi:10.1130/0091-7613(2003)031<0267:SEFWSF>2.0.CO;2.

Calvert, A. J., Preston, L. A., & Farahbod, A. M. (2011). Sedimentary underplating at the Cascadia mantle-wedge corner revealed by seismic imaging. Nature Geoscience, 4(8), 545–548, doi:10.1038/ngeo1195.

Campbell, M. R. (1896). Drainage Modifications and Their Interpretation. The Journal of Geology, 4(5), 567–581.

Chylek, S. J. (2002). GIS Analysis of Quaternary Stream Capture in the Eastern Coast Range, Western Oregon (Undergraduate Honors Thesis). University of Oregon.

von Dassow, W. (2018). Geomorphic Evidence for Differential Rock Uplift Across the Southern Cascadia Forearc (Masters Thesis). Oregon State University.

Davies, D. R., Valentine, A. P., Kramer, S. C., Rawlinson, N., Hoggard, M. J., Eakin, C. M., & Wilson, C. R. (2019). Earth's multi-scale topographic response to global mantle flow. Nature Geoscience, 12(10), 845–850, doi:10.1038/s41561-019-0441-4.

Delph, J. R., Levander, A., & Niu, F. (2018). Fluid Controls on the Heterogeneous Seismic Characteristics of the Cascadia Margin. Geophysical Research Letters, 45(20), doi:10.1029/2018GL079518.

DeMets, C., Gordon, R. G., & Argus, D. F. (2010). Geologically current plate motions. Geophysical Journal International, 181(1), 1–80, doi:10.1111/j.1365-246X.2009.04491.x.

Doane, T. H., Roth, D. L., Roering, J. J., & Furbish, D. J. (2019). Compression and Decay of Hillslope Topographic Variance in Fourier Wavenumber Domain. Journal of Geophysical Research: Earth Surface, doi:10.1029/2018JF004724.

Facenna, C., & Becker, T.W. (2020). Topographic expressions of mantle dynamics in the Mediterranean. Earth-Science Reviews, 209, 103327, doi:10.1016/j.earscirev.2020.103327.

Faccenna, C., Glišović, P., Forte, A., Becker, T. W., Garzanti, E., Sembroni, A., & Gvirtzman, Z. (2019). Role of dynamic topography in sustaining the Nile River over 30 million years. Nature Geoscience, doi:10.1038/s41561-019-0472-x.

Forte, A. M., & Whipple, K. X. (2018). Criteria and tools for determining drainage divide stability. Earth and Planetary Science Letters, 493, 102–117, doi:10.1016/j.epsl.2018.04.026.

Forte, A. M., Yanites, B. J., & Whipple, K. X. (2016). Complexities of landscape evolution during incision through layered stratigraphy with contrasts in rock strength. Earth Surface Processes and Landforms, 41, 1736–1757, doi:10.1002/esp.3947.

Foufoula-Georgiou, E., & Kumar, P. (1994). Wavelet Analysis in Geophysics. In Wavelet Analysis and Its Applications (Vol. 4, p. 372). New York: Academic Press, doi:10.1016/B978-0-08-052087-2.50007-4.

Furlong, K. P., & Govers, R. (1999). Ephemeral crustal thickening at a triple junction: The Mendocino crustal conveyor. Geology, 27(2), 127–130, doi:10.1130/0091-7613(1999)027.

Gallen, S. F. (2018). Lithologic controls on landscape dynamics and aquatic species evolution in post-orogenic mountains. Earth and Planetary Science Letters, 493, 150–160, doi:10.1016/j.epsl.2018.04.029.

Goren, L., Willett, S. D., Herman, F., & Braun, J. (2014). Coupled numerical-analytical approach to landscape evolution modeling. Earth Surface Processes and Landforms, 39(4), 522–545, doi:10.1002/esp.3514.

Hawley, W. B., & Allen, R. M. (2019). The Fragmented Death of the Farallon Plate. Geophysical Research Letters, 2019GL083437, doi:10.1029/2019GL083437.

Hyndman, R. D., & Peacock, S. M. (2003). Serpentinization of the forearc mantle. Earth and Planetary Science Letters, 212(3–4), 417–432, doi:10.1016/S0012-821X(03)00263-2.

Jaccard, P. (1900). Étude comparative de la distribution florale dans une portion des Alpes et des Jura. Bulletin de La Societe Vaudoise Des Sciences Naturelles, 37(142), 547–579, doi:10.5169/seals-266450.

Johnson, K. M., & Tebo, D. (2018). Capturing 50 Years of Postseismic Mantle Flow at Nankai Subduction Zone. Journal of Geophysical Research: Solid Earth, 123(11), 10,091-10,106, doi:10.1029/2018JB016345.

Kelsey, H. M., Engebretson, D. C., Mitchell, C. E., & Ticknor, R. L. (1994). Topographic form of the Coast Ranges of the Cascadia Margin in relation to coastal uplift rates and plate subduction. Journal of Geophysical Research, 99(B6), 12245–12255, doi:10.1029/93JB03236.

Kirby, E., & Whipple, K.X. (2012). Expression of active tectonics in erosional landscapes. Journal of Structural Geology, 44, 54–75, doi:10.1016/j.jsg.2012.07.009.

Lashermes, B., Foufoula-Georgiou, E., & Dietrich, W. E. (2007). Channel network extraction from high resolution topography using wavelets. Geophysical Research Letters, 34(23), doi:10.1029/2007GL031140.

Levandowsky, M., & Winter, D. (1971). Distance between sets. Nature, 234, 34–35.

Lock, J., Kelsey, H., Furlong, K., & Woolace, A. (2018). Late Neogene and Quaternary landscape evolution of the northern California Coast Ranges: Evidence for Mendocino triple junction tectonics. Geological Society of America Bulletin, 15, doi:10.1130/B25885.1.

Malamud, B. D., & Turcotte, D. L. (2001). Wavelet analyses of Mars polar topography. Journal of Geophysical Research: Planets, 106(E8), 17497–17504. doi:10.1029/2000JE001333.

Mallat, S. (1999). A Wavelet Tour of Signal Processing (2nd ed.). San Deigo, Calif: Elsevier.

McPhee, D. K., Langenheim, V. E., Wells, R. E., & Blakely, R. J. (2014). Tectonic evolution of the Tualatin basin, northwest Oregon, as revealed by inversion of gravity data. Geosphere, 10(2), 264–275, doi:10.1130/GES00929.1.

Mitchell, N.A., & Yanites, B.J. (2019). Spatially Variable Increase in Rock Uplift in the Northern U.S. Cordillera Recorded in the Distribution of River Knickpoints and Incision Depths. Journal of Geophysical Research Earth Surface, 124, 1238–1260, doi:10.1029/2018JF004880.

Moeller, B. (1990). Stream Capture in the Central Oregon Coast Range and its Relationship to Tectonic and Structural Geology (Masters Thesis). University of Oregon, Eugene, OR.

Moodie, A. J., Pazzaglia, F. J., & Berti, C. (2018). Exogenic forcing and autogenic processes on continental divide location and mobility. Basin Research, 30(2), 344–369, doi:10.1111/bre.12256.

Mudd, S. M., & Furbish, D. J. (2005). Lateral migration of hillcrests in response to channel incision in soil-mantled landscapes. Journal of Geophysical Research: Earth Surface, 110(F4), doi:10.1029/2005JF000313.

Niem, W. A. (1976). Drainage basin morphology in the central Coast Range of Oregon (Masters Thesis). Oregon State University.

O'Hara, D., Karlstrom, L., & Roering, J. J. (2019). Distributed landscape response to localized uplift and the fragility of steady states. Earth and Planetary Science Letters, 506, 243–254, doi:10.1016/j.epsl.2018.11.006.

Perron, J. T., & Royden, L. (2013). An integral approach to bedrock river profile analysis. Earth Surface Processes and Landforms, 38(6), 570–576, doi:10.1002/esp.3302.

Perron, J. T., Kirchner, J. W., & Dietrich, W. E. (2008). Spectral signatures of characteristic spatial scales and nonfractal structure in landscapes. Journal of Geophysical Research, 113(F4), doi:10.1029/2007JF000866.

Ramachandran, K., Hyndman, R. D., & Brocher, T. M. (2006). Regional P wave velocity structure of the Northern Cascadia Subduction Zone. Journal of Geophysical Research: Solid Earth, 111(B12), doi:10.1029/2005JB004108.

Reidel, S. P., & Tolan, T. L. (2013). The late Cenozoic evolution of the Columbia River system in the Columbia River flood basalt province. In Geological Society of America Special Papers (Vol. 497, pp. 201–230). Geological Society of America, doi:10.1130/2013.2497(08).

Richardson, P., & Karlstrom, L. (2019). The multi-scale influence of topography on lava flow morphology. Bulletin of Volcanology, 81(4), 21, doi:10.1007/s00445-019-1278-9

Roberts, G. G. (2019). Scales of Similarity and Disparity Between Drainage Networks. Geophysical Research Letters, doi:10.1029/2019GL082446.

Roberts, G. G., White, N., & Lodhia, B. H. (2019). The Generation and Scaling of Longitudinal River Profiles. Journal of Geophysical Research: Earth Surface, 124(1), 137–153, doi:10.1029/2018JF004796.

Sare, R., Hilley, G.E., & DeLong, S.B. (2019). Regional-Scale Detection of Fault Scarps and Other Tectonic Landforms: Examples from Northern California. Journal of Geophysical Research: Solid Earth, 124(1),1016-1035, doi:10.1029/2018JB016886.

Schwanghart, W., & Scherler, D. (2014). Short Communication: TopoToolbox 2 - MATLAB-based software for topographic analysis and modeling in Earth surface sciences. Earth Surface Dynamics, 2(1), 1–7, doi:10.5194/esurf-2-12014.

Torrence, C., & Compo, G. P. (1998). A Practical Guide to Wavelet Analysis. Bulletin of the American Meteorological Society, 79(1), 18, doi:10.1175/1520-0477(1998)079<0061:APGTWA>2.0.CO;2.

Turcotte, D. L., Shcherbakov, R., Malamud, B. D., & Kucinskas, A. B. (2002). Is the Martian crust also the Martian elastic lithosphere? Journal of Geophysical Research: Planets, 107(E11), 1–20, doi:10.1029/2001JE001594.

Walsh, T. J., Korosec, M. A., Phillips, W. M., Logan, R. L., & Schasse, H. W. (1987). Geologic map of Washington-Southwest quadrant.

Wegmann, K. W., Zurek, B. D., Regalla, C. A., Bilardello, D., Wollenberg, J. L., Kopczynski, S. E., et al. (2007). Position of the Snake River watershed divide as an indicator of geodynamic processes in the greater Yellowstone region, western North America. Geosphere, 3(4), 272–281, doi:10.1130/GES00083.1.

Wells, R. E., & McCaffrey, R. (2013). Steady rotation of the Cascade arc. Geology, 41(9), 1027–1030, doi:10.1130/G34514.1.

Wells, R. E., Weaver, C. S., & Blakely, R. J. (1998). Fore-arc migration in Cascadia and its neotectonic significance. Geology, 26(8), 759–762, doi:10.1130/0091-7613(1998)026<0759:FAMICA>2.3.CO;2.

Wells, R. E., Blakely, R. J., Wech, A. G., McCrory, P. A., & Michael, A. (2017). Cascadia subduction tremor muted by crustal faults. Geology, 45(6), 515–518, doi:10.1130/G38835.1.

Whipple, K.X., DiBiase, R. A., Ouimet, W. B., & Forte, A. M. (2017a). Preservation or piracy: Diagnosing low-relief, high-elevation surface formation mechanisms. Geology, 45(1), 91–94, doi:10.1130/G38490.1.

Whipple, K. X., Forte, A. M., DiBiase, R. A., Gasparini, N. M., & Ouimet, W. B. (2017b). Timescales of landscape response to divide migration and drainage capture: Implications for the role of divide mobility in landscape evolution: Landscape Response to Divide Mobility. Journal of Geophysical Research: Earth Surface, doi:10.1002/2016JF003973.

Willett, S. D., McCoy, S. W., Perron, J. T., Goren, L., & Chen, C.-Y. (2014). Dynamic Reorganization of River Basins. Science, 343(6175), 1248765–1248765, doi:10.1126/science.1248765.

Yang, R., Willett, S. D., & Goren, L. (2015). In situ low-relief landscape formation as a result of river network disruption. Nature, 520(7548), 526–529, doi:10.1038/nature14354.

Yeats, R. S., Graven, E. P., Werner, K. S., Goldfinger, C., & Popowski, T. A. (1996). Tectonics of the Willamette Valley, Oregon (Vol. 1). US Government Printing Office.